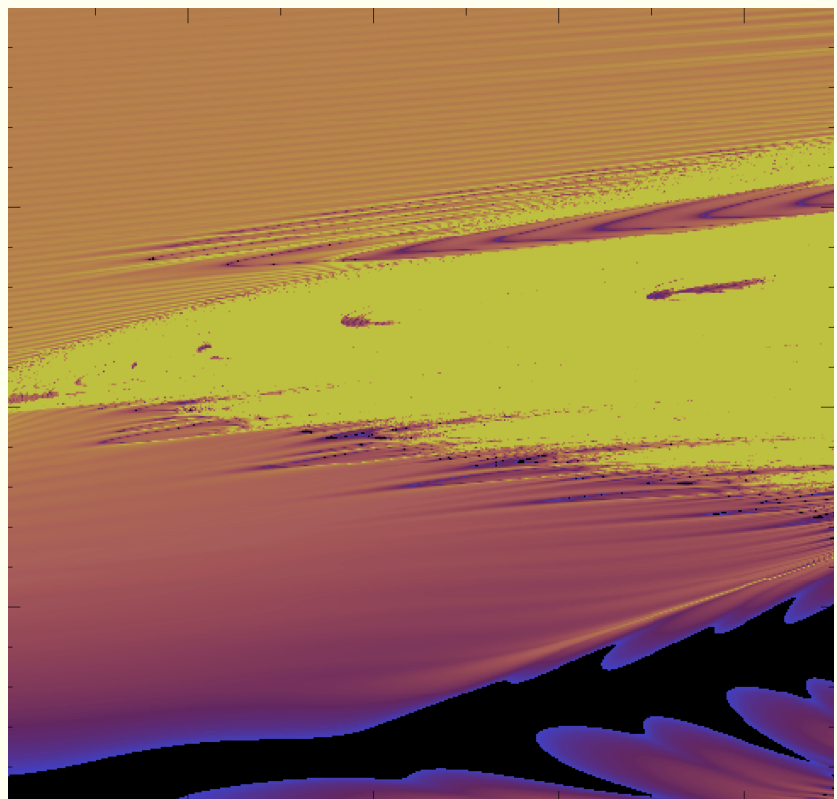


Acta Futura

Issue 4

A journal on future visions



Advanced Concepts Team

<http://www.esa.int/act>



Cover image from “A Dynamical System Approach to Astrodynamics”, in this issue.

Publication: Acta Futura, Issue 4 (2011)

Editor-in-chief: Duncan James Barker

Associate editors: Dario Izzo
Jose M. Llorens Montolio
Christos Ampatzis
Pacôme Delva
Francesco Biscani

Published and distributed by: Advanced Concepts Team
ESTEC, PPC-PF
2201 AZ, Noordwijk
The Netherlands
www.esa.int/gsp/ACT/publications/ActaFutura
Fax: +31 71 565 8018
D.O.I.: xx.xxxx/ACT-BOK-AF04

Copyright ©2011 - ESA Advanced Concepts Team

Typeset with X_ET_EX

Contents

Foreword	7
Toward Neuromorphic Odor Tracking: Perspectives for space exploration <i>E.M.Moraud and E. Chicca</i>	9
Orbits of artificial nanoparticles in the interplanetary medium: the influence of Lorentz force <i>I. Mann and A. Czechowski</i>	21
Towards an on-chip optically integrated array of superconducting detectors for sub-mm and FIR astrophysics <i>J. Bueno, N. Llombart, J.L. Costa-Krämer</i>	25
A relativistic navigation system for space <i>A. Tartaglia, M. Ruggiero and E. Capolongo</i>	33
Artificial Curiosity for Autonomous Space Exploration <i>V. Graziano, T. Glasmachers, T. Schaul, L. Pape, G. Cuccu, J. Leitner and J. Schmidhuber</i>	41
A Dynamical System Approach to Astrodynamics <i>A. Celletti and C. Lhotka</i>	53
Epitaxial quantum dots for sunlight harvesting <i>D. Alonso-Álvarez, B. Alén and J. M. Ripalda</i>	69
Micro-to-Macro: Astrodynamics at Extremes of Length-scale <i>C.R. McInnes, M.Ceriotti, C. Colombo, J. Sanchez, R. Bewick, J. Heiligers and C. Lücking</i>	81

Foreword

THE natural inquisitiveness of the human mind is the fundamental driving force for scientific discovery. Mankind feels the need , the urge to explore the unknown. Since the dawn of man's intelligence he has stared at the stars in awe and wonder. Space is still largely unknown to mankind and therefore stirs his imagination like no other thing. It is the largest unexplored frontier, and hence captures the human imagination and spurs him to ever greater achievements.

Scientific innovation comes from necessity. Exploration necessitates innovation. Therefore space not only inspires exploration, it requires innovation. Space is the only thing which can capture the imagination of man while simultaneously requiring vigorous innovation. The inspiration offered by the frontier of space, coupled with its innate need for innovation results in one of the largest and most dynamic scientific fields of research.

The studying of space sciences can involve extremes length scales, such as the research of particle interactions in the early hot universe and the long term evolution of clusters of galaxies. The space sciences can hold the answers to the "big" questions of science such as "how did our universe begin?", "what is the long term structure and stability of our universe?" and "are there any other universes separate from ours and do we interact with them?". In the future, space can also help solve some of the problems which plague mankind such as over- population, material and energy shortages by colonizing other planets and mining them for resources. Therefore space not only holds the wonder of the human imagination because of its unknown vastness, but it is vital to answering our fundamental questions about the universe and may help solve problems of material shortage and over-population.

The topics of the articles in this issue were chosen based the teams expert knowledge in the field of space science. The articles reflect the most promising topics in space science at the moment including such concepts as relativistic navigational systems, artificial nano-particles in space and neuromorphic detection and navigation systems.

Duncan James Barker
(Editor-in-chief)

<http://www.esa.int/act>
act@esa.int



Acta Futura 4 (2011) 9-19

DOI: 10.2420/AF04.2011.09

**Acta
Futura**

Toward Neuromorphic Odor Tracking: Perspectives for space exploration

EDUARDO MARTIN MORAUD^{*} AND ELISABETTA CHICCA[†]

^{}Advanced Concepts Team, ESA-ESTEC, 2200 AG Noordwijk, The Netherlands*

[†]Institute for Neuroinformatics, University of Zurich and ETH Zurich, 8006 Zurich, Switzerland

Abstract.

Autonomy is an essential factor to maximize the scientific return of exploratory missions, and it increasingly motivates the development of intelligent technologies that reduce the need for remote control or human supervision. This is the case for instance in the fields of rover navigation or on-board science analysis for planetary exploration. Interestingly, some of the tasks involved in such endeavors are also faced and efficiently solved by biological systems in nature, e.g. the animal olfactory system is able to autonomously detect and track cues (molecules) over long distances; it can robustly cope with sparse or noisy data, and it requires low computational complexity and energy consumption. On account of such capabilities, technologies that find inspiration in the neural architecture of biological systems present intrinsic advantages that give answers to the requirements of space environments. This paper outlines recent work in the fields of bio-inspired autonomous navigation and neuromorphic chemical sensing. We envision that these two approaches can be merged to produce novel techniques for autonomous exploration in space applications.

1 Introduction

For decades space exploration has been involved with searching for traces of past or present life and water on other planets along with measuring geophysical parameters relevant to planetary evolution. Examples of upcoming exploratory missions sharing these goals include the ‘ExoMars’ mission led by ESA, which will perform measurements of the Martian soil and rocks, collecting and analyzing particles by means of a surface Rover [39]. Likewise, the NASA ‘ARES’ Mission will study the atmospheric composition of the red planet using an Unmanned Air Vehicle (UAV) that will be flown through the near-surface atmosphere while collecting samples of its chemistry and dynamics [34].

Common to all aforementioned tasks is required to detect and track chemical components in an unknown environment. This involves several challenges. First, relevant particles or blends are to be detected and discriminated on-line. Precise gas sensor technologies and on-board analysis are required to classify relevant molecules in real time, thereby coping with their short-time scale, high dimensionality and quickly changing amplitude [15]. Traditional pattern recognition models based on attractor states may prove too slow for such purposes.

Secondly, exploration needs to be driven toward ar-

^{*}E-mail: emartimoraud@ieee.org

[†]E-mail: chicca@ini.phys.ethz.ch

eas of high scientific impact. Navigation must be autonomous and efficient, able to deal with data that is sparse, noisy and subject to turbulence. Note, that in real environments, patches of high concentration are constantly surrounded by wide voids where no relevant information is available. This makes navigation a complicated task for which simple approaches (e.g., gradient-based) fail, since gradients constantly fluctuate in magnitude and direction, and do not point toward the source [35].

When considering space applications, additional constraints must be accounted for, namely, limited energy consumption and physical space. Computational complexity must thus be kept to a minimum.

Interestingly, olfactory source localization is a common task in nature, and many animals constantly solve it to locate food or find mates with high accuracy and limited resources [26]. Moth and Bacteria are among the most illustrative and better documented examples of scent tracking. The former use their antennae to detect pheromones released by females, and employ them to track the plume toward their mate [2]. Bacteria on the other hand rely on local searches to move toward a source of nutrients [3]. To this date, neither the discrimination capabilities achieved by biological systems, nor their efficiency in exploration, have been replicated by artificial counterparts.

Several biomimetic solutions have attempted to draw inspiration from nature, and to apply them to robotics as an alternative to classic engineering approaches [14, 30]. Of particular interest, neuromorphic technologies mimic the *architectural structures* present in the nervous system. They are usually implemented in analogue circuits that consume little power and they exploit parallel computation which allows real-time performances. Such concepts provide an ideal technical framework to deal with the requirements of space applications. Recent successful applications include neuromorphic vision-based spacecraft landing, derived from insect optic flow strategies, and integrated within Very Large Scale Integration (VLSI) sensors [27, 22].

In this paper, we report advances in both neuromorphic chemical detection and autonomous navigation. We further outline how, when combined, such techniques may prove valuable in the framework of planetary exploration.

2 Robot navigation

2.1 Toward full autonomy

Intelligent decision-making in space unmanned vehicles is essential to overcome the limitations caused by communication delays and overloaded bandwidths. It allows the exploration of distant planets without direct human supervision, and thereby to replace impractical remote control [1].

To this day, however, autonomous navigation has been mostly limited to providing basic behaviours, e.g. obstacle-avoidance or detection of traversable areas. Higher-level behaviours that require scientific expertise and long-term plans (as is the case when seeking chemicals) are still human controlled. Additional autonomy has recently been deployed using planning and scheduling techniques [38, 10, 6] in order to flexibly *redirect* exploratory paths on-line, and thereby to account for new features of interest discovered along the way. Yet this is only local and with limited range of action within the pre-established long-term plan outlined from Earth. Fully automating exploratory operations would require that the whole navigation toward promising areas be decided onboard by the agent itself, guided by interactions with its environment and motivated by an intrinsic interest in the final goal.

Completely autonomous source localization has been attempted on Earth through a variety of techniques, either purely probabilistic or inspired from biological systems. The former uses intelligent sensing and planning to reason about the world, but it often suffers from the sparseness of information far from the source, and it proves to be truly efficient in dense conditions only, i.e. close to the source where the plume can be considered as a continuous cloud [28]. Bio-inspired approaches, on the other hand, can yield impressive results even far from the source [17, 14, 29], but often address the problem only from a *behavior imitation* perspective, i.e. they mimic the choices performed by animals through a rule-based approach, regardless of the mechanism from which the behavior emerges. This raises the question of how well such strategies may be adapted to new scenarios (if at all) or even be optimized when considering added constraints such as those imposed by space. A proper adaptation would instead require tuning and rewiring the underlying neural architecture.

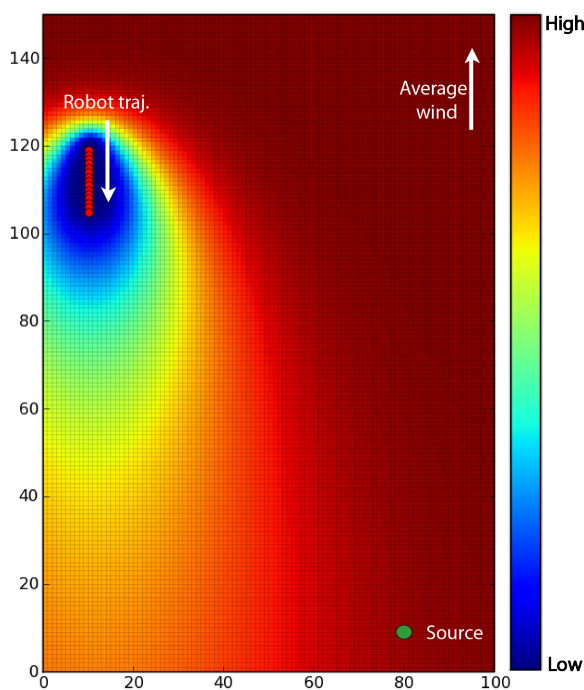


FIGURE 1. *Infotaxis.* Example of belief (probability map) for the location of the source after 10 steps (red dots). No ‘cues’ are detected in that time. Locations in front of the agent become less probable as the agent navigates forward without encounters, thereby increasing the likelihood of locations on the sides. The shape of the belief (Gaussian-like) is inferred from the physics description of how cues spread in the environment when transported by the wind.

2.2 Infotactic strategies

Infotaxis [40] conveys the advantages of both approaches previously mentioned. It is based on Reinforcement Learning (RL) approaches, and fully exploits the capabilities of autonomous on-line learning. The agent discovers the direction leading to the source by iterative interactions with its environment, driven by a decision-making strategy that efficiently combines exploratory patterns with information exploitation.

Interestingly, although animal patterns are not pre-programmed or imposed through explicit rules of movement, behaviors such as casting or zigzagging (extensively documented in moths) do actually emerge naturally from the underlying architectural model [20]. This represents a promising baseline from which to derive extended strategies, adapted to other scenarios. As a

matter of fact, even though initially restrained to the problem of scent tracking, infotaxis actually embodies a *general* framework for intelligent navigation and source localisation with sparse cues. Its core components are outlined hereafter.

Algorithmic foundations.

Infotaxis is built around two core components: Uncertainty modeling and decision-making. The former is achieved through an internal description of the world (physical description of how cues spread in turbulent environments when transported away from the source), which can be used to interpret encounters and thereby to infer the likelihood for the source to be at a given location.

In the scenario considered in [40] (odor cues spread in an open environment), the internal model corresponds to the spatio-temporal profile of odor plumes (as derived from the equations of diffusion-advection). Since molecule dispersal is subject to high degrees of turbulence and randomness, a detailed description of the environmental dynamics is unfeasible; instead, a time-average distribution of the detection-rate R is calculated, to which a random component is added, i.e. actual encounters are sampled independently from a poisson-distributed variable.

Based on this physical model, a *probabilistic belief* is built (Fig. 1) given the trace of past perceptions (in a similar way to [28]). Note that both encounters and non-encounters provide information and are used to iteratively update the belief, which is then relied upon for the decision-making. The strategy attempts to maximize the expected amount of ‘knowledge’ acquired in the next step, as quantified in terms of the entropy of the aforementioned probabilistic map. Note that this differs from classical approaches in that the agent does not directly target the most likely location for the source, but rather the one where he expects to ‘learn’ more about its surroundings.

The (expected) uncertainty in future steps is derived from two terms: A first term which evaluates the *probability of finding the source*, and a second one which computes the *amount of knowledge* gathered even if the source is not found. The first term corresponds to the exploitative choice; the robot chooses to go in the direction that maximises its (expected) chances of finding the source (regardless of other considerations) whereas the second term represents the explorative decision which pushes the robot to go to regions where it might detect

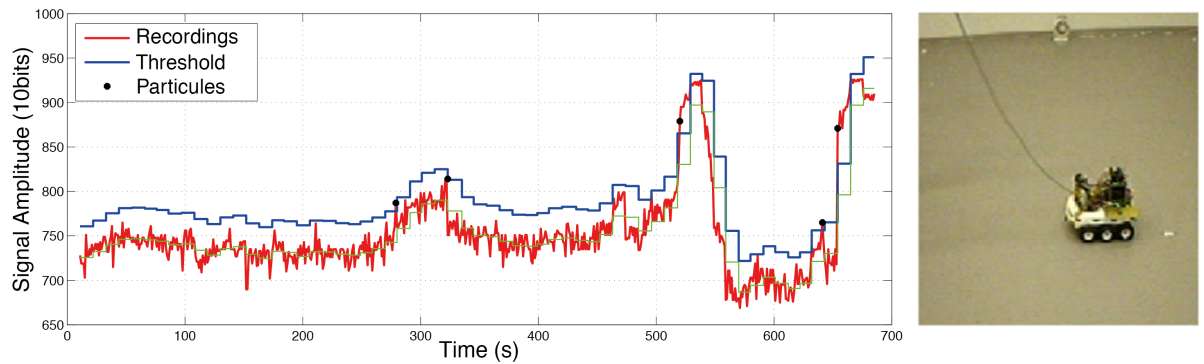


FIGURE 2. *Left.* Real recordings (red) with a heat sensor at sampling frequency $f = 10\text{Hz}$, and derived ‘cues’ (black dots) to be employed by infotaxis when guiding the search. A moving window (blue) is used to filter the signal while preventing consecutive correlated hits from being overcounted, thereby ensuring that ‘cues’ are appropriately derived from the sensor measurements *Right.* Experimental setup, koala robot endowed with the sensor, and heat source.

new cues (regardless of whether the source is actually believed to be in that direction or not). This balance is essential for the strategy to be effective and provides the model with a robustness that makes it especially suitable for turbulent environments. Its efficiency was shown indeed to outperform more classical approaches [40]. Note that the horizon considered when predicting rewards consists of a single step, but could easily be extended to account for elaborated planning.

2.3 Facing real environments

We addressed the problem of verifying that infotactic strategies may prove equally efficient under real experimental conditions. It is well known that matching the complexity of the world in computational models is highly challenging, and usually it is necessary to make simplifications or assumptions to help make the problem tractable. On the contrary, robotic agents are confronted with the real environment and hence provide a testbed to assert complete and rigorous results. It is also an essential step to ensure that algorithmic concepts can be implemented with the available technology and employed for real-world applications.

The key point at the core of infotaxis is the randomness of odor encounters. This randomness is explained by the turbulence of the medium (particles spread through diffusion-advection), and it motivates the use of an uncertainty-minimisation approach. Cues are modeled in simulation through stochastic mathematical descriptions, and it is assumed that they are independent and uncorrelated. Yet in reality an odor

patch covers a certain volume and presents extended spatiotemporal characteristics. Even though inherently random, this structure will give rise to consecutive non-independent ‘cues’. For infotaxis to be fully efficient, consecutive detections should not be overcounted. In [24], we calculated the posterior probability distribution from a modified model that accounts for correlated hits, and is built around *transitions* from no-detection to detection rather than on single hits. In our implementation, this is achieved by means of an adaptive filter, calculated over a moving time-window (Fig. 2).

Furthermore, electronic sensors must be chosen so that the requirements of the model (in terms of sensitivity and speed) are met. Because odor sensors usually require long degassing times and saturate easily, they are unable to respond to the requirements of infotaxis. We chose as an alternative to use heat sensors, which do not saturate easily and react at high speed. We note that the spatiotemporal distribution of heat is identical to that of odor, and thus no loss of accuracy is brought in by this adaptation. Alternative solutions for chemical sensing that draw inspiration from the animals neural information system are further outlined in section 3, along with their advantages.

Infotaxis robustness and effectiveness was then tested by means of a real robotic framework (Fig. 2 – right). Identical distributions were obtained, both for the search time required until finding the source, and for the number of encounters required (Fig. 3), thus ensuring that its main properties are preserved when applied in reality. Note also that the internal model relied upon

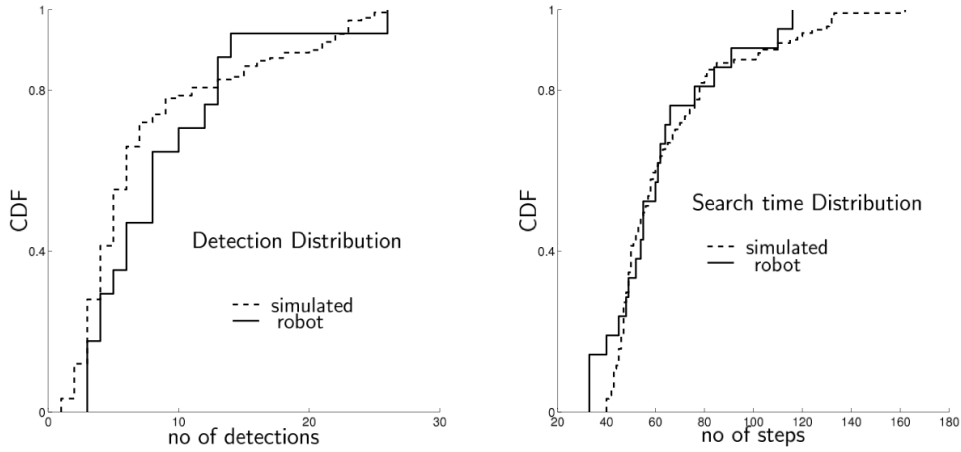


FIGURE 3. Comparison of robotic and simulated results: cumulative distribution of the number of steps until finding the source (left) and of the number of cues required to reach the goal (left).

by the agent requires parameters such as wind speed and direction. Which in reality may vary over time and differ from the estimated ones. The robustness of infotaxis was thus evaluated even with respect to *inaccurate* modeling by the agent; the parameters were not fine-tuned or adapted on-line, yet despite this discrepancy the robot was able to find the source within reasonable time limits.

The biomimetic characteristics of the navigation were also preserved in our robotic implementation. Robot trajectories were shown to exhibit animal-like patterns such as ‘extended cross-wind’ or ‘zigzag upwind’ [24]. The track angle histogram also maintains a distribution similar to that observed in moths.

3 Artificial olfaction

Molecule sensing and discrimination is being deployed in a range of space projects. Examples of on-board analysis and recognition include the Mars Organic Molecule Analyzer (MOMA) embedded within the ExoMars rover, that will analyze gases in the Martian atmosphere, attempting to separate and identify specific components. Complementary approaches that help facilitate this task would prove highly useful.

In this regard, it has been suggested that the animal olfactory system exploits network dynamics to improve the recognition of different inputs. They make use of the transient response and decorrelate different inputs by *mapping* them into a higher dimensional space that

exploits the number of possible spatio-temporal combinations [30]. Under this grounding premise, recognition models built out of a similar structure could prove extremely efficient for real applications. Neuromorphic engineering is therefore a promising tool for building odor classification systems.

This technology may also be implementable as part of gas sensor employed in every day-life problems (e.g., CMOS). Progress so far in this direction has been hindered by the high price of these devices, and considerable effort has been devoted to developing low-cost gas sensors using CMOS technology, and combining them with MEMS for instance. This has led to the implementation of low-power smart gas sensors. A recent review by Gardner et al. [12] summarizes the main latest achievements in the field of integrated CMOS gas sensors.

3.1 Neuromorphic computation for olfactory systems

Neuromorphic VLSI devices comprise hybrid analog/digital circuits that implement hardware models of biological systems, using computational principles analogous to the ones used by nervous systems [21].

During the last decade the neuromorphic engineering community has made substantial progress by developing the technology for constructing distributed multi-chip systems of sensors and neuronal processors that operate asynchronously and communicate using action-

potential-like signals (or spikes) [7, 23]. The main advantages of VLSI networks of spiking neurons permit the embodiment of this platforms on robotic devices, providing the circuits with realistic inputs which are affected by the interaction of the robot with the environment.

Recent advances in chemosensors [12], a better understanding of the signal processing principles of biological olfactory systems and progress in the technology for constructing distributed spiking multi-chip neuromorphic systems, have made it possible to consider implementing compact, low-power, biologically inspired neuromorphic olfactory systems.

These systems are often modular. The sensing (see [32] for a recent review), the signal processing (e.g., [31]) and the artificial neural network pattern recognition system (e.g., [9, 33]) are implemented separately using various technological means (sensors with different transducer principles, conventional software algorithms, general purpose digital computing devices and custom hybrid analog/digital VLSI devices).

Within the biologically inspired olfactory systems proposed in the literature the most representative example of a neuromorphic olfaction device was recently suggested by Koickal et al. [13]. They presented a fully integrated neuromorphic olfaction chip comprising a chemosensor array, a signal conditioning circuitry and a spiking neural architecture with on-chip spike time dependent plasticity [19].

We propose a modular neuromorphic approach for testing olfactory coding and signal processing hypothesis derived from the study of insects. The long term goals of this research include the development of novel algorithms for chemical sensor data classification based on principles extracted from biological olfactory systems.

The choice for modularity provides two main advantages in comparison to a fully integrated neuromorphic olfaction chip:

1. commercially available chemical sensor arrays can be easily integrated in the neuromorphic system.
2. possibility to test different network topologies by means of spiking multi-neuron Address Event Representation (AER) chips and the related hardware infrastructure¹.

¹In recent years we have witnessed the emergence of new asynchronous communication protocols that allow aVLSI neurons to transmit their activity across chips using pulse-frequency modulated signals (in the form of events, so-called spikes). One of the most common asynchronous communication protocols used in these types of

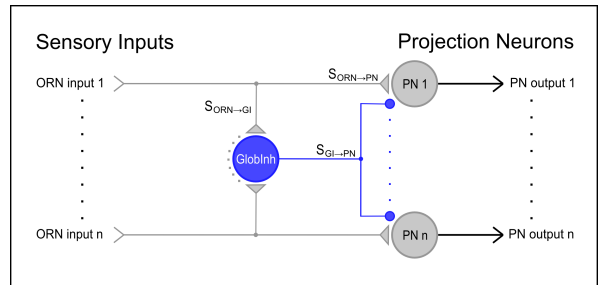


FIGURE 4. Simplified model of the AL studied in [4]. Small triangles: excitatory connections. Small circles: inhibitory connections. Weights of excitatory and inhibitory connections (gray and blue pathways) are the only free parameters used to study the behavior of the network.

The olfactory system of insects provides an ideal substrate for studying the information processing in biological neural networks for several reasons. Firstly, it is a ‘small’ system, i.e. the first olfactory relay in insects, the Antennal Lobe (AL), consists of a relatively small number (ca. 50 in *Drosophila*) of functionally distinct processing units or glomeruli. Secondly, it exhibits a stereotyped connectivity; the glomeruli are zones of high synaptic convergence between the axons of one type of Olfactory Receptor Neurons (ORN) and the dendrites of a few Projection Neuron (PN) projecting to higher brain areas [41]. Finally, the odor code is conserved between individuals which is helpful for the systematic comparison and pooling of experimental results.

In the insect glomeruli, inhibitory modulation of the AL activity is achieved by the interaction of Local Interneuron (LN) with ORN and PN. These intra-AL connections have a significant influence on the processing of information in the AL [42, 37]. The role of these inhibitory networks in shaping and processing olfactory information is not fully understood, despite a number of studies that have illustrated the importance of inhibition in the AL. In [4], we studied a network architecture with feed-forward global inhibition based on a previous study by Silbering and Galizia [36] (see Fig. 4) by using a linear model, a spiking software simulation and a neuromorphic implementation.

We used the linear model to provide a complete char-

systems is based on the AER [18]. Systems containing more than one AER chips can be assembled using off-chip arbitration and lookup tables to map address-events from one chip to another, implementing arbitrary network topologies. Infrastructures for constructing multi-chip pulse-based neuromorphic systems based on AER have been developed by several researchers (e.g., [5, 8, 25, 11, 7]).

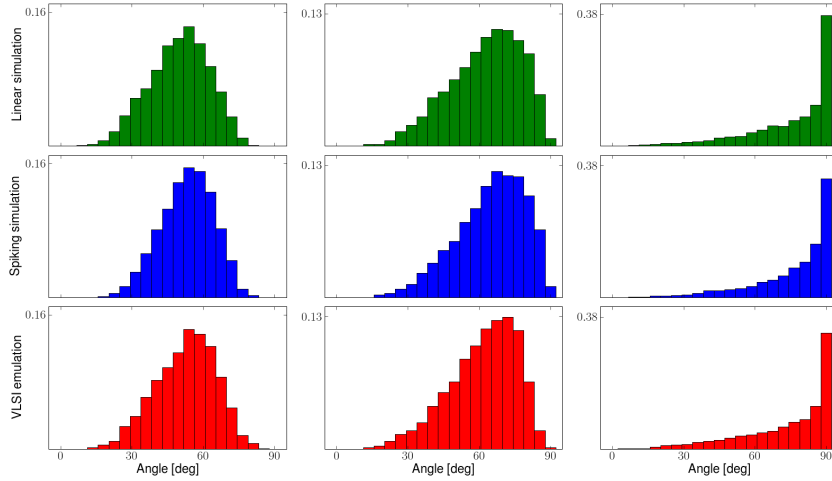


FIGURE 5. Histogram of angles between activation vectors of odor pairs for the three simulations (rows) and for three values of inhibition strength (columns) presented in [4]. Increasing inhibition strength (from left to right) produces a shift of the angle distribution toward the 90 degrees limit, therefore increasing odor discriminability.

acterization of the parameter space. The spiking simulation on the other hand provides the advantage of including the temporal dynamics in the model but has the drawback of being computationally intensive, especially for large network simulations. Alternatively, the neuromorphic VLSI emulation has the advantages of the spiking simulation in a compact, low-power, real-time system.

As shown in Fig. 5, we compared the behavior of the network in response to calcium concentrations measurements of odor responses in *Drosophila Melanogaster* for the three different simulation approaches.

One hypothesis about the role of the AL in the olfactory processing stream is to increase odor discriminability. In the AL, all axons with the same receptor expression profile converge onto a single glomerulus [41], so that the array of activity values of each ORN for a given odor represents a vector in a multidimensional space. Intuitively, we can consider the Euclidean angle between pairs of vectors as a measure of odors proximity, thus the network should increase angles to improve odor discriminability.

The table in Fig. 5 presented in [4] shows the distribution of angles (computed for all possible odor pairs) for the three simulations (rows) and for three values of inhibition strength (columns). When inhibition is disabled (left column) the PNs angle histogram is identical to the input (ORN) angle histogram for the linear simulation (top graph). When inhibition is enabled (center

column) an average increase in angles between odors is observed in the three models. This network effect can be increased by increasing the strength of inhibition (right column).

These results showed that inhibition could be used by the AL to increase angles between odor pairs and therefore improve odor discriminability. The three models show comparable results.

Apart from studying the role of local inhibition in the AL, this work was very useful to establish a hardware framework for implementing models of olfactory computation. The neuromorphic neural network studied in [4] can be used as a preprocessing stage for an odor classifier. We are currently investigating a neuromorphic system for odor classification using the same data presented in [4], and comparing the classifier performance on the network's input and output data.

4 Perspectives for space

Infotactic navigation strategies have been tested so far in the case of olfaction only, i.e. for scent-tracking and odor-source localization. Nevertheless, the concept only requires certain features to work (cues encountered along the way as the agent navigates, providing information about where the source is more likely to be, along with a model of the environmental dynamics), and it hence represents a quite general approach that may be applicable to different scenarios with equal degrees of

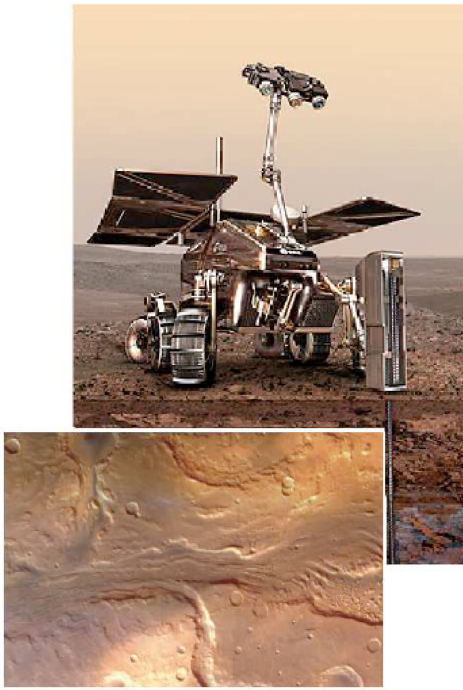


FIGURE 6. Exomars rover [39] and riverbed along which fully autonomous water-source localisation may be considered.

success.

Under such premise, it may be of interest to consider whether similar approaches could be used for space-related applications as the ones outlined in the introduction, for instance in the framework of finding footprints of biological activity. A key point is that the goal is treated as a source that spreads cues in the environment in a way that can be modeled, and relied upon when reasoning. Rover infotactic navigation would help guide the search toward areas of scientific interest (e.g., a crater, or the source of a dry river - Fig. 6).

These navigation strategies must be supported by on-board detection and real-time classification of chemical components. Integrated sensors and neuromorphic olfactory systems described above are ideal candidates for achieving these demanding tasks. The results presented in [4], summarized in section 3, provide a promising substrate for exploring hardware implementation of real-time chemical detection and classification devices. Furthermore, the neuromorphic technology can guarantee low-power consumption and compactness, essential for space applications. In particular, the hardware framework presented in [4] is relevant for robotic scent tracking in space exploration for the following reasons:

1. The neuromorphic chips used are massively parallel and operate in real time, regardless of the size of the implemented neural network.
2. The analog circuits modelling spiking neurons and dynamic synapse are operated in the transistor's subthreshold regime [16], therefore producing currents of the order of pico-Amperes and leading to very low power consumption.
3. Miniaturized systems can be implemented after a prototyping phase used to explore different architectures.
4. The spiking neural networks implemented in our neuromorphic chips can exploit temporal dynamic analogues to those observed in biology to achieve improved odor classification.

5 Conclusion

We have presented both software and hardware bio-inspired alternatives to classical robot navigation and odor-sensing processing. These exploit the structure of neural systems, their low energy consumption and small size, making them very well adapted to the requirements of space applications. Specifically we envision that implementing infotactic navigation supported by neuromorphic sensing and processing will lead to efficient and robust strategies that could allow full autonomy to be contemplated in exploratory rovers. These would intelligently guide the search for chemicals without human supervision.

In addition, alternative applications that go beyond mere odor recognition and tracking may also be considered. The presented models can be extended to account for additional constraints and scenarios, and may therefore be considered as a baseline from which to derive global searching strategies with sparse or noisy cues. Examples could include autonomous satellite guidance, or extensions that cope with limited measuring capabilities. Note that these may be included in the model as constraints, which might lead to substantial changes in the strategies adopted depending on the reward-to-cost ratio considered.

Acknowledgment

This work was supported by the EU ICT Grant ICT-231168-SCANDLE “acoustic SCene ANalysis for Detecting Living Entities”.

We thank the Advanced Concepts Team of the European Space Agency, where the presented ideas on autonomous navigation were initially discussed. We also thank Matthew Cook and Giacomo Indiveri for proofreading this manuscript and providing valuable feedback.

References

- [1] M. Bajracharya, M. W. Maimone, and D. Helmick. Autonomy for mars rovers: Past, present, and future. *Computer*, 41:44–50, 2008.
- [2] J. Belanger and E. Arbas. Behavioral strategies underlying pheromone-modulated flight in moths: lessons from simulation studies. *J. Comp. Physiol. A*, 183:345–360, 1998.
- [3] H. C. Berg. Bacterial behaviour. *Nature*, 254:389–392, April 1975.
- [4] M. Beyeler, F. Stefanini, H. Proske, G. Galizia, and E. Chicca. Exploring olfactory sensory networks: Simulations and hardware emulation. In *Biomedical Circuits and Systems Conference BIOCAS 2010*, pages 270–273. IEEE, 2010.
- [5] K. A. Boahen. Point-to-point connectivity between neuromorphic chips using address-events. *IEEE Transactions on Circuits and Systems II*, 47(5):416–34, 2000.
- [6] A. Castano, A. Fukunaga, J. Biesiadecki, L. Neakrase, P. Whelley, R. Greeley, M. Lemmon, R. Castano, and S. Chien. Automatic detection of dust devils and clouds on mars. *Machine Vision and Applications*, 19(5):467–482, 2008.
- [7] E. Chicca, A. M. Whatley, V. Dante, P. Lichtsteiner, T. Delbrück, P. Del Giudice, R. J. Douglas, and G. Indiveri. A multi-chip pulse-based neuromorphic infrastructure and its application to a model of orientation selectivity. *IEEE Transactions on Circuits and Systems I*, 5(54):981–993, 2007.
- [8] S. Deiss, R. Douglas, and A. Whatley. A pulse-coded communications infrastructure for neuromorphic systems. In W. Maass and C. Bishop, editors, *Pulsed Neural Networks*, chapter 6, pages 157–78. MIT Press, 1998.
- [9] T. A. Dickinson, J. White, J. S. Kauer, and D. R. Walt. An olfactory neural network for vapor recognition in an artificial nose. *Biological Cybernetics*, 382:697–700, 1996.
- [10] T. Estlin, D. Gaines, C. Chouinard, R. Castano, B. Bornstein, M. Judd, I. Nesnas, and R. Anderson. Increased mars rover autonomy using ai planning, scheduling and execution. In *IEEE International Conference on Robotics and Automation*, 2007.
- [11] S.-G. et al. AER building blocks for multi-layer multi-chip neuromorphic vision systems. In S. Becker, S. Thrun, and K. Obermayer, editors, *Advances in Neural Information Processing Systems*, volume 15. MIT Press, Dec 2005.
- [12] J. W. Gardner, P. K. Guha, F. Udrea, and J. A. Covington. CMOS interfacing for integrated gas sensors: A review. *IEEE Sensors Journal*, 10(12):1833–1848, 2010.
- [13] T. J. Koickal, A. Hamilton, S. L. Tan, J. A. Covington, J. W. Gardner, and T. C. Pearce. Analog VLSI circuit implementation of an adaptive neuromorphic olfaction chip. *IEEE Transaction on Circuits and Systems I*, 54(1):60–73, 2007.
- [14] G. Kowadlo and R. A. Russell. Robot odor localization: A taxonomy and survey. *Int. J. Rob. Res.*, 27(8):869–894, 2008.
- [15] G. Laurent. Olfactory network dynamics and the coding of multidimensional signals. *Nature Reviews Neuroscience*, 1:884–895, November 2002.
- [16] S.-C. Liu, J. Kramer, G. Indiveri, T. Delbrück, and R. Douglas. *Analog VLSI: Circuits and Principles*. MIT Press, 2002.
- [17] T. Lochmatter, X. Raemy, L. Matthey, S. Indra, and A. Martinoli. A Comparison of Casting and Spiraling Algorithms for Odor Source Localization in Laminar Flow. In *Proceedings of the 2008 IEEE International Conference on Robotics and Automation (ICRA 2008)*, pages 1138–1143, 2008.
- [18] M. Mahowald. *VLSI analogs of neuronal visual processing: a synthesis of form and function*. PhD thesis, Department of Computation and Neural Systems, California Institute of Technology, Pasadena, CA., 1992.

- [19] H. Markram, J. Lübke, M. Frotscher, and B. Sakmann. Regulation of synaptic efficacy by coincidence of postsynaptic APs and EPSPs. *Science*, 275:213–215, 1997.
- [20] D. Martinez. On the right scent. *Nature*, 445:371–372, January 2007.
- [21] C. Mead. *Analog VLSI and Neural Systems*. Addison-Wesley, Reading, MA, 1989.
- [22] V. Medici, G. Orchard, S. Ammann, G. Indiveri, and S. Fry. Neuromorphic computation of optic flow data. Technical Report - Ariadna 08/6303, European Space Agency, the Advanced Concepts Team, 2010.
- [23] P. Merolla, J. Arthur, B. Shi, and K. Boahen. Expandable networks for neuromorphic chips. *IEEE Transactions on Circuits and Systems I*, 54(2):301–311, Feb. 2007.
- [24] E. M. Moraud and D. Martinez. Effectiveness and robustness of robot infotaxis for searching in dilute conditions. *Frontiers in Neurorobotics*, 4(0):12, 2009.
- [25] A. Mortara, E. Vittoz, and P. Venier. A communication scheme for analog VLSI perceptive systems. *IEEE Journal of Solid-State Circuits*, 30:660–9, 1995.
- [26] J. Murlis, J. S. Elkinton, and R. T. Carde. Odor plumes and how insects use them. *Annual Review of Entomology*, 37:479–503, January 1992.
- [27] G. Orchard, C. Bartolozzi, and G. Indiveri. Applying neuromorphic vision sensors to planetary landing tasks. In *Biomedical Circuits and Systems Conference, BIOCAS 2009*, pages 201–204. IEEE, 2009.
- [28] S. Pang and J. A. Farrell. Chemical plume source localization. *IEEE Transactions on Systems, Man, and Cybernetics, Part B: Cybernetics*, 36(5):1068–1080, Oct. 2006.
- [29] P. Pyk, S. B. I. Badia, U. Bernardet, P. Knüsel, M. Carlsson, J. Gu, E. Chanie, B. S. Hansson, T. C. Pearce, and P. F. J. Verschure. An artificial moth: Chemical source localization using a robot based neuronal model of moth optomotor anemotactic search. *Auton. Robots*, 20:197–213, June 2006.
- [30] M. Rabinovich, R. Huerta, and G. Laurent. Transient Dynamics for Neural Processing. *Science*, 321(5885):48–50, 2008.
- [31] B. Raman, P. A. Sun, A. Gutierrez-Galvez, and R. Gutierrez-Osuna. Processing of chemical sensor arrays with a biologically inspired model of olfactory coding. *IEEE Transaction on Neural Networks*, 17(4):1015–1024, 2006.
- [32] F. Röck, N. Barsan, and U. Weimar. Electronic nose: current status and future trends. *Chemical Reviews*, 108(2):705–725, 2008.
- [33] T. Roppel and D. M. Wilson. Biologically-inspired pattern recognition for odor detection. *Pattern Recognition Letters*, 21:213–219, 2000.
- [34] S. P. Sandford, M. A. Croom, R. W. Moses, C. A. Kuhl, M. D. Guynn, R. D. Braun, and J. S. Levine. ARES and beyond - autonomous aerial platforms provide a unique measurement capability for earth and planetary science. In *2nd AIAA Unmanned Unlimited Systems, Technologies, and Operations*, September 2003.
- [35] B. I. Shraiman and E. D. Siggia. Scalar turbulence. *Nature*, 405:639–646, 2000.
- [36] A. F. Silbering and C. G. Galizia. Processing of odor mixtures in the drosophila antennal lobe reveals both global inhibition and glomerulus-specific interactions. *J. Neurosci.*, 27(44):11966–11977, 2007.
- [37] A. F. Silbering, R. Okada, K. Ito, and C. G. Galizia. Olfactory information processing in the drosophila antennal lobe: anything goes? *Journal of Neuroscience*, 28(49):13075–13087, December 2008.
- [38] T. Smith. *Probabilistic planning for robotic exploration*. PhD thesis, CMU The Robotics Institute, Pittsburgh, PA, USA, 2007.
- [39] J. Vago. Exomars: Searching for life on the red planet. *ESA bulletin*, 126:17–23, May 2006.
- [40] M. Vergassola, E. Villermaux, and B. I. Shraiman. Infotaxis as a strategy for searching without gradients. *Nature*, 445:406–409, 2007.

- [41] L. B. Vosshall, A. M. Wong, and R. Axel. An olfactory sensory map in the fly brain. *Cell*, 102:147–159, 2000.
- [42] R. I. Wilson, G. C. Turner, and G. Laurent. Transformation of olfactory representations in the drosophila antennal lobe. *Science*, 303(5656):366–370, January 2004.



Acta Futura 4 (2011) 21-23

DOI: 10.2420/AF04.2011.21

**Acta
Futura**

Orbits of artificial nanoparticles in the interplanetary medium: the influence of Lorentz force

INGRID MANN^{*} AND ANDRZEJ CZECHOWSKI[†]

^{*}*Belgian Institute for Space Aeronomy, 3 Avenue Circulaire, 1180 Brussels, Belgium*

[†]*Space Research Centre, Polish Academy of Sciences, Bartycka 18A, 00-716 Warsaw, Poland*

Abstract. It has been suggested to utilize solar radiation pressure acting on nanodust to facilitate transporting material in space (De Juan Ovelar *et al.* [5]). Dust particles in the interplanetary medium carry a surface charge and therefore in addition to the radiation pressure are influenced by Lorentz force. We show that the Lorentz force acting on nanodust in the solar wind and interplanetary magnetic field is difficult to predict and complicates the suggested “tailoring” of dust orbits.

1 Introduction

The radiation pressure force that acts on small dust particles in the interplanetary medium can be of the same order as the solar gravitation force (see *e.g.* Ref. [9]). Hence dust particles with suitable light scattering properties can be significantly influenced in their trajectories by the radiation pressure force. Optimizing light scattering properties of objects has been discussed as a means for space transportation by solar radiation pressure [6]. Based on considering the orbits of nanodust exposed to solar radiation, the “tailoring of nanodust trajectories” is suggested (De Juan Ovelar *et al.* [5]). The major forces acting on dust in the interplanetary

medium are gravity, radiation pressure and electromagnetic forces. For nanodust, both the latter forces are important. We address here the issue of the extent to which electromagnetic forces must be taken into account for the suggested “tailoring” of orbits.

2 Dust charging

Dust particles, as well as larger objects in the interplanetary medium, acquire a surface charge (see *e.g.* Ref. [8]). The charging processes in the interplanetary medium are emission of photoelectrons caused by in-falling solar radiation, sticking and recombination of plasma particles, secondary electron emission, thermionic emission and field emission. With photo ionization being the major process, dust and larger objects acquire a surface charge that corresponds to a positive potential, U , relative to the surrounding solar wind plasma of the order of 1 to 10 V that is roughly independent from size. With the surface charge $Q \sim Ua$, where a is the radius of the particle, the ratio of surface charge Q , to mass m , of the dust particles is $Q/m \sim 1/a^2$. The electromagnetic forces, being proportional to charge, for small sizes become more important compared to gravity. The exact amount of the carried charge depends on the size, shape and structure of the dust particles, the dust velocity relative to the plasma, the plasma temperature (which de-

^{*}E-mail address: ingrid.mann@aeronomie.be

[†]E-mail address: ace@cbk.waw.pl

fines the velocity distribution of in-falling plasma particles) and finally on the solar radiation flux, namely in the UV. Photoelectron emission, secondary electron emission and thermionic emission depend on dust material composition. The dust shape and structure may also influence charging.

The equilibrium surface charge is attained in timescales typically less than a day, nevertheless it is reasonable to assume that the real charge values vary around the equilibrium value. The surface charge corresponds to tens to a few hundreds e and assuming Poisson statistics leads to 20 percent charge differences for a given dust size. Variations of the solar wind parameters cause charge fluctuations of the same order. Though not showing any systematic variations with the solar cycle, the dust surface charge follows temporal variations of solar wind parameters on short time scales. A model calculation by Kimura and Mann [7] that was based on measured solar wind parameters which followed the surface charge of carbon and silicate dust particles at 1 AU. The calculations show that the surface charge of the silicate dust increases by up to roughly 20 percent for solar wind conditions with low plasma density, high temperature, and high bulk velocity.

3 Dust trajectories

Based on the considerations of surface charge we estimate that the particle trajectories should not vary much for variations of the surface charge of 20 percent. This should account for stochastic variations and for variations in charge due to solar wind variations. Let us assume that the dust particles can be released from the spacecraft, since the spacecraft potential is typically of the same order as the dust. After being released, the different charging currents provide an average equilibrium potential, but the dust charges of released grains vary around this value. We consider the case of trajectories similar to those previously discussed in Ref. [5] for the transport of particles on time scales of the order of 100 days.

For the trajectory calculations we follow the equation of motion used by Czechowski and Mann [4]. This includes gravity, radiation pressure and Lorentz force in the Parker solar magnetic field model as given there. The radiation pressure to gravity ratio is 0.4 and the particles are all released at solar distance 0.9 AU from circular Keplerian orbit. The charge varies around the typical value for 100 nm grains of 10^{-7} e/m_p (*i.e.* elementary

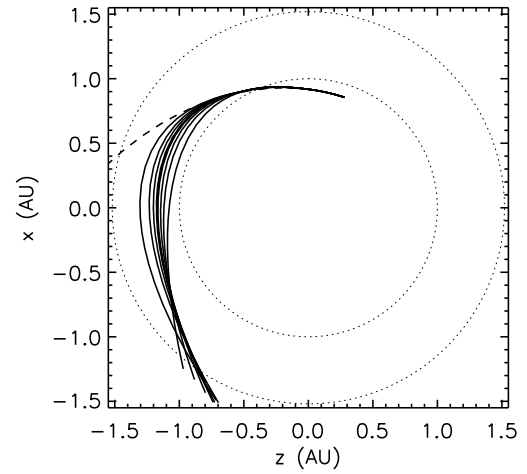


FIGURE 1. Calculated dust trajectories projected onto the ecliptic plane. The dashed line is for an electrically neutral particle ($Q/m = 0$) with radiation pressure to gravity ratio $\beta = 0.4$. The solid lines correspond to the same beta value and the values of Q/m equal to $(0.8, 0.9, 0.95, 1.0, 1.01, 1.05, 1.1 \text{ and } 1.2) \times 10^{-7} \text{ e}/m_p$, respectively. The projections of the orbits of Earth and Mars are shown by the dotted lines.

charge per proton mass $10^{-7} \text{ e}/m_p \approx 10 \text{ C/kg}$). Figure 1 shows the calculated trajectories of charged dust projected onto the ecliptic. The trajectories all start at the same point at a distance of 0.9 AU from the Sun and are followed to Mars orbit. All particles start with the same initial velocity assuming they start from circular orbit. The values of charge to mass ratio are different for different trajectories and distributed within plus/minus 20 percent from the equilibrium value. The dashed lines denote the orbits of Earth and Mars. The difference in Lorentz force due to charge variation leads to significant differences in the trajectories. In addition to that, the trajectories with nonzero Q/m all escape away from the ecliptic by quite a large distance. This can be seen in Figure 2, which shows the vertical distance y from ecliptic of the particle vs. distance from the Sun (r) for the calculated trajectories. In any case of non-zero surface charge the dust particles would miss Mars orbit. Note, that in addition to the considered surface charge, also magnetic field varies (*e.g.* Burlaga *et al.* [2]).

4 Summary

While radiation pressure strongly affects the trajectories of dust in a limited size interval, the additional in-

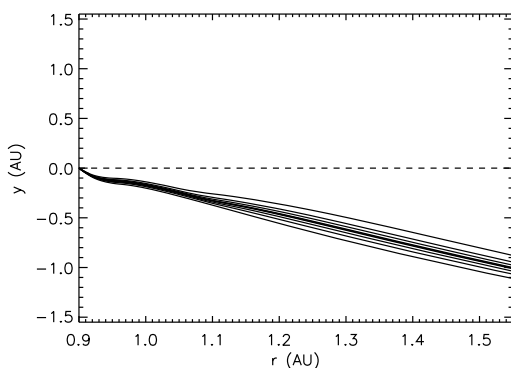


FIGURE 2. The same trajectories as in Figure 1, but shown in the vertical coordinate (y) vs distance from the Sun (r). The trajectories with nonzero Q/m all escape away from the ecliptic by quite a large distance, so that they all miss Mars.

fluence of the Lorentz force on dust in this size interval is not negligible. Electromagnetic forces change the orbital inclination with the result that the dust particles that are released within the ecliptic plane at 0.9 AU for transfer to Mars would not reach the orbit of Mars but would be pushed out from the ecliptic plane. This change of the orbital latitude needs to be taken into account when considering the application of radiation pressure as a tool for acceleration of small dust particles in space. The exact surface charge of the grains as well as the variations of the solar magnetic field are difficult to predict and hence predicting the dust trajectories is a challenge even if the released particles have identical initial surface charge.

The problem can be reduced by choosing a suitable dust material. The variations of the dust surface charge especially occur during solar wind conditions with low plasma density, high temperature, and high bulk velocity, which increase the secondary electron current from the grains. Charge variations are therefore stronger for grains that consist of material with high secondary electron yield, like silicate grains, as opposed to grains that consist of material with low secondary electron yield (for instance carbon, cf. [7]).

Our discussion did not consider the exact shape of particles and the charge estimate assumes spherical grains. The spherical particles carry a smaller charge than irregular particles of equal potential and volume. [1] The irregular shape of particles also leads to a force due to anisotropic emission, but this is only important for meter-sized and larger objects. [3]

References

- [1] S. Auer, S. Kempf, and E. Gruen. Computed electric charges of grains with highly irregular shapes. *Dust in Planetary Systems*, 643:177–180, 2007.
- [2] L. F. Burlaga, L. W. Klein, R. P. Lepping, and K. W. Behannon. Large-scale interplanetary magnetic fields: Voyager 1 and 2 observations between 1 AU and 9.5 AU. *Journal of Geophysical Research*, 89(A12):10659–10, 1984.
- [3] J. A. Burns, P. L. Lamy, and S. Soter. Radiation forces on small particles in the solar system. *Icarus*, 40:1–48, 1979.
- [4] A. Czechowski and I. Mann. Formation and acceleration of nano dust in the inner heliosphere. *The Astrophysical Journal*, 714:89, 2010.
- [5] M. De Juan Ovelar, J. M. Llorens, C. H. Yam, and D. Izzo. Transport of nanoparticles in the interplanetary medium. In *60th International Astronautical Congress, Daejeon, Republic of Korea*, 2009.
- [6] L. Jia and E. L. Thomas. Radiation forces on dielectric and absorbing particles studied via the finite-difference time-domain method. *Journal of the Optical Society of America B*, 26(10):1882–1891, 2009.
- [7] H. Kimura and I. Mann. The electric charging of interstellar dust in the solar system and consequences for its dynamics. *The Astrophysical Journal*, 499:454, 1998.
- [8] T. Mukai. On the charge distribution of interplanetary grains. *Astronomy and Astrophysics*, 99:1–6, 1981.
- [9] M. Wilck and I. Mann. Radiation pressure forces on “typical” interplanetary dust grains. *Planetary and Space Science*, 44(5):493–499, 1996.



Acta Futura 4 (2011) 25-32

DOI: 10.2420/AF04.2011.25

**Acta
Futura**

Towards an on-chip optically integrated array of superconducting detectors for sub-mm and FIR astrophysics

JUAN BUENO,^{*} NURIA LLOMBART [†] AND JOSÉ LUIS COSTA-KRÄMER [‡]

^{*}Centro de Astrobiología (CSIC-INTA), 28850 Torrejón de Ardoz, Madrid, Spain

[†]Departamento de Óptica, Universidad Complutense de Madrid, 28037 Madrid, Spain

[‡]IMM-Instituto de Microelectrónica de Madrid (CNM-CSIC), Isaac Newton 8, PTM, E-28760 Tres Cantos, Madrid, Spain

Abstract.

Cryogenic devices incorporating superconducting thin film structures are currently the most sensitive detectors for many applications. Among these applications the detection of electromagnetic energy (photons) from astronomical sources as well as searches for other types of particles such as dark matter (by detecting gamma rays emitted by dark matter) are very relevant for both space and fundamental research. The latest developments towards a fully integrated on-chip optical system (lenses + detectors) that can be used for the detection of submillimeter-wave (sub-mm) and far infrared (FIR) radiation are reviewed herein. These consist of an integrated system with a large array of Si lenses and Lumped Element Kinetic Inductance Detectors (LEKIDs) fabricated with thin TiN superconducting films.

1 Introduction

Millimeter-wave, submillimeter-wave and far infrared spectroscopy and imaging have become an important and powerful technology for both space and ground-based applications such as atmospheric remote sensing

[19], study of cosmic water profiles [18, 15], comet characterization [20] and investigation of cosmological phenomena with radio telescopes [30]. ESA's Herschel, the largest telescope ever launched to space [29], is presently exploring the sub-mm wavelength domain that cannot be accessed from the ground, thus opening a new window of the electromagnetic spectrum to astronomical research. As a consequence, new populations of very distant dusty galaxies are being detected, new interstellar molecules are being discovered (OH^+ , H_2O^+ , H_2Cl^+) and new exo-protoplanetary disks are being characterized. Europe is already working on SAFARI (SpicA FAR-infrared Instrument) [17], the next instrument to be launched in space by the Japanese Space Agency (JAXA) in the SPICA space mission [1]. SAFARI is an imaging Fourier Transform Spectrometer (FTS) for the SPICA space mission, covering the 30–210 μm waveband with a spectral resolution of $R \sim 10$ to 10000. In the USA, the Astronomy and Astrophysics Decadal Survey [4] has extolled the importance of short wavelength radio surveys of the sky to study dusty material associated with galaxies and stars prioritizing CCAT (Cerro Chajnantor Atacama Telescope), a submillimeter telescope under construction in Chile [5] and BLISS (Background Limited In-

^{*}E-mail address: juan.bueno@cab.inta-csic.es

frared/Submillimeter Spectroscopy) [2], also an instrument for the SPICA space mission.

2 Detection system

The next generation of astronomical instruments requires large field of view cameras with thousands of pixels for allowing simultaneous measurements of a large number of spectroscopic bands over a wide area of the sky. The recently developed Microwave Kinetic Inductance Detectors (MKIDs) [10] have the potential to be the components of such large arrays.

2.1 Principle of operation

The operation of a Microwave Kinetic Inductance Detector is based on the increase in the quasiparticle population and the corresponding increase in the kinetic inductance L_k within the volume of a superconducting film upon absorption of photons or phonons with energies $\hbar f > 2\Delta$ ($d\langle n_{qp} \rangle \approx \hbar f / 2\Delta$) where 2Δ is the binding energy of a superconducting electron pair (Cooper pair). This small inductance change can be measured with the use of high quality factor microwave resonant circuits. The resonant circuit is coupled to a microwave feedline and influences the phase and amplitude of a propagating microwave signal. The absorption of a photon or phonon modifies the inductance of this circuit, changing the resonant frequency f_0 slightly, and thus the measured phase and amplitude of the microwave readout signal.

The primary advantage of this technology is that by using resonant circuits with slightly different resonant frequencies and high quality factors, Frequency Domain Multiplexing (FDM) allows up to a thousand of resonators to be read out through a single coaxial cable and a single HEMT amplifier. The reduction in complexity at the cryogenic level in contrast with other ultra-sensitive low temperature detectors, such as the transition edge sensor (TES) or semiconductor based detectors, is staggering and makes the MKID very relevant to the future development of ground based astronomical cameras, which will depend on larger arrays to improve mapping speeds. The theoretical noise limit of these devices is governed by generation-recombination noise, which scales with temperature and film volume [33]. For a typical coplanar aluminum MKID device operating at 100 mK this noise is estimated to be around 10^{-20} W/Hz $^{1/2}$ [7] which is over an order of magnitude better in sensitivity than other detectors

in this class. Existing MKIDs have shown noise in the mid 10^{-19} W/Hz $^{1/2}$ range [6], which can be lowered further by proper consideration of readout mechanisms, approaching the sensitivity required for background limited observations for applications with low optical background loading (optical power levels below fW and photon noise levels corresponding to NEPs below 10^{-19} W/Hz $^{1/2}$).

2.2 Coupling the radiation to the microwave kinetic inductance detectors

The first approach to fabricate MKID resonators was with the use of distributed half-wave or quarter-wave length co-planar waveguide (CPW) geometries. With this geometry the device acts as a photon or phonon detector once the signal is coupled into the MKID using antennas [9] or quasiparticle traps [28]. In the past years MKIDs have also been used directly as absorbers [11] which is known as Lumped Element Kinetic Inductance Detector (LEKID). Although the different approaches have performed well in the mm-wave, optical and X-ray band, they can be complicated to fabricate and can suffer from efficiency problems which reduces the overall detector performance.

The Lumped Element Kinetic Inductance Detector concept was first introduced in 2007 as a simple solution for coupling incoming signals directly to the sensitive detection elements without the need for additional coupling structures [11]. The LEKID is based on the same principle as the MKID but does not require quasiparticle traps or antennas to operate as an optical detector since the LEKID carefully chosen geometry acts as the radiation absorber.

Coupling the radiation from the telescope to the detectors is a crucial point that directly affects the sensitivity of the instruments. Coupling mechanisms are required for high efficiency and large array integration. At short wavelengths, a good solution is the use of LEKIDs as proposed in [11, 12]. The radiation coupling is achieved by tuning the material conductivity and thickness to the incoming waves impedance. The main disadvantages of such solution with respect to the antenna coupled MKIDs are that i) it suffers from significant cross-coupling between the different array elements and ii) a reduced focal plane receiving area since LEKIDs usually have black spots (areas where the radiation is not absorbed, or absorbed but not changing its resonance frequency). These spots are associated to the area of capacitance of the LEKID and can be of the

order of 25% of the total LEKID area. This translates to an optical efficiency reduction of the same order associated to the smaller receiving area.

We propose the use of lens coupled LEKIDs as shown in Fig. 1 to focus the radiation into the central part of the LEKID (i.e. the inductance area of the resonator). Such configuration has the potential to achieve high sensitive detection, by increasing the focal plane receiving area, and low cross-coupling, by having more isolated resonators, whereas maintaining a low cost fabrication process. The LEKID resonator will be fabricated on a silicon wafer and the lens on the other side of the same wafer by a Si wafer etching process.

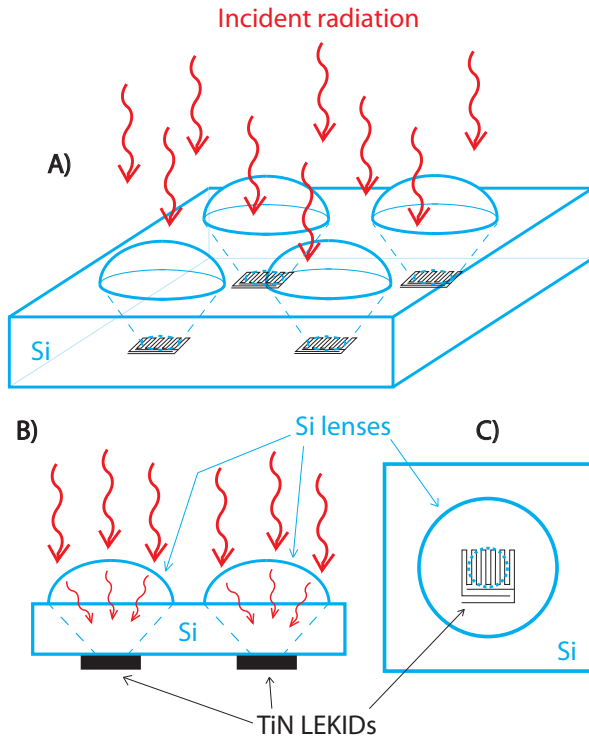


FIGURE 1. Schematic picture of an on-chip optically integrated array of superconducting detectors. A) is a drawing of a silicon wafer with the etched lenses on the top side and the sputtered TiN LEKID detectors on the other. B) and C) are the side and top views of the device respectively.

3 Lens coupled lumped element kinetic inductance detector

The LEKID radiation absorbing mechanism relies on matching the incoming wave impedance using the con-

ductivity and thickness values of the material. The absorption mechanism is similar to the one used by a micromesh bolometer [34]. It consists of a distributed metallic grid over a back short placed at a $\lambda/4$, being λ the wavelength of the medium, with an impedance chosen to optimize sub-mm absorption. The grid is considered to be immersed in the silicon. For small grid periods, assuming just the main Floquet mode in a periodic analysis, i.e. $d \ll \lambda$, an effective sheet impedance of the grid can be calculated as $R = \frac{d}{w} \frac{\rho}{t}$, where d is the grid period, w is the width of the leg, t is the thickness of the metallic layer, and ρ is the electrical resistivity of the metal (see Fig. 2 inset for a geometry clarification). The absorption efficiency is maximized when a back short at $\lambda/4$ is used. In such case, the sheet impedance should match the characteristic impedance of free space $R = 120\pi/n$, where n is the index of refraction of silicon $n = 3.45$. If the period of the array approaches $\lambda/2$, a more detailed analysis including higher order Floquet modes is needed as explained in [26]. Figure 2 shows the absorption efficiency of THz plane wave coming from broadside for a grid of $d = 60 \mu m$, $w = 12 \mu m$, $hb = 44 \mu m$, $t = 1 \mu m$ and $\sigma = 4.5 \times 10^4 S/m$ at normal incidence. The grid is considered to be infinite and it is simulated as a periodic structure. The efficiency is high due to the use of a back short. For a situation where the LEKID is placed in the interface between the vacuum and the silicon and no back short is used the efficiency drops to 75% provided that $R = 120\pi/(n + 1)$. However the lens efficiency analysis described in the following is analogous.

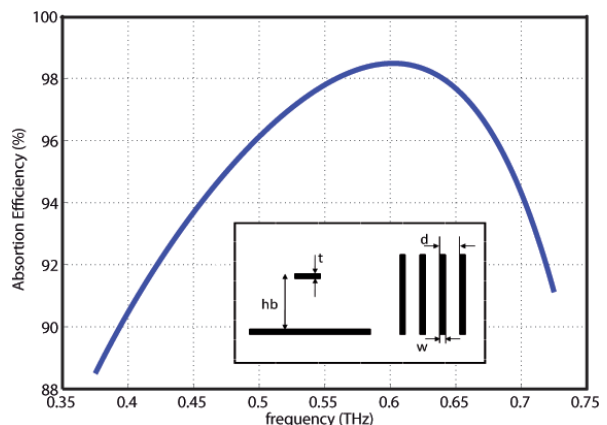


FIGURE 2. Absorption efficiency for normal incidence of a wire grid of a period $d = 60 \mu m$, a wire width of $w = 12 \mu m$, a wire thickness of $t = 1 \mu m$ made of a metal with $\sigma = 4.5 \times 10^4 S/m$ above a ground plane placed at $hb = 44 \mu m$.

If such grid is placed at the focal plane of an extended hemispherical lens, the absorption efficiency will be the integration of the grid response to a range of plane waves defined by the lens f-number [26], not just that of a single plane wave arriving from a certain angle. However, if the f-number values used are large (standard elliptical silicon lenses have an f number value of the order of 0.6), as proposed here, the corresponding angular range will be small and therefore the absorption will resemble the one of a single plane wave coming from broadside. The reason for this assumption is that the field at the focal plane of a focusing lens has the shape of an airy pattern. This pattern can be expressed mathematically as the anti fourier transform of its plane wave spectrum, which corresponds to the integration of the plane waves coming from 0 to θ where $\theta = \arcsin(\frac{1}{2f})$ given by the lens f-number. Figure 3 shows the electric field simulated with CST [3], where we have considered a lens with an aperture of 2.4 mm and an f-number of 1.04. The absorption efficiency estimated in the simulations was of the same order as that calculated for the single plane wave shown in Fig. 2.

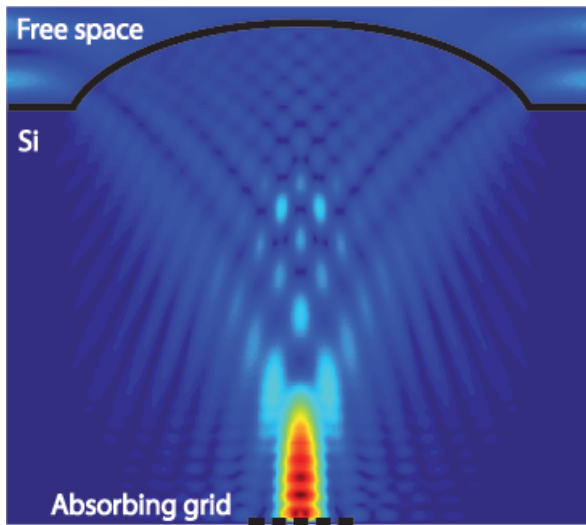


FIGURE 3. Electric field distribution inside a silicon microlens with an aperture of 2.4 mm and an f-number of 1.04. An absorbing grid with the dimensions shown in Fig. 2 is placed at the focal plane of the lens.

4 Lens Fabrication

For large arrays, consisting of thousands or more detectors, techniques to fabricate the integrated lens ar-

rays are required. The fabrication of such arrays is still a challenge in this frequency range. Advanced techniques are needed to avoid the manual assembly of the array as proposed in the analysis of the first sub-mm instruments [8]. It is possible to use lithographic techniques or laser micromachining to fabricate arrays of lenses in the same wafer. The advantage of the lithographic fabrication technique is that it will allow the fabrication of the whole array in parallel. The success of this technique depends also on the dimension of the lens and in particular on the actual lens thickness. The use of large f-numbers for the lens in order to reduce its thickness will be mandatory [27]. In any case, the LEKID absorbing dimension can be easily matched to the corresponding f-number.

Reflow has been demonstrated to be a successful technique for the fabrication of glass microlenses [31, 25, 22]. This technique has been also used to fabricate silicon microlenses transferring the shape of the glass microlens into a silicon wafer by means of Reactive Ion Etching (RIE) [21, 14]. These silicon arrays of microlenses have been used for infrared (IR) radiation but due to the small size of the lenses this technology has not been proven for sub-mm and FIR radiation. The f-number of the microlenses depends on the ratio between the height and the diameter of the lens. With the reflow technique the height of the lens is limited by the thickness at which the photoresist is span (maximum 350 μm), and therefore large diameters imply very large f-numbers and consequently very thick wafers. Thus a different technique, the so-called drop technique, is also being studied in parallel. The idea for the drop technique is to transfer the shape of a cured solid photoresist drop, which gets the shape of a spherical cap due to surface tension, into the silicon wafer by a RIE process. There are two steps in this process: the first one is the preparation of the photoresist drop using a micropipette and curing the resist, and the second one is the transfer of the shape of the drop into the silicon by RIE. The drop technique has the advantage that the height of the lens is set by the surface tension, which is proportional to the density of the photoresist. Using a more dense photoresist allows a higher lens for the same lens diameter. However it is more difficult to be extended for an array, whereas the reflow technique should be straightforward. Therefore, we are looking to both techniques in parallel: the drop technique would most likely be adequate for the fabrication of small arrays and the reflow technique for large number of lenses. The quality and homogeneity of these lens arrays will not be as good as

the ones that it is possible to obtain with a laser ablation technique. However, these methods provide with a faster and inexpensive way of fabricating lens arrays for submillimeter applications. Although the work on the lens arrays is still preliminary, we believe that once the lithographic and RIE processes are fully developed and optimized, reproducibility and homogeneity in arrays of hundreds of lenses should be achievable.

4.1 Preparation of the photoresist drop

Positive photoresist Microposit S1813 from Shipley (UK) was used for these experiments. Different densities of the same photoresist were obtained by evaporating part of the solvent contained in the resist in an oven at 90 °C. A series of drops were made with the different resists on silicon wafers using a micropipette. By carefully choosing the volume with the micropipette, it is possible to control the diameter of the lens. The height of the lens is set by the surface tension of the photoresist, which depends on its density [32, 13]. Therefore, using a thinner or thicker resist allows one to control the height of the lens. After depositing the drops on the wafer, they were precured in an oven at 90 °C for 10 minutes and then cured for 90 hours in another oven at 120 °C. It is very important for the final lens quality that the drop is completely cured before starting the etching process.

4.2 Reactive ion etching of the photoresist drop

The drops were etched in a Reactive Ion Etching (RIE) chamber using a mixture of gases of SF₆ and O₂ at 50 and 10 sccm respectively, at a pressure of 90 mtorr. Etching series at different plasma powers were done, although it turned out that 250 W was the power at which the lenses had the optimum quality. We defined the transfer ratio between the photoresist and the silicon as the ratio between the height of the resist lens and the height of the silicon lens. This transfer ratio varied slightly depending on the photoresist used but it was approximately ~ 1.7.

4.3 Surface characterization

Scanning Electron Microscopy (SEM) techniques were used to characterize the lens surface. The SEM characterization of a lens can be found in Fig. 4.B, where it is possible to distinguish several small pores at the lens surface. The pores diameter is approximately 2 μm. At this point, the reason for the pores formation remains still

unclear although it seems clear that they are present already at the resist. A possible explanation for the formation of these pores is that they are remaining microbubbles of liquid resist inside the drop that evaporate very quickly once they are in contact with the plasma during the etching process, leaving their shape into the resist and forming the pores.

Atomic Force Microscopy (AFM) analysis were carried out in order to study the topography of the lens surface (see Fig. 4.C and Fig. 4.D). The AFM images were taken in contact mode in air, with a Scientec scanner with a maximum range of 100 μm × 100 μm. (n)Doped silicon tips with a nominal force constant ranging from 0.5 to 9.5 N/m were used. The deepest pore found had a depth of approximately 0.4 μm and a diameter of around 2 μm. The root-mean-square (rms) roughness was estimated with the WSxM software [23] obtaining values of 0.06 ± 0.01 μm, which is very good for sub-mm and FIR optical instruments.

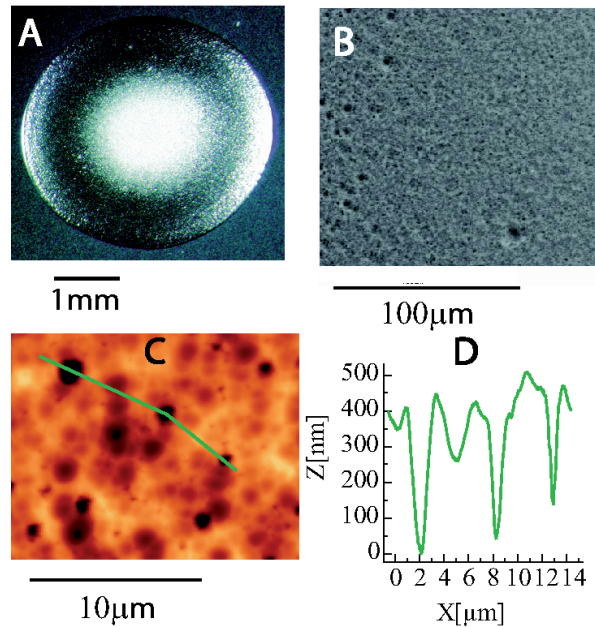


FIGURE 4. *A* is an optical photograph of a fully etched silicon lens. The lens diameter is about 3.5 mm and the height is about 110 μm, with a surface roughness of approximately 2 μm. *B* is an image taken with the SEM where the roughness of the lens surface can be observed. *C* is a 2-D AFM image of the pore observed with the SEM. *D* shows a 1-D AFM scan along the green line drawn in *C*.

5 Optimization of superconducting materials

The sensitivity of a LEKID detector depends strongly on the properties of the superconducting material. The normal-state resistivity of the material has to be high so the absorber impedance can be matched with the free-space impedance easily. The superconducting material quasiparticle lifetime has to be also high since the chance of detecting them relies on the time that the quasiparticles linger in the detector.

5.1 The role of titanium nitride

Titanium nitride (TiN) is an ideal material choice for a detector because of its critical superconducting transition temperature, which can be tuned from 0 to 5 K, and its large normal-state resistivity which has been reported to be $100 \mu\Omega\text{cm}$ [24]. The TiN normal-state resistivity is similar to polycrystalline TiN films reported in the literature but considerably higher than for single-crystal films. The high resistivity (relative to Al, Ta, or Nb) is very convenient for highly efficient photon absorption in lumped-element resonator structures [12]. As a consequence of the Mattis-Bardeen relationship $L_s \approx \hbar R_s / \pi \Delta$ between the normal-state surface resistance R_s and the superconducting surface inductance L_s , the large resistivity also guarantees a large kinetic inductance fraction $\alpha_{sc} \approx 1$. Another important factor is the quasiparticle lifetime. The maximum quasiparticle lifetime found in Leduc *et al.* experiments is $200 \mu\text{s}$ for $T_c=0.8 \text{ K}$ [24]. The use of TiN carries a factor of 10 improvement in sensitivity with respect to Aluminium LEKIDs. Other important characteristics of TiN are that it is a mechanically robust material and that sputtered TiN films show very low loss. Furthermore, the ability to reach high Q_r with TiN resonators should enable very dense LEKID frequency multiplexing.

5.2 Titanium nitride film growth

The TiN thin films were deposited using a home made multicathode triode sputtering system reaching a base pressure of $2 \times 10^{-8} \text{ mbar}$. The substrate holder is transferred from the load-lock to the sputtering chamber by a linear magnetic manipulator. A halogen lamp type of heater is used in the load-lock chamber to degas substrates at $\approx 200^\circ\text{C}$ for 5 min prior to their introduction in the main chamber for TiN deposition. There are two leakage valves in the sputtering chamber to intro-

duce separately Ar and N₂ into the vacuum chamber. Both gases were 99.995% purity. The Ti target has a diameter of 50 mm and the distance from the target to the substrate distance is 80 mm. Typical plasma parameters for TiN film growth were: a) total gas pressure of $8 \times 10^{-3} \text{ mbar}$, b) heating filament current of typically 13 Amps, c) plasma current of about 2 Amps and bias voltage of 30 V, d) potential applied to the sputtering target was about 1.25 – 2 kV at powers between 20 W and 40 W. The TiN films were deposited at different Ar/Nitrogen partial pressures, from pure Nitrogen (0% Ar) to 100% Ar, in order to tune their superconducting critical temperature (see Fig. 5), while the substrate was kept at room temperature during film growth.

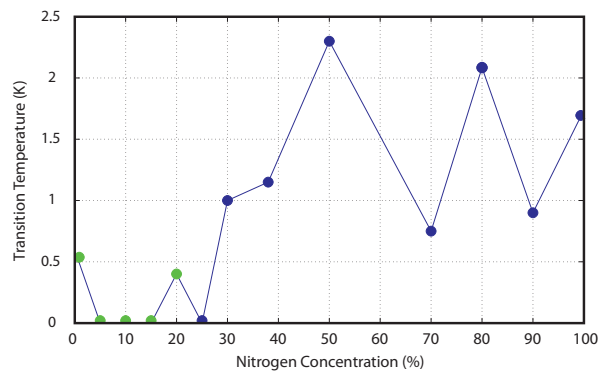


FIGURE 5. (color online) Transition temperatures of TiN films measured in a four probe configuration. Green points show the TiN films sputtered at 20 W and blue point show the TiN films sputtered at 40 W. Solid lines are a guide to the eye.

6 Discussion

LEKIDs have shown an important impact in millimeter, submillimeter and far infrared astronomical instrumentation in the past years [16] and represent a critical technology for future detector arrays, due to their simplicity compared to other types of detectors and the large number of pixels that can be multiplexed. In this article the use of microfabricated silicon lenses to reduce the cross-coupling between different pixels and improve the overall efficiency has been presented. This method has been validated with electromagnetic simulations which show radiation conversion efficiencies up to 90%. Attempts of fabricating silicon micromachined lenses have been successful, obtaining lenses of a few millimeters in diameter and hundreds of microns in height with low

rugosity (below 3 μm). Once lithographic and RIE processes are fully developed and optimized, reproducibility and homogeneity in arrays of hundreds of lenses should be achievable. The first superconducting TiN films have been grown in a UHV chamber by sputtering Ti at different Nitrogen/Argon partial pressure ratios to tune the superconducting transition temperature. The next steps in the development of this detection device concept are the fabrication of absorbing structures with the TiN, fabrication and testing of an on-chip lens and LEKID system, and the implementation and characterization of a full array of lens coupled LEKIDs.

7 Acknowledgements

The authors gratefully acknowledge TiN film low temperature resistive measurements by A. Camón from the ICMA (CSIC) and by S. Doyle, J. Gould and D. Mozorov from Cardiff University. They also acknowledge IMM triode sputtering chamber setup work performed by I. Fernández and F. Briones, J. Martínez from IMM for help with the Si RIE experiments, E. López-Camacho from ICMM for SEM and AFM characterization, M. Arroyo-Hernández for X-ray measurements of TiN films, A. G. Taboada from CAB for his work with the microlenses arrays, and J. Martín-Pintado from CAB and C. Dunscombe and P. D. Mauskopf from Cardiff University for helpful discussions. Juan Bueno acknowledges support through grants AYA2008-06166-C03-02 and AYA2010-21697-C05-01. Nuria Llombart acknowledges support through grant AYA2010-10054-E and the program “Ramón y Cajal” RYC-2009-04924. José L. Costa-Krämer acknowledges support from MAT2008-06330.

References

- [1] http://ir.isas.jaxa.jp/SPICA/SPICA_Home/index_English.html.
- [2] <http://sub-mm.caltech.edu/BLISS/>.
- [3] <http://www.cst.com/>.
- [4] http://www.nap.edu/catalog.php?record_id=12951.
- [5] <http://www.sub-mm.org/>.
- [6] J. J. A. Baselmans, S. J. C. Yates, R. Barends, Y. J. Y. Lankwarden, J. R. Gao, H. Hoevers, and T. M. Klapwijk. Noise and sensitivity of aluminum kinetic inductance detectors for sub-mm astronomy. *J. Low Temp. Phys.*, 151(1-2):524–529, 2008.
- [7] J. J. A. Baselmans, S. J. C. Yates, P. de Korte, H. Hoevers, R. Barends, J. N. Hovenier, J. R. Gao, and T. M. Klapwijk. Development of high-q superconducting resonators for use as kinetic inductance detectors. *Advances in Space Research*, 40(5):708–713, 2007.
- [8] T. H. Buttgenbach. An improved solution for integrated array optics in quasi-optical mm and sub-mm receivers: the hybrid antenna. *IEEE Trans. MTT*, 41:1750–1760, 1993.
- [9] P. K. Day, H. G. Leduc, A. Goldina, T. Vayonakis, B. A. Mazin, S. Kumar, J. Gao, and J. Zmudzinas. Antenna-coupled microwave kinetic inductance detectors. *Nuclear Instruments and Methods in Physics Research*, 559(2):561–563, 2005.
- [10] P. K. Day, H. G. LeDuc, B. A. Mazin, A. Vayonakis, and J. Zmudzinas. A broadband superconducting detector suitable for use in large arrays. *Nature*, 293:817–821, 2003.
- [11] S. Doyle, J. Naylor, P. D. Mauskopf, A. Porch, and C. Dunscombe. A lumped element kinetic inductance device for detection of THz radiation. *32nd International Conference on Infrared and Millimeter Waves IRMMW-THz*, pages 450–451, 2007.
- [12] S. Doyle, J. Naylor, P. D. Mauskopf, A. Porch, and C. Dunscombe. A lumped element kinetic inductance device for detection of THz radiation. *J. Low Temp. Phys.*, 151(1-2):530–536, 2008.
- [13] J. C. Earnshaw, E. G. Johnson, B. J. Carroll, and P. J. Doyle. The drop volume method for interfacial tension determination: an error analysis. *Journal of Colloid and Interface Science*, 177(1):150–155, 1996.
- [14] L. Erdmann and D. Efferenn. Technique for monolithic fabrication of silicon microlenses with selectable rim angles. *Opt. Eng.*, 36(4):1094–1098, 1997.

- [15] P. Eriksson, M. Ekström, B. Rydberg, and D. P. Murtagh. First odin sub-mm retrievals in the tropical upper troposphere: ice cloud properties. *Atmos. Chem. Phys.*, 7(2):471–483, 2007.
- [16] A. M. et al. Nika: A millimeter-wave kinetic inductance camera. *Astronomy & Astrophysics*, 521:A29, 2010.
- [17] B. S. et al. The space infrared telescope for cosmology and astrophysics: Spica a joint mission between JAXA and ESA. *Experimental Astronomy*, 23(1):193–219, 2009.
- [18] G. J. M. et al. The submillimeter wave astronomy satellite: Science objectives and instrument description. *The Astrophysical Journal*, 539(2):L77–L85, 2000.
- [19] J. W. W. et al. The earth observing system microwave limb sounder (EOS MLS) on the aura satellite. *IEEE Transactions on Geoscience and Remote Sensing*, 44(5):1075–1092, 2006.
- [20] S. G. et al. Miro: Microwave instrument for rosetta orbiter. *Space Science Reviews*, 128(1–4):561–597, 2007.
- [21] N. T. Gordon, C. L. Jones, and D. J. Purdy. Application of microlenses to infrared detector arrays. *Infrared Phys.*, 31(6):599–604, 1991.
- [22] M. He, X.-C. Yuan, N. Q. Ngo, J. Bu, and V. Kudryashov. Simple reflow technique for fabrication of a microlens array in solgel glass. *Optics Letters*, 28(9):731–733, 2003.
- [23] I. Horcas, R. Fernández, J. M. Gómez-Rodríguez, J. Colchero, J. Gómez-Herrero, and A. M. Baro. WSxM: A software for scanning probe microscopy and a tool for nanotechnology. *Rev. Sci. Instrum.*, 78(1):013705, 2007.
- [24] H. G. Leduc, B. Bumble, P. K. Day, B. H. Eom, J. Gao, S. Golwala, B. A. Mazin, S. McHugh, A. Merrill, D. C. Moore, O. Noroozian, A. D. Turner, and J. Zmuidzinas. Titanium nitride films for ultrasensitive microresonator detectors. *Appl. Phys. Lett.*, 97:102509, 2010.
- [25] S.-K. Lee, M.-G. Kim, K.-W. Jo, S.-M. Shin, and J.-H. Lee. A glass reflowed microlens array on a si substrate with rectangular through-holes. *J. Opt. A: Pure Appl. Opt.*, 10(4):044003, 2008.
- [26] N. Llombart, C. M. Bradford, A. Neto, and G. Chattopadhyay. Impedance matching of a micromesh bolometer placed in a silicon parallel plate waveguide spectrometer. *IEEE Antennas and Propagation Society International Symposium, 2008. AP-S 2008*, 2008.
- [27] N. Llombart, G. Chattopadhyay, C. Lee, J. Gill, A. Skalare, I. Mehdi, and P. H. Siegel. Narrow angle lens antenna for thz applications. *Antennas and Propagation Society International Symposium, 2009. APSURSI '09. IEEE*, pages 1–4, 2009.
- [28] B. A. Mazin, B. Bumble, P. K. Day, M. E. Eckart, S. Golwala, J. Zmuidzinas, and F. A. Harrison. Position sensitive x-ray spectrophotometer using microwave kinetic inductance detectors. *Appl. Phys. Lett.*, 89:222507, 2006.
- [29] G. e. a. Pilbratt. Herschel space observatory. an ESA facility for far-infrared and submillimetre astronomy. *Astronomy and Astrophysics*, 518:L1, 2010.
- [30] G. L. Pilbratt. The herschel mission, scientific objectives, and this meeting. *Proc. Eur. Space Agency Symp.*, SP-460:13–20, 2000.
- [31] Z. D. Popovic, R. A. Sprague, and G. A. N. Connell. Technique for monolithic fabrication of microlens arrays. *Applied Optics*, 27(7):1281–1284, 1988.
- [32] Y. Rotenberg, L. Boruvka, and A. W. Neumann. Determination of surface tension and contact angle from the shapes of axisymmetric fluid interfaces. *Journal of Colloid and Interface Science*, 93(1):169–183, 1983.
- [33] A. V. Sergeev and M. Y. Reizer. Photoresponse mechanisms of thin superconducting films and superconducting detectors. *Int. J. Mod. Phys. B*, 10(6):635–667, 1996.
- [34] A. D. Turner, J. J. Bock, J. W. Beeman, J. Glenn, P. C. Hargrave, V. V. Hristov, H. T. Nguyen, F. Rahman, S. Sethuraman, and A. L. Woodcraft. Silicon nitride micromesh bolometer array for submillimeter astrophysics. *Applied Optics*, 40(80), 2001.



Acta Futura 4 (2011) 33-40

DOI: 10.2420/AF04.2011.33

**Acta
Futura**

A relativistic navigation system for space

ANGELO TARTAGLIA^{*}, MATTEO LUCA RUGGIERO[†], EMILIANO CAPOLOGNO[‡]

*Dipartimento di Fisica, Politecnico di Torino, corso Duca degli Abruzzi 24, 10129 Torino, Italy,
and INFN, via Pietro Giuria 1, 10126 Torino, Italy*

Abstract. We present here a method for relativistic positioning in spacetime based on the reception of pulses from sources of electromagnetic signals whose worldline is known. The method is based on the use of a four-dimensional grid covering the whole spacetime and made of the null hypersurfaces representing the propagating pulses. In our first approach to the problem of positioning we consider radio-pulsars at infinity as primary sources of the required signals. The reason is that, besides being very good clocks, pulsars can be considered as being fixed stars for reasonably long times. The positioning is obtained linearizing the worldline of the observer for times of the order of a few periods of the signals. We present an exercise where the use of our method applied to the signals from four real pulsars permits the reconstruction of the motion of the Earth with respect to the fixed stars during three days. The uncertainties and the constraints of the method are discussed and the possibility of using moving artificial sources carried around by celestial bodies or spacecrafts in the Solar System is also discussed.

1 Introduction

In ancient times people learnt to travel by sea, far from the coast, looking at the sky. Though they measured time on the basis of the day and night alternation and not much more, Polynesian settlers, using the stars as a guide, were able to sail across the Pacific ocean over thousands of kilometers without getting lost. In the West, once the measurement of time reached modern accuracy and precision with the first marine chronometer, the celestial navigation was the base of the spread of European colonization over the world. Today the equivalent of the old navigation (and of the present, though by other guidance systems) is represented by the exploration of the Solar System and, possibly, even beyond. Until now however the guidance of the spacecraft is performed from Earth; stars are used at most for trim definition purposes on board.

In fact the idea of using stars for navigation in space seems and sounds appealing, but now, our better knowledge of space and time, which General Relativity binds together, must be taken into account. In particular in order to achieve the precision and accuracy needed in space we cannot simply consider the configuration of "fixed" stars and the times at the origin of our travel and at the local position. We need to compare clocks far away in the sky (or at least following known spacetime trajectories or worldlines) with a clock we carry

^{*}E-mail address: angelo.tartaglia@polito.it

[†]E-mail address: matteo.ruggiero@polito.it

[‡]E-mail address: emiliano.capolongo@polito.it

with us. The idea we are reviewing and presenting in the present paper outlines a fully relativistic navigation system based on the local measurement of the arrival times of electromagnetic signals from sets of at least four pulsating sources, located at known positions in the sky. The first implementation of the idea considers pulsars as sources, however, as we shall see, the same approach can be adopted when the origin of the pulses is an artificial one.

2 Relativistic positioning

Any object in spacetime, for instance a pointlike observer, is represented by a line, actually its worldline, in the fourdimensional continuum. Electromagnetic signals that reach the observer at a given position and time, travel on his past light cone. The situation is schematized in fig. 1

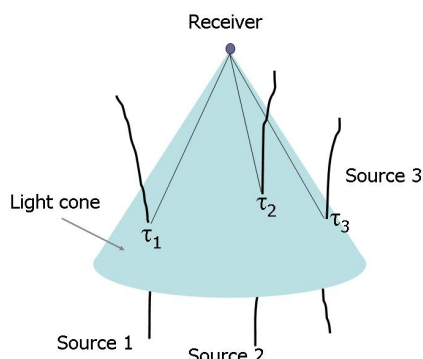


FIGURE 1. View of a pointlike observer with its past light cone; time flows from bottom to top. The black almost vertical lines correspond to the world lines of three light emitters slowly moving around. The straight lines on the surface of the cone are the world-lines of the electromagnetic signals emitted by each source. The numbers τ_1 , τ_2 and τ_3 are the proper times at the emission event.

The figure necessarily represents a three-dimensional spacetime; actually the dimensions should be four, but the geometrical configuration is essentially the same. Imagine you have at least four broadcasting devices, each one equipped with a clock; their electromagnetic signals can convey the information of the proper time of each emitter at the moment of the emission. The user is reached at any moment by a set of four signals; the information carried by each signal concerns the identi-

fication code of the source and the proper emission time of that signal. The relevant fact is that the set of the four emission times depends on the position of the observer in spacetime. The correspondence between positions and quartets of proper times is one to one, provided the four worldlines of the emitters are linearly independent from one another and as far as we do not consider lensing effects, which are important in strong gravitational fields. Under these conditions we may think to use the four numbers (the four emission times) as good coordinates localizing the receiver both in space and in time (this is the reason why the emitters must be at least four). The basis for this peculiar coordinate set is given by the spacetime trajectories of the four emitters. The four proper times are the *emission coordinates* of the user. This approach has been considered by various authors [2, 9, 11, 1, 6] and has especially been studied by B. Coll and collaborators [3, 5, 4].

Our approach is slightly different, but in the end it produces an equally reliable positioning. If we imagine to have a finite source of electromagnetic waves located at space infinity, the wave fronts of the signal will everywhere be planes. Suppose the source emits periodic pulses: geometrically the signal will be a set of non-intersecting planes traveling at the speed of light. If we have four of such pulsed sources, their pulses will fill space with a sort of egg-crate lattice. Each signal from each source may be labeled with a simple ordinal number, so that each cell in the lattice is identified by the labels on one of the corners. The orientation of one family of planes (pulses from one of the sources) is specified when a unit vector perpendicular to one of the planes is given. All this is expressed in three dimensions, but spacetime is four-dimensional, so that the same considerations as above can be made identifying each traveling pulse with a (three-dimensional) hyperplane; its orientation will be given by a four-vector orthogonal to the (family of) hyperplanes. Our four-vector can carry all the relevant information if it is written like this:

$$\chi \doteq \frac{1}{cT} (1, \vec{n}) \quad (1)$$

Here \vec{n} is a purely spacelike unit three-vector. In an arbitrary Cartesian coordinates system in space its components would be the direction cosines of the vector with respect to the coordinated axes. T is the periodicity of the pulses given in a reference frame where the source is at rest (proper period of the pulses). The factor we put in front of the expression of χ in (1) produces the same dimensions as for ordinary three-dimensional

wave-vectors. Since we are speaking of electromagnetic pulses, the χ vector is null or self-orthogonal:

$$\chi \cdot \chi = \frac{1}{c^2 T^2} (1 - 1) = 0 \quad (2)$$

If we consider the covariant version of χ , which is, technically speaking, a 1-form, we know that it has a Hodge conjugate 3-form:

$$\omega = * \chi \quad (3)$$

The 3-form ω is, by construction, perpendicular to the four-vector χ : $\chi \cdot \omega = 0$. Furthermore, being χ a null vector, ω too is null: $\omega \cdot \omega = 0$. In practice, since χ identifies a direction in space-time, ω , as we wrote above, corresponds to a family of three-dimensional hyperplanes perpendicular to χ . When we split the four-dimensional description into space and time (3+1 splitting), the projection of the above picture in space gives the familiar view of a set of ordinary bi-dimensional planes (wave fronts) propagating along the direction given by the space components of χ at the speed of light.

What matters for us is that four families of independent hyperplanes of this sort cover the whole space-time with a four-dimensional foam of (hyper)cells, each one uniquely labeled by a set of four integers (the ordinal numbers of the hyperplanes, i.e. of individual pulses, meeting at one of the vertices). This configuration permits to position any event in spacetime modulo the edges of a cell. If we identify the sources by the indices a, b, c, d the lengths of the edges will be cT_a, cT_b, cT_c, cT_d ; each edge is null in the sense of (2).

Now, if we have an observer moving across space-time, his worldline successively intersects the cells of the "foam" we mentioned above. The situation is sketched in fig. 2.

The intersection of the worldline with one of the hyperplanes identifies the reception event of the corresponding pulse. If the receiver is equipped with a clock he can both count the subsequent arrivals of the pulses and measure the proper time intervals between the arrivals, represented in fig. 2 by the length of the worldline between two intersections.

If we consider, for instance, an arrival event from source a , we may label it with the integer n_a . Of course from the viewpoint of the signals from b the n_a event will have a label somewhere in between n_b and $n_b + 1$; the same will in general be the case for sources c and d . In practice we may think to use the four numbers

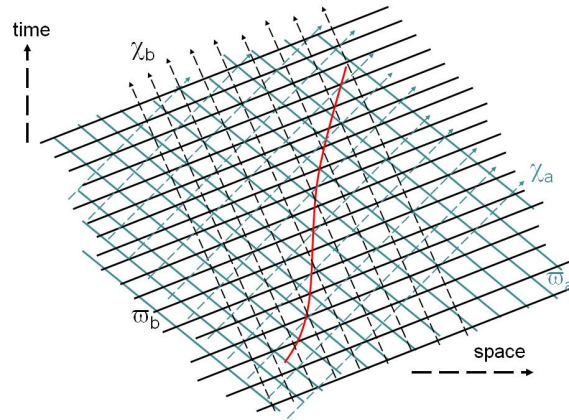


FIGURE 2. Bidimensional view of the positioning pattern described in the text. ω_a and ω_b identify two families of hyperplanes; each hyperplane corresponds to a single pulse from a source and may be labeled by an ordinal number. The dashed lines correspond to the flow lines of the χ null four-vectors. The continuous wiggling line is the worldline of an user traveling across spacetime. The intersection of the worldline with one of the hyperplanes identifies the reception event of the corresponding pulse.

$\{n_a; n_b + x_b; n_c + x_c; n_d + x_d\}$ as coordinates to localize the reception event of the n_a -th pulse from source a . The x 's we have introduced are, in general, $0 \leq x < 1$.

2.1 Linearization

If we want the above defined coordinates to be useful we must find a practical way to evaluate the fractional x 's. This is indeed easy if spacetime is flat and the worldline of the observer is straight. The situation then is shown in fig. 3. If the observer has got a clock he is able to measure the time intervals between the arrivals of the pulses, i.e. the lengths between the light blue blobs marking the arrivals of the signals in fig. 3.

Under the geometrical assumptions we have made it is trivial to see that, given a sequence of eight arrivals, simple linear relations between the time intervals and the x 's hold. Solving the corresponding system of linear equations leads to the complete definition of the positions in spacetime of the first four reception events. With a moving sequence of events, it is then possible to fully reconstruct the whole worldline of the receiver.

In order to turn our n 's and x 's into practical coordinates we must also know the proper emission periods of the sources (the T 's) and their positions in the sky, in other words, their worldlines. In practice these are the

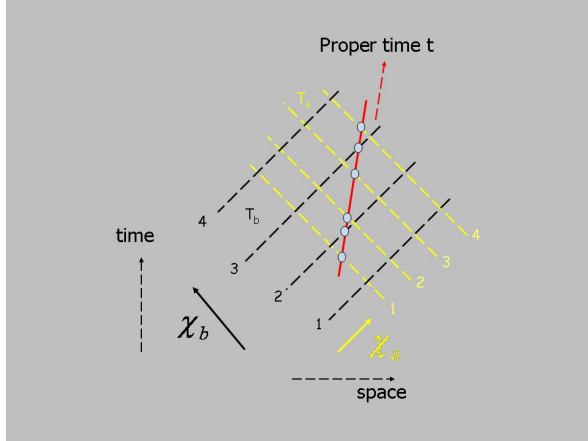


FIGURE 3. Bidimensional representation of the reception of a number of successive pulses arriving from sources *a* and *b* according to the scheme of fig. 2; the small ovals identify the arrival events. When the worldline of the user is straight, or may be thought of as approximately straight, the knowledge of the time span between the arrivals of the pulses is sufficient to uniquely localize the reception events, and then the position of the user.

direction cosines of the propagation from each source (for details see [14, 15]).

3 Constraints and uncertainties

In order to have an extremely simple algorithm we considered a flat spacetime and a straight worldline of the observer. Are these conditions credible? and to what extent?

3.1 The observer's worldline

In a flat spacetime a straight worldline corresponds to an inertial, and therefore uniform, motion. This condition is not appropriate to describe the journey of a spacecraft in space both because of the presence of the gravitational field and of the maneuvers made using an engine; this is increasingly relevant when one considers the motion on the surface of a celestial body, including the Earth. In general the motion will be accelerated as in the case shown in fig. 2. Neglecting for one moment the gravitational field, one can ask; "how can we treat the curvature of the worldline due to the acceleration"?

Developing the worldline function in powers of time and looking at the first non linear term in the *i*-th space component of the motion we have of course:

$$s_i = v_i t + \frac{1}{2} a_i t^2 \quad (4)$$

The relative importance of the non linear term with respect to the linear one is:

$$\epsilon = \frac{a_i t}{2v_i} \quad (5)$$

Now if we decide what is the acceptable tolerance for our problem we obtain the maximum time within which the linear approximation for the worldline (i.e. the uniform motion hypothesis) is viable:

$$t \leq \delta t = 2\epsilon \frac{v_i}{a_i} \quad (6)$$

Within the Solar System the speed of freely falling objects is controlled by Kepler's laws, so that it does not exceed $\sim 10^5$ m/s (the escape velocity from the surface of the Sun is $\sim 6 \times 10^5$ m/s); for our purposes it is not the case to consider "visitors" not belonging to the Solar System. On the other hand, for manned vehicles there are limitations of the maximal acceleration that should not exceed $30 - 40$ m/s² in order to prevent unacceptable physical damage (the acceleration at launch of the space shuttle is limited to approximately 30 m/s² [8]). It is less simple to define upper limits to the tolerable acceleration for unmanned spacecraft, since that limit would depend on the fragility of the payload and of the onboard equipment. It is, however, true that usually the preferred strategy for space missions is to tend to favor weak long-lasting thrusts rather than short and violent pushes, the latter being reserved at most for the take off from celestial bodies. As a reference, we take the value of 100 m/s² for the highest acceleration. Using these figures we see that an accuracy of 1 part in 10^5 implies that the linearity hypothesis is not tenable for more than approximately $\delta t = 10^{-2}$ s. If we think to our sources as being millisecond pulsars, the above δt includes a number of cycles which is roughly 10: this is enough for a sequence of 8 events such that the actual worldline of the receiver is piecewise reconstructed as a chain of locally straight portions. Of course, if we consider pulsar sources with an emission period in the order of μ s's or less¹, we may use a much higher number of paces within a given interval. In this way, keeping the prescribed accuracy fixed, we could allow for much bigger accelerations.

¹In this case they could not be pulsars, since neutron stars cannot rotate that fast, because of their size.

The final accuracy of the positioning depends both on the quality and emission frequency of the sources and on the accuracy of the onboard clock used to measure the delay from one arrival event to the other.

3.2 The gravitational field

Until now we have neglected the influence of gravitational fields which are of course present throughout the Solar System. This means that the background spacetime is curved rather than flat; can we account for this? A first remark is that the curvature of spacetime at the emission point and along most of the trajectory of the signal, out of the Solar System, is irrelevant for our method, provided it does not change in time, or at least it changes only over times much longer than the ones implied in our positioning process. The reason is that the curvature in the environment of the emitting neutron star and along the electromagnetic ray determines the global time of flight of a pulse in an (almost) time-independent way, so that it does not affect the intervals between the arrival times of successive signals. What remains to be considered is the effect of the curvature in the region where the receiver is located; since the receiver is moving, also the local curvature it feels changes with time. However we remark that the gravitational acceleration within the Solar System (excepting the surface of the Sun and the giant planets) is of the order of 10 m/s^2 and usually much less than that. In these conditions a simple Newtonian approach is acceptable; under this condition the gravitational field can be treated as any other acceleration field in a flat background. In practice for times short enough that the worldline can be considered to be straight we are on the tangent space and no gravitational field is visible, but for longer times gravity appears in the bending of the reconstructed space-time trajectory. Again we have a time tolerance within which our linear algorithm works; if we wish instead to use our method in order to investigate the structure of the gravitational field at the receiver's position, we simply need to collect data for a long enough time.

4 An exercise

In order to make a preliminary evaluation of the feasibility of a positioning system like the one we have been describing so far, we have implemented our method developing a conversion algorithm from the arrival times

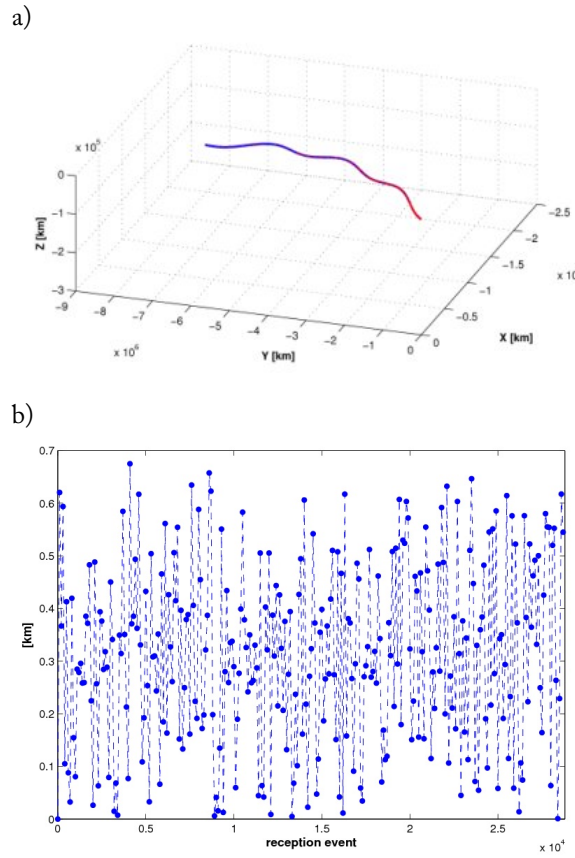


FIGURE 4. Motion of the Earth with respect to the fixed stars during three days, reconstructed using the arrival times of four pulsars at the site of the Parkes observatory in Australia. (a) Global view; the scale does not allow to distinguish between the reconstructed trajectory and the ephemerides. (b) The values of the positioning during the same three days; they are in the order of hundreds of meters.

measured by the receiver into the reconstructed space-time evolution of the observer. Then we have applied our tool to the signals from four real pulsars as they would be received at the site of the Parkes observatory in Australia [10]. In practice the arrival times were simulated using the TEMPO2 programme, which has been developed by the astrophysics community to study the pulsars and can be used to simulate the sequence of the signals from known pulsars at any position on the surface of the Earth. Our simulated data taking has been prolonged for three days and has produced the result synthetically visible in fig. 4.

In the figure one sees the space trajectory of the Earth with respect to the pulsars, assumed to be fixed stars.

Actually the reconstructed orbit is superposed to the expected path given by the ephemerides. At the scale of the graph in a) it is impossible to catch any difference between the two curves, but in fact the simulated trajectory fluctuates about the fiducial one according to the assumed accuracy in the determination of the arrival times. The absolute positioning error during the same period is visible in part b) of the figure; it is in the order of a few hundred meters.

In order to verify the response of our programme to the uncertainties in the measurement of time by the observer we have run some preliminary tests simulating an observer at rest with the fixed stars. A typical result (with one space dimension suppressed) can be seen in fig. 5. The asymmetry between the x and y directions is due to the non-fully symmetric distribution of the pulsars around the hypothetical user.

For the test we have simulated the actual behaviour of the onboard clock superposing to the fiducial arrival times a nanosecond Gaussian noise. Consistently the reconstructed position of the receiver displays a dispersion of the order of approximately 40 cm.

5 Fixed stars versus artificial sources

The idea of using pulsars for navigation and positioning purposes was put forth since the early times of their discovery [7] but everybody is perfectly aware of the fact that, though appealing, radio-pulsars are very faint objects so that their signals are many orders of magnitude below the noise at corresponding frequencies [12]. This means that big antennas and refined elaboration techniques are needed in order to receive their pulses; the size of the antenna could be reduced considering X-ray pulsars, but the receiving device should be out of the atmosphere and the problem of the intensity of the signal remains [13]. It is true that recognizing a known pulsar is not the same as looking for unidentified new objects, as people using radiotelescopes do, but anyway the use of pulsars would be difficult and limited to a few and expensive cases. Once however the method is adopted and validated there is no reason for excluding artificial pulsating sources. Actually if we allow for moving emitters we have an ample choice of different solutions. The relevant requisite is that the worldline of the emitter must be known; in practice in our algorithms we shall have time depending direction cosines and time depending relativistic γ factors with respect to the reference frame in which we decided to represent both the sources and the user. The rate of change of the time dependent values will have to be small enough not to spoil the linearization procedure for the receiver's worldline. If the emitter is an artificial one, we may of course think of using much higher frequencies than the ones we find in pulsars: GHz's will not be a problem. Since the piecewise linearization is made over times of a few tens of the emission periods at most, the relative stability will have to be kept over tens or hundreds of μ s.

Supposing the source is carried by a spacecraft whose path in the Solar System is well known, or even by a satellite orbiting the Earth, the relative speeds of these vehicles with respect to the user can be of the order of, say, $\sim 10^4$ m/s. This means that the emitter during the integration time of the algorithm moves, at most 1 m. At a distance ranging from thousands to millions of km the displacement corresponds to angles from μ rads.

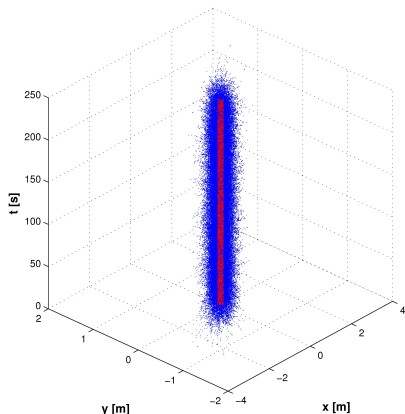


FIGURE 5. Worldline of an observer at rest. The blue dots are obtained from the simulated arrival times of the signals from four pulsars; the red line is the real spacetime position. The dispersion is contained within 40 cm.

down to $n\pi$ rad or less. Coming to the expected rate of change of the relative velocity of the emitter with respect to the receiver, we see that at the highest credible acceleration we have room for changes of the speed at most in the order of 1 cm/s. A change of this amount produces a corresponding change in the γ in the order of 1 part in 10^{19} which is negligible.

Similar results hold also when we imagine our emitters to be laid down on celestial bodies, such as the Moon, or Mars, or the asteroids.

Summing up, a permanent structure to enable the navigation in the Solar System could consist of a set of sources of electromagnetic pulses located on celestial bodies and on freely orbiting spacecrafts. Such a system could also be integrated by the use of a limited number of pulsars. In all cases, even though the minimum number of emitters is four, the sources on which to rely will have to be more than four: redundancy is important (as it is the case also for the present terrestrial GPS) because some of the sources, for periodic occultation or for any other reason, may turn out to be unavailable for a while. Let us add, that for purely geometrical reasons the distribution of the sources in the sky of the user should always be as even as possible in order to optimize the accuracy of the positioning. This again implies a redundant number of emitters, especially if their position changes with time.

6 Conclusion

We have seen that it is possible, for positioning purposes, to exploit periodic pulses from sources with known worldlines. The use of null vectors makes the method intrinsically relativistic, so that no ad-hoc correction is needed. If the time interval within which it is possible to treat the user's worldline as being straight is not less than ten times the longest period of the emitters, simple linear relations between the arrival times of the pulses from different sources hold. Solving the corresponding system of linear equations allows the reconstruction of the worldline of the user.

If you were starting a journey at a given moment and from a given position, you need to know several things such as the position of the initial event with respect to an arbitrary reference frame, the position in the sky of at least four pulsating sources and their possible motion and the period of the pulses from each source in a reference frame where the source is at rest.

Applying our algorithm, the whole worldline of the

traveler can be reconstructed with respect to the start event in the chosen reference frame. The accuracy of the positioning depends on the distribution of the sources in the various directions and on the precision of the clock the observer uses to measure the time from one pulse and the other.

The use of pulsars as sources has been considered, though it is limited by the extreme weakness of the signals and the need for comparatively long integration times and the concentration of the pulsars in the galactic plane (uneven distribution in space). However, we have been able to simulate the reconstruction, by means of pulsars, of the worldline of a point of the surface of the Earth.

We have then discussed the application of our method to artificial emitters of pulses. In this case we would have the possibility to use higher frequencies, then shorter integration times, and much higher intensities, then a cheaper and more manageable hardware for the detection and treatment of the signals. In the case of an artificial source we need also to know the worldline of the emitter. In order to build a navigation support network in the Solar System we could think to place a number of our pulsating emitters on different celestial bodies and onboard freely falling spacecrafts.

Unlike the present situation, a space mission could be self-guided using the connection with the navigation support network. The spacecraft would have to be equipped with an antenna designed to receive the pulses from the network and to recognize from which one of the sources they come, a clock, a memory containing the ephemerides of the sources from the initial event of the journey onward and a computing facility with a resident simple linear algorithm. No need for remote control would remain, except for some calibration from time to time. Of course the technological requirements of the equipment listed above have to be discussed carefully. For instance the antenna must be designed so that it can catch the pulses from at least four sources simultaneously by use of a set of either omnidirectional or wide aperture elements with different orientations in space. Hopefully the determination of the direction from which the signals arrive is not necessary as far as the parameters of the source are entirely known, so that it will be sufficient to recognize the source from its "signature".

The attention has been concentrated on the space missions, however there is no reason to exclude more familiar applications for positioning on or around the Earth. Using a constellation of high Earth orbit satel-

lites as primary sources would provide the equivalent of the present GPS, without the need for Sagnac periodic re-synchronization of the clocks from Earth. The next generation of Galileo satellites could be an opportunity to test our method in the terrestrial environment. For a practical test, actually four micro-satellites in high Earth orbit broadcasting regular pulses could be enough.

The effort should now be concentrated on technological elements such as clocks, receivers, processing units, energy consumption and miniaturization etc. The prospective of an autonomous navigation among the planets makes all this worth doing.

References

- [1] D. Bini, A. Geralico, M. Ruggiero, and A. Tartaglia. Emission versus Fermi coordinates: applications to relativistic positioning systems. *Class. Quantum Grav.*, 25(20):205011, 2008.
- [2] M. Blagojevic, G. J. F., W. Hehl, and Y. N. Obukhov. Real null coframes in general relativity and GPS type coordinates. *Phys. Rev. D*, 65(4):044018, 2002.
- [3] B. Coll. Relativistic Positioning Systems. *AIP Conf. Proc.*, 841:277–284, 2006.
- [4] B. Coll, J. J. Ferrando, and M. J. A. Positioning with stationary emitters in a two-dimensional space-time. *Phys. Rev. D*, 74(10):104003, 2006.
- [5] B. Coll, J. J. Ferrando, and J. A. Morales. Two-dimensional approach to relativistic positioning systems. *Phys. Rev. D*, 73(8):084017, 2006.
- [6] P. Delva, U. Kostić, and A. Čadež. Numerical modeling of a Global Navigation Satellite System in a general relativistic framework. *Advances in Space Research*, 47:370, 2011.
- [7] G. Downs. Interplanetary navigation using pulsating radio sources. *NASA Technical Report*, (JPL-TR-32-1594, NASA-CR-140398):1–18, 1974.
- [8] NASA. Space Shuttle Main Engines. http://www.nasa.gov/returntoflight/system/system_SSME.html.
- [9] C. Rovelli. GPS observables in general relativity. *Phys. Rev. D*, 65(4):044017, 2002.
- [10] M. Ruggiero, E. Capolongo, and A. Tartaglia. Pulsars as celestial beacons to detect the motion of the Earth. *Int. J. Mod. Phys. D*, In press:10, 2010.
- [11] M. Ruggiero and A. Tartaglia. Mapping Cartesian coordinates into emission coordinates: Some toy models. *Int. J. Mod. Phys. D*, 17(2):311–326, 2008.
- [12] J. e. a. Sala. Feasibility Study for Spacecraft Navigation System Relying on Pulsar Timing Information. *European Space Agency, the Advanced Concepts Team, Ariadna Final Report*, (03-4202), 2004.
- [13] S. I. e. a. Sheikh. Spacecraft Navigation Using X-Ray Pulsars. *J. Guid. Control Dynam.*, 29(1):49–63, 2006.
- [14] A. Tartaglia. Emission coordinates for the navigation in space. *Acta Astronaut.*, 67:539–545, 2010.
- [15] A. Tartaglia, M. Ruggiero, and E. Capolongo. A null frame for spacetime positioning by means of pulsating sources. *Advances in Space Research*, 47:645–653, 2011.



Acta Futura 4 (2011) 41-51

DOI: 10.2420/AF04.2011.41

**Acta
Futura**

Artificial Curiosity for Autonomous Space Exploration

V. GRAZIANO^{*}, T. GLASMACHERS, T. SCHAUL, L. PAPE, G. CUCCU, J. LEITNER AND J. SCHMIDHUBER

IDSIA, Galleria 2, 6928 Manno-Lugano, Switzerland

Abstract.

Curiosity is an essential driving force for science as well as technology, and has led mankind to explore its surroundings, all the way to our current understanding of the universe. Space science and exploration is at the pinnacle of each of these developments, in that it requires the most advanced technology, explores our world and outer space, and constantly pushes the frontier of scientific knowledge. Manned space missions carry disproportionate costs and risks, so it is only natural for the field to strive for autonomous exploration. While recent innovations in engineering, robotics and AI provide solutions to many sub-problems of autonomous exploration, insufficient emphasis has been placed on the higher level question of autonomously deciding what to explore. *Artificial curiosity*, the subject of this paper, precisely addresses this issue. We will introduce formal notions of “interestingness” based on the concepts of (1) compression progress through discovery of novel regularities in the observations, and (2) coherence progress through selection of data that “fits” the already known data in a compression-based way. Further, we discuss how to construct a system that exhibits curiosity driven by the interestingness of certain types of novel observations, with the mission to curiously go where no probe has gone before.

1 Introduction

Technology, and science in general, has progressed to the point that we can send intricate machines which are computationally powerful into space. So advanced are these machines that their potential easily exceeds what can be accomplished by manual control from Earth: the bandwidth of the sensors, such as cameras, usually exceeds the bandwidth of the communication channel between space probe and mission control, and more importantly, the enormous time latency involved in the exchange of signals imposes strict limitations on the efficiency of manual control. The efficiency of these probes could be greatly enhanced if they were able to carry-out missions and explore autonomously. For efficient autonomous exploration a probe needs to be as like a scientist as possible. In this paper we discuss the concept of *artificial curiosity* [12, 15] and how it can be used to best approximate the decisions a scientist might make, guided by his own knowledge, understanding, and curiosity.

Ideally, the device controller should make informed decisions on which information to send back to Earth, and what to do next in order to optimally achieve its mission goals. However, building such a controller solely based on assumptions and information available years before a mission begins does not really solve the problem. The very nature of an exploratory mission is to encounter novel, and unexpected information. One

^{*}E-mail address: vincent@idsia.ch

cannot provide *a priori* behaviors to efficiently study unpredicted phenomena. A more functional design might include on-board control software capable of autonomously classifying a piece of information such as an image or a situation as interesting or not worthwhile to investigate or even transmit back to Earth, based on the goals of the spacecraft. The probe could also then send interesting information to Earth with priority over non-interesting information. More importantly, rather than to wait for mission control to analyze the information and send back an appropriate action plan, our space probe could actively explore the interesting phenomenon until it has gained some understanding thereof and no longer classify it as interesting. Different phenomena would then become promising sources of novel information and attract the interest of our probe.

However, information collected this way serves another purpose beyond being reported to Earth: it may facilitate decision making in the future, enabling the agent to bootstrap detection and understanding of complex phenomena, based on simpler ones learned earlier in the mission. This automatic adaptation to previously unknown phenomena further increases the probe's autonomy from mission control. It enables the probe to respond more appropriately to circumstances not foreseen at design time than any catch-all algorithm might.

Intelligent autonomous control in active agents such as space probes is addressed within the field of artificial intelligence. A control algorithm or 'agent', such as a so-called reinforcement learner [5, 23], abstracts a spacecraft into two types of components: sensors that provide observations of the environment, and actuators that effect the surrounding environment, including the agent itself. The control algorithm bridges the sensory and motor systems. In reinforcement learning language, we talk about an agent or controller, that learns a policy which determines the actions taken by the agent, given the history of observations and actions.

For every interaction with the environment, be it exploratory or otherwise, the algorithm updates the policy based on success or failure of the action sequence attempted. The measure of success or failure is usually encoded into a single *reward* signal [23]. This way the agent learns from experience and autonomously improves its policy over time. However, the big open challenge in this learning paradigm is how to decide where to look and what to try next in order to maximize the learning progress. Humans seem to make such decisions with relative ease, driven by their internal curiosity. The idea behind artificial curiosity is to transfer this

internal human drive to reinforcement learning, making autonomous exploration practical. This amounts to providing the learning agent with an automatically available internal curiosity reward signal.

In this article we describe a route for transforming a probe into a more autonomous agent. We will achieve this goal in two conceptual steps, which are both related to the design of an internal feedback signal guiding curiosity. First we provide the probe with a way to measure the interestingness of its sensory inputs, which allows it to passively judge the observations it makes. Then we come to the active part, the crux of autonomy, namely how to come up with action plans or behaviors that lead to exciting new observations, which is known as *artificial curiosity* [11, 13]. We then close the article with a discussion on human curiosity as a driving force of scientific research.

Let us begin by introducing a number of concepts prerequisite to the notion of artificial curiosity.

2 What Is Interesting?

Although we are aiming for an autonomous decision maker, let us first restrict ourselves to an agent which cannot take any actions, e.g., a probe which passively monitors its environment. Here, the design goal for an autonomous agent reduces to detecting interesting pieces of information among the vast stream of incoming observations. To thoroughly address this problem we need a solid definition of interestingness, as well as practical algorithms for classifying information as such. However, the notion of interestingness, although intuitively clear, got formalized only relatively recently, using the concept of *learning progress* [11], in particular *compression progress* [18].

Let us look at an example. Assume a probe (a rover) is equipped with sensors to continuously monitor its surroundings. Although we are ultimately interested in making the rover explore its surroundings autonomously let us for the moment focus only on specific observations: the simple thermal sensor records, a single number at each time step, capturing some information about its environment. Let us assume that the sensor records its readings as plain text strings, consisting of the time of the reading, taking a measurement each minute, and the temperature in Kelvin, with an accuracy of 1/10 Kelvin. A typical record might read:

12/25/2030 14:11 | 288.6 K,

where the first entry indicates the date and time at mission control when the reading was taken. This is one possible encoding of the information, in both human and machine readable format. Of course, this is an arbitrary choice, and there are many ways to encode the same information, some more compact than others. For example, including the start date and time elapsed in every record makes each record a complete piece of information, but it is highly redundant within the stream of records. We can save storage space by noting the start date only once. Knowing that the temperature is recorded once a minute means that we do not even need a time stamp at all; the time of a measurement can be deduced from the time the series of measurements started and the index of the record in the list. Moving to a smarter encoding that saves storage space is known as *compression* [7]. Saving storage may or may not be a big deal for our space probe, but it surely is when sending the information through a limited bandwidth channel. Moreover, we will see in the following that the ability to compress information can have far-reaching implications for our explorer.

Given that using shorter encodings is beneficial, is there a better way to compress our data? The first step in compression is to look for *patterns* in the data. A pattern can be defined as something that, on any level of abstraction, repeats itself. For example, fractals possess self-similarity and repeat their pattern at every scale, the decimal expansion of π is the result of the repeated application of the same numerical procedure. Once a stream of data is analyzed, and repetitive trends are found, they can be exploited for the construction of a *model* of the pattern. When analyzing our temperature data we will find a profile which, more or less, repeats with each rotation of the planet. The values will rise in the morning and drop in the evening. A compressor can store this pattern once and then use it as a model to compress future observations. It makes use of this model by storing only the differences of the measurements from the model. These representations of the temperatures will, on average, be smaller than the actual values, thereby shortening the length of the encoding.

Typical (loss-less) general purpose compression algorithms exploit different types of patterns. One strategy is to build up a dictionary of frequent patches of information and patterns which can be referenced with short codes. In contrast, statistical encoding relies on a probability model of which information is expected to occur next, such that the most probable next temperature can be encoded with a very short code [3], while for example

rare jumps in temperature will have longer codes. These two strategies are often combined, such as in the famous Lempel-Ziv-Welch algorithm [24], which is the basis of the `gzip` tool, an often-used program for data compression on computers.

A model that fits the data well allows a compressor to code the information compactly. This means that the optimal model is problem-dependent. In the extreme case we arrive at the notion of Kolmogorov complexity [6, 7, 21]. The Kolmogorov complexity of a sequence is defined as the length of the shortest program (in a universal programming language) encoding this information. This formal approach to compression turns out not to be realizable in practice. Instead, one has to fall back to approximations and heuristics, such as dictionaries and statistical prediction, and be content with compressors that at best only approximate the ideal compressor and the shortest possible encoding of the data. However, even such imperfect compressors can be extremely powerful. For example, the models built by the human brain, which include tremendously useful concepts such as hierarchies (ranging from abstract to concrete notions), are all of the latter type, and can be realized as instances of compression. In addition, compression is intimately related to the concept of Occam's razor: the principle of preferring models with fewer assumptions (among the models that explain the data) translates to choosing the shortest program that compresses the data [1, 21].

We want to emphasize that the compressor has *learned* something about the environment by studying it, discovering patterns, and then constructing a model from these patterns. Building a model which explains some aspect of the environment, in the case of our probe the typical daily behavior, not only allows us to compress observations, but also represents what we have learned about the environment, and allows us to make *predictions* about future events [4, 21]. Applying the model to the (past) events used to construct the model itself allows the compressor to encode these events with short codes, resulting in data compression. We use the term 'prediction' for information obtained from the model, even when applied to data from the agent's history.

As discussed above, the notions of pattern, model, prediction and compression are intimately related. Learning is then the process of finding patterns in data and incorporating them into a model, which again allows the compressor to encode with shorter codes, and thus to compress and predict better. Although predictability and compressibility are not *quite* the same [9],

we can use a measure of compression to express the quality of predictions a model can make about information in the environment. We will see that this notion also leads to a straight-forward definition of interestingness.

The process of learning or training in this passive scenario of monitoring the world and processing data is understood as *learning to predict* (in contrast to learning to act well). This is the same as learning to compress. The goal of learning is thus equivalent to finding shorter and shorter codes for a given stream of data. However, as noted above, there is a lower bound on the length of an encoding that a compressor can find. Thus, the learning progress, measured by the decrease in length of the compressed representation, will essentially vanish as the length of the code approaches the length that an ideal compressor would produce. If the model is suitable for the problem at hand, this means that it will have learned to predict all the data arbitrarily well, leaving nothing else to learn. So what makes data or information *interesting*? Continuing the line of thought above, the extent to which new information is interesting is related to how much the model of the environment stands to improve by observing it. This concept is caught compactly by the notion of *compression progress*. Using the connection between prediction and compression, we now phrase the statement as such: information is interesting if it allows us to more succinctly code the observations we have made in our environment.

The drive to actively seek out data which allows for the learning of more expressive and compact models over time (or in other words, the drive to compress data with shorter programs) is known as *curiosity* [15]. The goal of curiosity is to maximize the pace of learning patterns and regularities. A rover can use this drive to learn new rules to govern its exploration strategy.

3 Compression Progress

Now that we have introduced and justified the utility and role of compression progress, we show how to formalize that notion. Broadly speaking, compression progress is a measure of how much the ability to compress the history of observations improves by either learning new patterns (from the history) or by making new observations.

We will discuss several aspects of this: (1) an adaptive compressor can learn previously unknown patterns and regularities by revisiting the history (by way of a change in the compressor), (2) new observations might yield ad-

ditional data obeying unknown but learnable laws, (3) new observations might also increase the internal *coherence* of the history, leading to a better compressibility of the augmented history, even without a change in the compressor (by way of a change in the data).

3.1 Coherence progress

To simplify matters, this paper will mostly focus on the last aspect, *coherence progress* [10]. We assume a fixed compressor; for example, say, the `gzip` tool. The progress of such an algorithm may change as new observations arrive. A new observation can be compressed in the context of the history, and the overall compressibility of the history changes accordingly. Hence, the progress is directly attributed to the current observation, and results in a (partial) measure of its interestingness.

To formalize this, we first introduce the auxiliary concept of *compression similarity*

$$S(a, b) = L(a) + L(b) - L(a + b) ,$$

which is a measure of how closely two sequences a and b are related to each other. Here, $L(\cdot)$ is the length of a compressed sequence when using a fixed compressor. In other words, $S(\cdot, \cdot)$ is a measure of how many bits can be saved by compressing two sequences together, as opposed to compressing them separately. We can generalize this to the notion of *compression coherence* of a single sequence:

$$C(h) = \frac{1}{n-1} \sum_{i=1}^{n-1} S(h_{1:i}, h_{i+1:n}).$$

In words, coherence is the average compression similarity between two partitions of the history, cut at index i . Coherence progress can then be defined as the increase in compression coherence, when incorporating a new observation into the history, measured in bits:

$$\begin{aligned} P_h(o_{n+1}) &= C(h_{1:n} + o_{n+1}) - C(h_{1:n}) \\ &= C(h_{1:n+1}) - C(h_{1:n}), \end{aligned}$$

3.2 Compression Progress

Now let us turn to the general case of learning compressors, the focus of most previous work on interestingness [11, 22, 14, 15, 16, 19, 18, 17, 20]. In contrast to a fixed tool such as `zip`, an adaptive compressor is able to make compression progress simply by revisiting the history, that is, without the need of additional observations

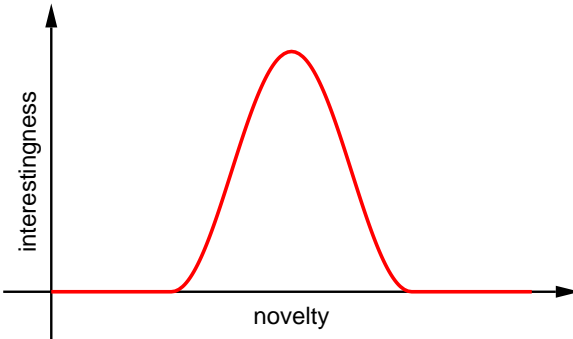


FIGURE 1. A Wundt Curve. Measures of interestingness date back to Wundt [25]. Wundt's curve shows the interestingness of an observation as a function of novelty. Novelty, unlike complexity, depends on the relationship between the information and the person observing it. Trivial patterns quickly lose their novelty, while noise is always novel. As learning proceeds the complexity of the most interesting patterns increases. From the artificial curiosity point of view, novelty can be considered inversely proportional to compressibility: noise has a low compressibility, and trivial or simple patterns have a high compressibility.

[15, 20] (although additional observations may make it easier to achieve compression progress). This progress is achieved by a change in the compression strategy, which can be interpreted as a gain in the understanding of the history. For example, a search process may find a new rule that allows the compressor to better predict forthcoming observations, thus encoding them from then on with shorter codes. Or an adaptive architecture, such as a recurrent artificial neural network, might adapt its synaptic weights to better reflect some aspect of the dynamics of the environment, again resulting in an even more powerful anticipation of observations.

Processes that lead to compression progress without additional observations are coupled with improvements of existing models, or with the emergence of completely new models. As discussed earlier, this added predictive power amounts to better understanding the sequence of observations, and thus the environment. This way, an adaptive compressor can adapt to its environment, building increasingly more complex rules on top of the pre-existing ones.

Let us treat this situation of an adaptive compressor in the terms of the length function L and the history $h_{1:n}$ introduced above. By re-visiting and re-compressing the history, an adaptive compressor can change its encoding, and thus the length function itself. It is straightforward that the progress of a change of encoding, re-

sulting in a new length function \tilde{L} , should be measured by

$$L(h_{1:n}) - \tilde{L}(h_{1:n}) .$$

Even more general measures of learning progress also take into account the time needed for compressing and decompressing the data [15]. Because of the nature of restructuring its compression strategy by means of detecting additional patterns and gaining improved understanding of the history, this type of progress cannot be attributed solely to a particular observation. Rather, it is also to be attributed to the restructuring process itself. Although learning a better compressor may be costly in terms of computational resources such as time and memory, this process too can have a measure of interestingness attributed with it, one that is consistent with the measure used with new observations.

3.3 Relation of Interestingness to Coherence Progress

Setting aside the interestingness associated with learning a better compressor, we now return to the compression progress-independent interestingness associated to particular observations. Our measure of coherence progress already captures a number of desirable properties of interestingness.

For the purposes of the present section, a new observation is uninteresting when we cannot make coherence progress from it. This may happen for completely different reasons: The observation may be easily compressible, either because the observation is trivially compressible by itself (e.g., a long string of zeros, $L(o_{n+1}) \approx 0$), or because its information is redundantly present in the observation history already (the sunrise temperature increase, after having observed hundreds of sunrises before), if the underlying pattern (here, periodicity) has been discovered already, i.e., $L(h_{1:n+1}) \approx L(h_{1:n})$. In both these cases, $P_h(o_{n+1})$ will be low.

On the other hand, patterns may be so complex that we cannot find predictive models. This may happen either because we lack the necessary prerequisites (such as basic skills or knowledge) for discovering the patterns, or because the observation is actually random; in both cases we have $L(h_{1:n+1}) \approx L(h_{1:n}) + L(o_{n+1})$, and thus $P_h(o_{n+1})$ will be low. In principle it is therefore difficult to tell a random phenomenon from a pattern we fail to catch. However, given enough observations with an underlying regularity, and a compressor that is able to find this regularity, the history of observations can be

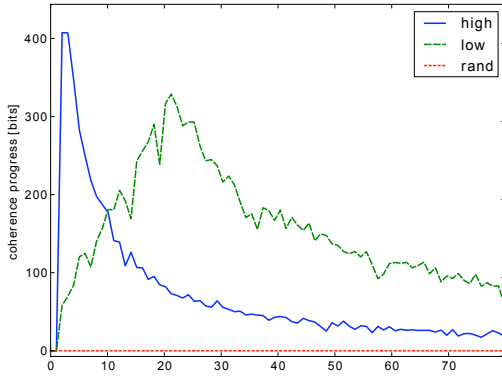


FIGURE 2. Illustration of the qualitative effect of aspects of interestingness, measured in terms of coherence progress $P_h(o_{n+1})$ achieved by a new observation, when added to the current history $h_{1:n}$ (where n is on the horizontal axis). The time profile of coherence progress evolves differently, depending on the amount of overlap between individual observations. The three classes from which the observations are drawn are the following. The plot in blue (solid line) shows observations with high overlap, where every observation shares 80% of its information with every other one (individual stones, say). For them coherence progress is high initially, but quickly decays, as the underlying patterns are easy to spot and then compress – observations from $n = 15$ onwards convey but few new insights. The plot in green (broken line) shows observations with low overlap (approximately 10%, different planets, say), in which case coherence progress only kicks in after the history has accumulated sufficient observations (around 20 here) for each new one to increase the coherence significantly (e.g., when different planet categories start to emerge). This class has more total information, and a more complex underlying structure, which is the reason why coherence progress stays comparatively high for a long time. In red (dotted), we show the plot for a sequence of random observations: the coherence progress is zero throughout, as expected.

stored in a much shorter form; for example, a child will find a course on advanced statistics completely boring, while a student with the necessary prerequisites may be fascinated. See Figure 1 for an informal illustration of how interestingness relates to the compressibility of observations.

It is important to note that data are not inherently interesting. What is currently interesting depends on context, namely, what we already know. For $P_h(o_{n+1})$ to be large, the new coherence $C(h_{1:n} + o_{n+1})$ needs to exceed the previous coherence $C(h_{1:n})$, which again means that new observations need to support the discovery of patterns in our experience for which we did not have sufficient evidence before. In order to keep things interesting we may profit from continually dis-

covering new patterns. Consequently, as we learn more, that is as our predictive model becomes stronger, we have to turn to environments where pattern discovery was originally too difficult. For example, we finally enroll in the advanced statistics course. This happens for two reasons: (i) contexts in which pattern detection was extraordinarily difficult appear relatively more interesting because we already figured out the simpler patterns and (ii) more importantly, having discovered a base of rules by first exploring simpler environments allows us to extend these rules to more complex patterns in more complex environments. A result of learning is that we can learn things we previously were unable to. Figure 2 illustrates this point by showing how the values of coherence progress evolve as observations (from a given class) are accumulated. The coherence progress is measured for three different classes, each with different degrees of shared information between the observations. Among other things, it also shows that there can be a trade-off between short-term and long-term progress.

Given that our formal definition of coherence provides a quantitative measure of certain aspects of interestingness, correctly capturing certain key qualitative aspects (noise is never interesting, redundant information quickly becomes uninteresting), that is simple to compute and understand, we will use it in the next section as a feedback signal that can inform an autonomous agent on where to explore next. In this way we are able to base a variant of artificial curiosity, the informed drive to explore aspects of the environment that maximize coherence progress, on a qualitative measure.

4 Choosing Actions

An agent equipped with intrinsic motivation, such as artificial curiosity, is able to control its behavior and steer itself autonomously towards places and phenomena that are *quantitatively interesting*. Such an agent, clearly, could play an important role in space exploration. We now discuss how to realize such an agent, making an autonomous robot more of a curious scientist. We want the agent to choose an action that results in interesting observations. How can we create such a curious agent?

Firstly, we need to extend our agent, which so far only does passive monitoring. Obviously, it is not enough for an agent to simply observe changes in its environment if it is to seek out interesting data. It must be able to perform different actions (e.g., move a sensor or its entire self), and more to the point, it must choose ac-

tions which actually lead to the observation of interesting data.

Without a good model of the world that agent can not know in advance which actions will most probably result in interesting observations. At the same time, without exploration the agent does not have access to observations from which it could build a sufficiently detailed model of its environment. Artificial intelligence research has resolved this dilemma by using, e.g., reinforcement learning algorithms [23]. Such algorithms are designed to bootstrap both action policy and world model at the same time. Typically, such algorithms are applied to autonomously achieve a pre-defined goal, encoded in a reward signal. Such a goal-related reward signal is known as *external reward* in the literature. With new observations and reward signals becoming available, reinforcement learning algorithms change their policy to make actions that have been rewarding in the past more likely in the future. This feedback, over time, shapes the behavior of the system, enabling it to evolve specialized strategies that achieve arbitrary pre-specified goals.

The decisive trick that turns an agent into a curious explorer is to provide the very same class of algorithms with a different type of feedback signal, namely with so-called *internal* or *curiosity reward* [12, 20]. This is the most direct way to reflect the drive for finding interesting observations in a control algorithm. Let us have a closer look at its different components in the following.

The agent needs to have a *model* of the world that represents what has been learned about the environment so far. Again, the role of this model is twofold: it allows for a compression of the history of its observations, and more relevant in this case, it allows the agent to make predictions about future events. The agent also needs a *way to update* the internal world model as new observations are made. Most of the time it is sufficient to refine the existing model, but sometimes it may be necessary to find a completely fresh model, one that integrates newly discovered phenomena with the previous model and possibly resolves conflicts between old assumptions and new data. Such learning and updating of models based on data is a prototypical task for machine learning algorithms, and can be implemented for example with artificial neural networks.

In order to choose better actions the robot needs *feedback* on how well it is performing. In the reinforcement-learning paradigm, such feedback is encoded into a reward signal. Based on the observations that follow an action, we can either increase or decrease the likelihood

of the action in similar, future situations.

In the case of a curious explorer this goal can be cast as a drive to improve the internal world model, for which the curiosity reward is received. From previous sections we know that such improvements can be measured in terms of compression progress, hence, the curiosity reward feedback is the progress made by the system. Note that this curiosity feedback signal cannot be formulated as a function of the state of the agent and its environment. Instead, it depends on the agent's internal state, particularly on the predictive power of its current world model.

Let's now extend our original example, the fixed probe measuring the temperature on a planetary surface. Consider the same probe attached to a vehicle or rover. The rover allows for simple actions, say: left, right, forward, backward, and stay. If we allow the robot to curiously explore at will, after generating a first model from its observations, it will begin by choosing actions either randomly or according to some ad-hoc scheme. Based on its observations the reinforcement learning algorithm will modify the likelihood of the actions so as to maximize the reward signal.

In this example the robot will detect a uniform, boring, temperature distribution on the surface, but when it enters a crater it will happen upon a different temperature pattern. This temperature pattern will be novel, and non-random, and therefore interesting. With enough exploration of the phenomenon the robot will make compression progress and enjoy a curiosity reward. This reward signal will then be used by the learning algorithm to increase the likelihood of action sequences that find such regions. As long as the pattern is not fully incorporated into the world model the agent will receive reward for exploration in this area. Continuing, the next time the agent discovers a crater, the temperature profile will again change. A crater of roughly the same size and shape will have the same profile and will generate little reward, exploration will not last long in this area. However, the exploration of a crater of a different shape will remain rewarding. Explorations of craters of different sizes will carry-on until the robot's model is capable of predicting the temperature profile of any crater.

A space probe that is driven by artificial curiosity will lead to the discovery and the modeling of unpredicted phenomena. This probe would not need the direct intervention of human scientists to guide it towards such phenomena, nor would its behavior need to be predetermined and programmed ahead of time. But a probe is typically sent into space with goals other than pure ex-

ploration. Often very specific experiments, predefined by scientists on Earth, or constraints on exploring only specific parts of space or certain phenomena are put on the spacecraft. A robot driven solely by exploration is simply not realistic. How then can a curious agent best serve us? Given the goals of a specific space mission we can define a goal to be used in the feedback of our reinforcement-learning algorithm.

Say we want our robots to mine some distant planet for a particular ore. The more ore they mine the better. Our feedback signal is easy to design. But, where is the ore? And what is the best way to mine on this unfamiliar planet? These are questions that the curiosity reward can help answer, by exploring and developing a world model that allows better prediction about the nature of the planet so that the most ore can be mined.

Moreover, how does an agent balance *exploration*, developing a model via an intrinsic reward signal, and *exploitation*, using its model to directly fulfill its goals? This is a non-trivial problem. In general it is hard to balance the exploration and the exploitation of an environment so as to maximize the external reward. It becomes particularly difficult when other constraints, such as limited lifetime and energy usage, are taken into account. Regardless, a reinforcement learning algorithm can learn when to explore and an agent equipped with artificial curiosity gives the agent a guided, open-ended, way to explore so it may better improve its collection of external reward.

Over the years various formalizations of curiosity have been researched by Schmidhuber et al. [20]. Some of them include intrinsic reward based on prediction error [12], world model improvements, differences between prior and posterior beliefs of agents before and after learning new data [22], as well as zero-sum intrinsic reward games of two players, each trying to out-predict or surprise the other, taking into account the computational costs of learning, and learning *when* to learn and *what* to learn [14]. There are other approaches as well for adding intrinsic motivation to artificial agents, e.g. [8].

Although it is conceptually clear how a route toward building curious autonomous agents looks like, the current state-of-the-art in machine learning may not yet be sufficient for realizing such behavior in a space probe. We identify two different types of bottlenecks: First, current compressors are mostly limited to specific domains, such as text, images, sound and video. Far more powerful model-building learning methods are required to build compressors that capture the world

in the way human scientists do. Second, a reinforcement learner that makes sense of the internal curiosity feedback generated by the compression-based coherence module needs to scale gracefully to larger and more complex environments. This requires progress in the field of reinforcement learning, since current methods are typically limited to small, simple, and low-dimensional tasks.

Current research focuses on finding ways to bring together the measure of compression progress, which is used as an intrinsic reward signal, with general yet practically feasible reinforcement-learning methods. These are yet to be implemented in real world and robotic systems. In our lab we focus on the implementation of these ideas in humanoid robots in real-world environments, as for example, in the E.U. funded project: IM-CLEVER¹.

5 Curiosity in Science

Compression progress is not only a useful principle for learning machines, such as curious space probes; it also reflects an important aspect of human scientific interest. By improving the subjective compressibility of the history of observations we obtain shorter and simpler descriptions of that history. The regularities that facilitate a short, simple description of the history can be regarded as rules that describe the structure of our observations. Conversely, we can understand our observations in terms of the rules we have thus far discovered. These rules or *compression programs* ultimately form the scientific description of our world. Driven by the desire to find shorter descriptions of their observations, scientists *actively focus* their attention (e.g. build measuring devices, perform experiments) on gathering data that allows them to find or validate better compression programs [15, 18]. Physicists, for example, have traditionally analyzed certain aspects of the world to find simple models to describe their limited observations better than previous models. In essence they are trying to find programs that compress observed data better than the best previously known program. For example, Newton's law of gravity can be formulated as a short program which allows for substantially compressing many observation sequences involving falling apples and other objects. Although its predictive power is limited – for example, while it does not explain the quantum fluctuations of the electrons inside an apple, it still allows for a large

¹<http://www.IM-CLEVER.eu/>

reduction in the amount of data required to encode the observations of falling objects, by assigning short codes to events that obey this law. Einstein's general relativity theory yields additional compression progress as it compactly explains many previously unexplained deviations from Newton's laws of motion.

More generally, scientists try to find increasingly compact rules to describe certain aspects of the world that are consistent with rules found elsewhere, for other aspects. However, a description of a system (e.g., a planet's surface) on a certain abstraction level (e.g., particle physics) does not immediately yield insights into all the phenomena related to that system (e.g., craters). Instead, scientists try to achieve further compression and more general explanations by finding rules that allow for shorter descriptions of the concepts known thus far. Such a collection of rules, or a *compression program*, can itself then become a concept to which a certain name is given. For example, planetary scientists obviously do not describe planet surface phenomena on the level of particle physics, but instead use more abstract concepts that allow for shorter descriptions of their observations. They might find it useful to introduce the concept of a crater, based on repeated occurrences of a depression in the planet's surface with a particular shape. The same principle applies for many other concepts we use to describe our world; the concept of a molecule allows for a short description of many aspects of stable configurations of its atoms, the concept of an atom allows for a short description of certain configurations of protons, neutrons and electrons, and so on. Similarly, we can identify more abstract concepts, such as 'turbulence,' for a distribution of motion in a liquid or gas, that is regular over a range of scales and allows, once again, for a shorter representation of a significant part of turbulent motion. In this fashion, the amount of compression that can be achieved serves as a criterion for determining the abstraction level on which a phenomenon can best be described. Compression programs for individual concepts on different abstraction levels can again be compared for similarities and grouped by inter-compressibility, potentially yielding further compression. Such an organization of compression programs takes a hierarchical form in which more abstract concepts describe increasingly general relations between concepts on different levels of abstraction. Although compression progress is essential to science, the idea that we should use simple programs to describe our world does not make how to find such programs explicit. As, for example, shown in [2], simple file

compression methods (gzip) can already be used to infer some regularities associated with the concept of 'life,' but not all compression methods used in science might be so straightforward.

The compression of a history of observations not only entails identifying the rules, regularities or models that describe particular physical processes, but also finding the level of abstraction on which physical entities are best represented. Similarly, compression *progress* consists of not only finding shorter rules which describe an ever larger number of observations, but also finding more abstract concepts to which the rules apply. In this fashion, a space probe driven by artificial curiosity could learn to form representations similar to the concepts formed by human scientists. For example, a space probe could learn to represent observations of 'craters' with a short program based on similarities in their shape. After this abstract concept is in place, it could learn to find models for the processes surrounding craters, for example, 'erosion'. Moreover, it could then actively direct its attention or even manipulate its environment, just as scientists perform experiments, to gather observations that allow to further compress its history of observations.

6 Conclusion

We have discussed a formal notion of curiosity within a framework of an agent that, from the interactions with its environment, learns to focus on observations with patterns that were not yet identified. Informal notions related to curiosity, such as complexity, pattern, regularity, novelty, interestingness, were captured in a general computational framework based on compression. Compression programs allow an agent to store its history of observations based on identified regularities underlying those observations. The interestingness of incoming observations can be determined relative to the agent's current ability to compress its history of observations. In particular, interestingness can be measured as *compression progress*. We also introduced a method for measuring the extent to which new data fits old data, called coherence progress.

Many algorithms and methods developed in artificial intelligence and computer science in general, such as gzip, neural networks, pattern recognition or dimensionality reduction, ultimately perform some kind of compression. Of course, most of the existing methods have their own particular limitations: e.g., only success-

ful with specific data types (such as text documents, images or music), do not produce human-readable representations, are overly time or resource intensive. While the current state of the art in machine learning is yet unable to address all these issues in general applications, a major advantage of our approach is that the interestingness of observations is determined *relative* to the pattern discovery ability of the compressor. Patterns that can be easily discovered by a certain compressor soon become boring, while patterns that can never be found by a compressor will also not be interesting. Instead, a curious agent focuses its actions on collecting observations for which its *limited* compressor can find regularities that were not yet discovered in the history of observations thus far. As researchers develop better and more flexible compression methods, the capability of curious artificial intelligence can be extended within the general framework of compression progress.

Artificial curiosity in artificial intelligence is closely related to human curiosity in scientific investigation. Scientists not only try to find regularities in previous observations, they also actively collect new observations that allow them to find even better compression programs. Autonomous exploring probes should resemble human scientists in that regard and use artificial curiosity to discover concepts similar to those found by human scientists.

References

- [1] A. Blumer, A. Ehrenfeucht, D. Haussler, and M. K. Warmuth. Occam's razor. *Information Processing Letters*, 24:377–380, 1987.
- [2] F. Corsetti and M. Storrie-Lombardi. Lossless compression of stromatolite images: A biogenicity index? *Astrobiology*, 3:649–655, 2003.
- [3] D. A. Huffman. A method for construction of minimum-redundancy codes. *Proceedings IRE*, 40:1098–1101, 1952.
- [4] M. Hutter. *Universal Artificial Intelligence: Sequential Decisions based on Algorithmic Probability*. Springer, Berlin, 2004.
- [5] L. P. Kaelbling, M. L. Littman, and A. W. Moore. Reinforcement learning: a survey. *Journal of AI research*, 4:237–285, 1996.
- [6] A. N. Kolmogorov. Three approaches to the quantitative definition of information. *Problems of Information Transmission*, 1:1–11, 1965.
- [7] M. Li and P. M. B. Vitányi. *An Introduction to Kolmogorov Complexity and its Applications* (2nd edition). Springer, 1997.
- [8] K. Merrick and M. Maher. Motivated learning from interesting events: adaptive, multitask learning agents for complex environments. *Adaptive Behavior*, 17(1):7, 2009.
- [9] J. Poland and M. Hutter. Asymptotics of discrete mdl for online prediction. *IEEE Transactions on Information Theory*, 51(11):3780–3795, 2005.
- [10] T. Schaul, L. Pape, T. Glasmachers, V. Graziano, and J. Schmidhuber. Coherence Progress: A Measure of Interestingness Based on Fixed Compressors. In *Fourth Conference on Artificial General Intelligence (AGI)*, 2011.
- [11] J. Schmidhuber. Curious model-building control systems. In *Proceedings of the International Joint Conference on Neural Networks, Singapore*, volume 2, pages 1458–1463. IEEE press, 1991.
- [12] J. Schmidhuber. A possibility for implementing curiosity and boredom in model-building neural controllers. In J. A. Meyer and S. W. Wilson, editors, *Proc. of the International Conference on Simulation of Adaptive Behavior: From Animals to Animate*, pages 222–227. MIT Press/Bradford Books, 1991.
- [13] J. Schmidhuber. Artificial curiosity based on discovering novel algorithmic predictability through coevolution. In P. Angeline, Z. Michalewicz, M. Schoenauer, X. Yao, and Z. Zalzala, editors, *Congress on Evolutionary Computation*, pages 1612–1618. IEEE Press, 1999.
- [14] J. Schmidhuber. Exploring the predictable. In A. Ghosh and S. Tsutsui, editors, *Advances in Evolutionary Computing*, pages 579–612. Springer, 2002.
- [15] J. Schmidhuber. Developmental robotics, optimal artificial curiosity, creativity, music, and the fine arts. *Connection Science*, 18(2):173–187, 2006.

- [16] J. Schmidhuber. Simple algorithmic principles of discovery, subjective beauty, selective attention, curiosity & creativity. In *Proc. 10th Intl. Conf. on Discovery Science (DS 2007), LNCS 4755*, pages 26–38. Springer, 2007. Joint invited lecture for *ALT 2007 and DS 2007*, Sendai, Japan, 2007.
- [17] J. Schmidhuber. Art & science as by-products of the search for novel patterns, or data compressible in unknown yet learnable ways. In M. Botta, editor, *Multiple ways to design research. Research cases that reshape the design discipline*, Swiss Design Network - Et al. Edizioni, pages 98–112. Springer, 2009.
- [18] J. Schmidhuber. Driven by compression progress: A simple principle explains essential aspects of subjective beauty, novelty, surprise, interestingness, attention, curiosity, creativity, art, science, music, jokes. In G. Pezzulo, M. V. Butz, O. Sigaud, and G. Baldassarre, editors, *Anticipatory Behavior in Adaptive Learning Systems. From Psychological Theories to Artificial Cognitive Systems*, volume 5499 of *LNCS*, pages 48–76. Springer, 2009.
- [19] J. Schmidhuber. Simple algorithmic theory of subjective beauty, novelty, surprise, interestingness, attention, curiosity, creativity, art, science, music, jokes. *SICE Journal of the Society of Instrument and Control Engineers*, 48(1):21–32, 2009.
- [20] J. Schmidhuber. Formal theory of creativity, fun, and intrinsic motivation (1990-2010). *IEEE Transactions on Autonomous Mental Development*, 2(3):230 –247, 2010.
- [21] R. J. Solomonoff. A formal theory of inductive inference. Part I. *Information and Control*, 7:1–22, 1964.
- [22] J. Storck, S. Hochreiter, and J. Schmidhuber. Reinforcement driven information acquisition in non-deterministic environments. In *Proceedings of the International Conference on Artificial Neural Networks, Paris*, volume 2, pages 159–164. EC2 & Cie, 1995.
- [23] R. S. Sutton and A. G. Barto. *Reinforcement Learning: An Introduction*. MIT Press, Cambridge, MA, 1998.
- [24] T. Welch. High speed data compression and decompression apparatus and method, Dec. 10 1985. US Patent 4,558,302.
- [25] W. M. Wundt. *Grundzüge der Physiologischen Psychologie*. Leipzig: Engelmann, 1874.



Acta Futura 4 (2011) 53-68

DOI: 10.2420/AF04.2011.53

**Acta
Futura**

A Dynamical System Approach to Astrodynamics

ALESSANDRA CELLETTI ^{*}, CHRISTOPH LHOTKA [†]

Dipartimento di Matematica, Università di Roma Tor Vergata, Via della Ricerca Scientifica 1, I-00133 Roma (Italy)

Abstract. Perturbation theory is a well-recognized and effective tool to analyze the stability properties of models in Astrodynamics; in particular, KAM and Nekhoroshev's theorems allow to understand the long term behavior of nearly-integrable dynamical systems. Following the work of Lagrange, Poincaré and Conley, the combination of Dynamical Systems, chaos theory and Lagrangian points gave birth to new concepts of space missions, nowadays known as Space Manifold Dynamics. The fields of application of perturbation techniques involve also problems of rotational dynamics, like the spin-orbit problem or the pitch model. In this context, we provide analytical and numerical results to investigate the stability properties of the dynamics.

1 Introduction

Merging the knowledge of Dynamical Systems, Celestial Mechanics and Astrodynamics has produced many advances in spacecraft mission analysis and design. A new branch of Astrodynamics, the so-called Space Manifold Dynamics (hereafter SMD), has made an impressive impact on the way of thinking about spacecraft

trajectories (see, e.g., [4], [5], [28], [35]). The classical technique to design space trajectories is based on patching together the solutions of the 2-body problem; the new interplanetary orbits of SMD are designed by making use also of the complicated (sometimes chaotic) structure of the N-body phase space. The development of the ideas, which lead to this new discipline, is a fantastic *paradigm* of how science evolves: J.-L. Lagrange ([37]) discovered five (triangular and collinear) equilibrium points (in the synodic frame) of the restricted 3-body problem, but he thought that his results had just an academic interest, since he passed away many decades before the first asteroid close to one of the equilibria was observed (i.e., 588 Achilles discovered in 1906). In 1968 the mathematician C. Conley ([14]) exploited the power of the unstable collinear points and he proved mathematically the existence of low-energy transit orbits leading the spacecraft from one primary to the other with a minimum expense of fuel, though the time to reach the goal might notably increase with respect to the application of the method of patched conics. Ten years later, space agencies started to develop interplanetary missions fully exploiting the Lagrangian points and the chaotic trajectories from the Hiten spacecraft ([42]) to ISEE-3, SOHO, MAP, etc.

A key role in the analysis of new trajectories using Dynamical Systems tools is played by the celebrated Kolmogorov–Arnold–Moser (hereafter KAM) and Nekhoroshev's theorems ([34], [1], [45], [46]). Under very general assumptions, KAM theory provides re-

^{*}E-mail address: celletti@mat.uniroma2.it

[†]E-mail address: lhotka@mat.uniroma2.it

sults on the stability of motions in Hamiltonian systems, which are small perturbations of integrable ones (more specifically, KAM theory establishes the persistence of invariant tori with fixed frequency for infinite times). On the other hand, Nekhoroshev's theorem provides the confinement of the actions (e.g., semimajor axis, eccentricity, inclination in the N-body problem) over exponential times. The original applications of these theorems provided results very far from being of practical interest in Astronomy. However, the development of computer-assisted techniques, including the construction of adapted algebraic manipulators for perturbative series expansions, allowed us to obtain results in agreement with the observed values of the astronomical parameters (see, e.g., [8], [10] and references therein). It is worth stressing that both theories allow also for the development of numerical techniques apt to investigate the stability of the dynamical systems, with the advantage of having a strong theoretical support. In fact, KAM theory provides tools for the construction (by a Newton's method) of invariant tori as well as of stable and unstable manifolds; Nekhoroshev's theorem serves as the basis for techniques for the computation of the stability times and for the description of the interlaced geography of resonances. Both theories are based on the development of suitable normal forms, which can be efficiently implemented on algebraic manipulators. In this work we consider two models associated to orbital and rotational problems in Astrodynamics: a 3-body problem to describe the orbital motion of a spacecraft and a rotational model to investigate its attitude stability. Both models are described by a nearly-integrable Hamiltonian system (such that KAM and Nekhoroshev's theorems can be applied). Since the dynamics of celestial bodies is always affected by (eventually small) dissipations, we take into account also dissipative models. As an example, we consider the pitch problem including a non-rigid structure of the spacecraft and the effect of an atmosphere. We remark that recent perturbative methods have been developed to encompass the dissipative case, through the computation of suitable normal forms ([9], [11]).

This paper is organized as follows. Section 2 reviews the basic facts about the Lagrangian points; we present in Section 3 the motivations for the development of Space Manifold Dynamics, leading to new methods for the design and analysis of interplanetary trajectories. The stability problem motivating the development of KAM and Nekhoroshev's theories is described in Section 4. An example of Nekhoroshev's type estimates is given in

Section 5, while applications of KAM theory and numerical tools for studying the stability character of the dynamics are presented in Section 6. Some conclusions are drawn in Section 7.

2 The Lagrangian solutions

We consider the restricted 3-body problem, formed by a body P with mass μ , which moves in the gravitational field of two primaries P_0, P_1 with masses μ_0, μ_1 , respectively; we assume that $\mu_0 > \mu_1 \gg \mu$, which implies that the primaries P_0, P_1 are not influenced by P (restricted problem). We consider a reference frame with the origin coinciding with the barycenter of the primaries; in this setting, we define r and Δ as the distances of P from P_0 and P_1 , while r' is the distance between the primaries and ϕ is the angle formed by the directions of r, r' . Let the reference plane coincide with the invariable plane of motion, formed by the unperturbed Kepler motion of the primaries, and let the positive x -axis be along the direction joining the primaries. In this setting we introduce the orbital elements (a', e', M') to describe the Keplerian motion of P_1 at any time, being respectively the semimajor axis, the eccentricity and the mean anomaly. To describe the motion of P , we introduce the orbital elements $(a, e, i, \omega, \Omega, M)$, where the inclination i , the argument of pericenter ω and the longitude of the ascending node Ω define the orientation of the osculating Keplerian ellipse. For $\mu_1 = 0$ the quantities $(a, e, i, \omega, \Omega)$ are constants, while $M = nt + M_0$, being M_0 the initial value and n the mean motion. Under the influence of P_1 , all orbital elements of P become functions of the time. We refer to the former as the unperturbed motion and to the latter as the perturbed motion, respectively. Without loss of generality we normalize to unity the gravitational constant G as well as we set $r' = 1, \mu_0 + \mu_1 = 1$, so that the angular velocity of rotation is unity. To a first approximation we assume that P_1 moves on a circular orbit ($e' = 0$) and that the motion of P is confined to lie in the invariable plane of motion ($i = 0, \Omega = 0$). The problem in the synodic frame is shown in Figure 1, where the two primaries P_0 and P_1 are kept fixed in the coordinate system which is uniformly rotating around the barycenter of P_0 and P_1 with the angular velocity of the primaries. In this set-

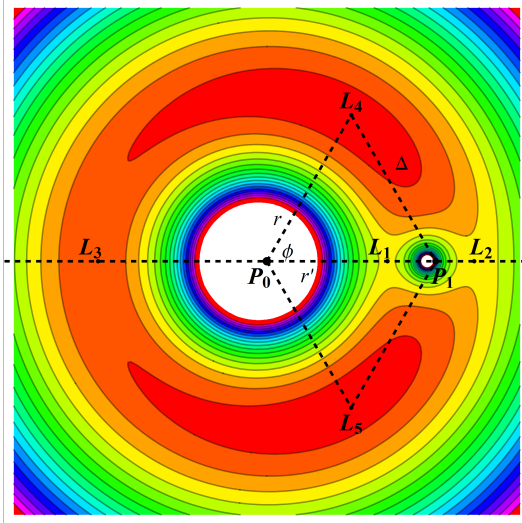


FIGURE 1. Hill's curves and the geometry of the restricted 3-body problem for $\mu_1 = 5 \cdot 10^{-2}$; the Lagrangian equilibrium points are denoted by L_1, L_2, L_3 (collinear), L_4, L_5 (triangular).

ting, the equations of motion for P can be written as

$$\begin{aligned}\ddot{x} - 2\dot{y} &= \frac{\partial \Omega}{\partial x}, \\ \ddot{y} + 2\dot{x} &= \frac{\partial \Omega}{\partial y},\end{aligned}\quad (1)$$

where the potential Ω is defined by

$$\Omega(x, y) = \mu_0 \left(\frac{r^2}{2} + \frac{1}{r} \right) + \mu_1 \left(\frac{\Delta^2}{2} + \frac{1}{\Delta} \right).$$

We look for the minima of the potential Ω to define the equilibrium points; a standard computation shows that the fixed points are located either on $y = 0$ for x depending on the mass ratio μ_0/μ_1 as well on special points, which form together with the location of P_0 and P_1 an equilateral triangle (with $\phi = 60^\circ$). The former are known as *collinear*, the latter as *triangular* (or equilateral) equilibrium points; they are numbered from L_1 to L_5 as shown in Figure 1. A plot of the potential along the line $y = 0$, say $\Omega(x) = \Omega(x, 0)$ is given in Figure 2 for $\mu_1 = 5 \cdot 10^{-2}$. As it is well known ([50]), there exists a natural invariant of motion associated to (1), the so-called *Jacobi integral* C_J , which can be derived by multiplying (1) by \dot{x} and \dot{y} , and integrating their sum with respect to time to obtain the relation

$$\dot{x}^2 + \dot{y}^2 = 2\Omega - C_J,$$

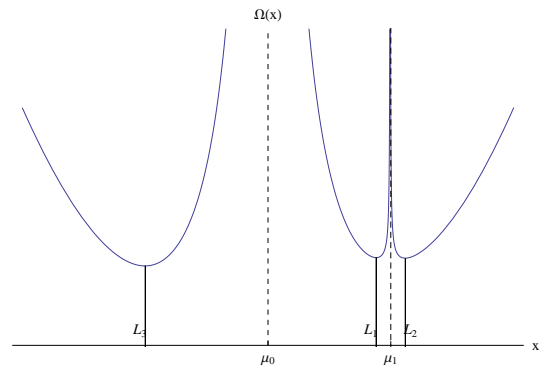


FIGURE 2. Minima of $\Omega(x) = \Omega(x, 0)$, corresponding to the collinear equilibrium points of the restricted problem for $\mu_1 = 5 \cdot 10^{-2}$.

where C_J is a constant. Since the square of the velocity cannot become negative, the motion is bounded by the relation $2\Omega - C_J \geq 0$. We report in Figure 1 different regions of the equipotential $\Omega(x, y)$ in color scale together with the zero velocity or Hill's curves. The form of Hill's curves for a given mass ratio μ_1/μ_0 mainly depends on the value of C_J and one can find regimes of closed regions, which imply stability of motion for all times. A detailed description of the topology of the zero velocity curves is shown in Figure 3. While for small C_J the zero velocity curves degenerate to the triangular Lagrange points themselves (3a), with increasing C_J they surround L_4 and L_5 symmetrically (3b) until they touch at the collinear equilibrium point L_3 (3c). Increasing again C_J we find one closed zero velocity curve, with the shape of a horseshoe (3d). For larger values of C_J the outer curve touches at the collinear point L_2 (3e), another connecting channel is opened (3f) until the inner curve touches at the equilibrium L_1 (3g). Finally we get two disconnected regimes (3h), encircling the two masses μ_0 and μ_1 , respectively. The Hamiltonian associated to the planar, circular, restricted 3-body problem, close to the 1:1 resonance, can be written in terms of Delaunay variables as ([7])

$$\begin{aligned}H(L, G, \tau, \omega, \lambda') &= -\frac{1}{2(1+L)^2} - (1+L) \\ &\quad - \mu_1 R(L, G, \tau, \omega, \lambda'),\end{aligned}\quad (2)$$

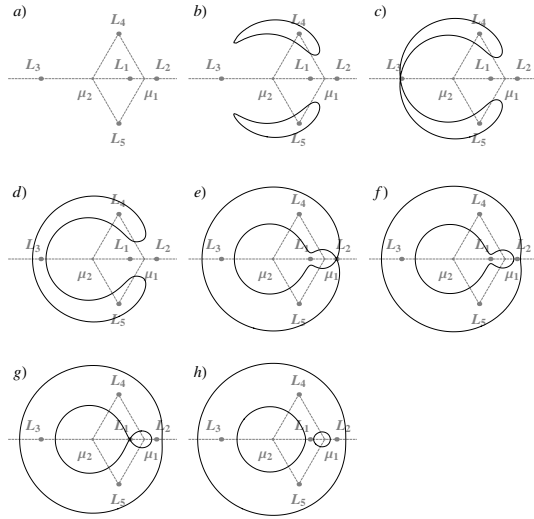


FIGURE 3. Types of zero velocity curves for different Jacobi-constants for $\mu_1 = 5 \cdot 10^{-2}$: a) $C_J = 3$, b) $C_J = 3.074$, c) $C_J = 3.0975$, d) $C_J = 3.15$, e) $C_J = 3.4019$, f) $C_J = 3.43$, g) $C_J = 3.4685$, h) $C_J = 3.55$.

where the modified Delaunay variables are defined in terms of the Keplerian elements as

$$\begin{aligned} L &= \sqrt{\frac{a}{a'}} - 1, \quad \tau = \lambda - \lambda', \\ G &= \sqrt{\frac{a}{a'}} \left(\sqrt{1 - e^2} - 1 \right), \quad \omega \end{aligned}$$

and λ, λ' are the mean orbital longitudes of P and P_1 , respectively. The Hamiltonian (2) is nearly integrable, since for $\mu_1 = 0$ it reduces to the Kepler's problem in the rotating coordinate system. However, for $\mu_1 \neq 0$ the disturbing function $R(L, G, \tau, \omega, \lambda')$ introduces a more general (non-integrable) dynamics. The restricted planar, circular, 3-body problem serves as a basic model for different kinds of space scenarios as we will see in the next Section. Indeed, L_1, L_2, L_3 are not stable, but with an additional amount of propulsion it is possible to keep the spacecraft close to those points. On the other hand L_4 and L_5 , being gravitationally stable, are good candidates for next generation space stations or observatories ([20]). This suffices to motivate the increasing interest for the study of the dynamics near the Lagrangian points.

3 Space Manifold Dynamics

The transfer of a spacecraft between different trajectories is classically obtained through a patched conic approximation, each 2-body approximation being valid within different spheres of influence ([2]). An alternative to such classical techniques in Astrodynamics has been recently proposed by merging the knowledge of Celestial Mechanics, Dynamical Systems and Flight Dynamics. The overall technique goes under the name of *Space Manifold Dynamics*, which we are going to shortly present here ([5], [28], [35]).

As it is well known, the Keplerian motion is only a first approximation of the dynamics of the celestial bodies, namely the 2-body approximation provided, e.g., by the Earth and the spacecraft. A better description of the motion is obtained by adding the gravitational influence of a third body, e.g. the Moon. However, Henri Poincaré ([48]) showed that the 3-body problem is not integrable and that a complete analytical solution, like in the Keplerian model, cannot be provided. Nevertheless, the mass of the second primary is typically small with respect to the leading primary; in this case one can think of the 3-body problem as a perturbed 2-body problem (see Section 2). In our example the integrable part is provided by the motion of the spacecraft subject to the Earth, while the perturbation is due to the influence of the Moon. This class of *close-to-integrable* 3-body problems can be conveniently investigated through the so-called perturbation theory (see, e.g., [8], [23], see also [16] for an approach based on Lie series), which aims to remove the perturbation appearing in (2) to higher orders in the (normalized) perturbing parameter, i.e. μ_1/μ_0 . Since the work of Poincaré we know that, beside regular motions, the 3-body problem exhibits chaotic dynamics, characterized by an extreme sensitivity to variations of the initial conditions. As we will see later, an effective tool to distinguish between regular and chaotic motions is obtained through the computation of the Lyapunov exponents or related quantities called *Fast Lyapunov Indicators* ([24]). Chaotic motions are generated around the unstable equilibrium solutions, giving rise to homoclinic (i.e. intersections between stable and unstable manifolds belonging to the same equilibrium point) and heteroclinic (i.e. intersections between stable and unstable manifolds belonging to different equilibrium points) intersections at the crossing of the stable and unstable manifolds. Within the 3-body problem we have reviewed in Section 2 the existence of triangular and collinear equilibrium solutions in the synodic refer-

ence frame. The discovery dates back to J.-L. Lagrange, who believed that such equilibrium solutions were just a simple mathematical curiosity, since he passed away many decades before the first asteroid (588 Achilles in 1906) close to the triangular positions was observed. In 1968 the mathematician Charles C. Conley published a paper where new routes from Earth to Moon, alternative to the patched conic approach, are envisaged. The idea is to prove the existence of low-energy orbits through the collinear point L_1 : in order to have minimal fuel costs, the spacecraft moves on orbits whose Jacobi constant is just above that corresponding to the collinear point (see [14]). Figure 3 shows that in case g) there is no orbit connecting the primaries, but a slight decrease of the Jacobi constant as in case e) leads to the opening of the bottleneck allowing for transits between the primaries. The existence of transit orbits through the bottleneck is proven in [14] (see also [15]) by linearizing the equations of motion around L_1 and by using Moser's version of Lyapunov's theorem ([44]). Transit orbits are then provided by using the stable and unstable manifolds associated to L_1 (see Figure 4), which can be explicitly constructed using efficient numerical algorithms closely following the KAM proof given in [41], namely by solving the functional equation defining the tori through a Newton's method ([32]). More-

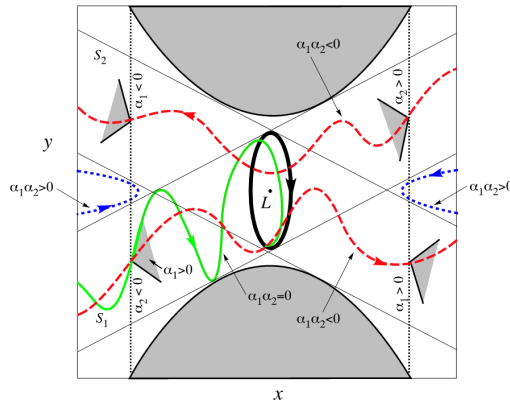


FIGURE 4. The dynamics around the bottleneck associated to L_1 . In green, non-transit orbits, in red, transit orbits (the picture is a copy of the original one in [14] obtained from [36]).

over, Conley showed that the low-energy orbits satisfy the following mission requirements:

- Minimizing Fuel: This is due to the low-energy needed, however this requirement must be compensated for by a much higher time for reaching

the goal.

- Control and Stability: the transfer of the spacecraft from the transit to the circumlunar orbit is obtained through a simply controlled impulse in the bottleneck region. This implies stability, since the transit time is small.
- Flexibility: outside the bottleneck region around the collinear point L_1 , one can approximate the motion by a 2-body problem where patched conics can be used to reach the Moon.

It is remarkable to mention that Conley concludes his paper with the following comment on the time required to reach the Moon by using the low-energy trajectories: "*Unfortunately, orbits such as these require a long time to complete a cycle (e.g., 6 months, though a modification of the notion might improve that)*". And later he adds: "*On the other hand, one cannot predict how knowledge will be applied – only that it often is*"; indeed, the foundations of SMD have been laid ([5], [28], [35]). New spacecraft trajectories are made possible through the concepts of chaos, KAM tori, invariant manifolds and Lagrangian points. By the way, some natural bodies already experienced such dynamics, like those asteroids in the 3:1 resonance with Jupiter, which get transported through chaotic orbits and eventually become Mars-crossing. The use of collinear points in Astrodynamics becomes nowadays very useful, thanks to the following facts: they provide a good observational point of the Sun (compare with the so-called *halo orbits*, i.e. 3-dimensional periodic orbits around a collinear point), the L_2 Moon–Earth collinear point can be used to establish communications between the Earth and the hidden side of the Moon, the collinear points provide an effective interplanetary transport, being natural dynamical channels, thus minimizing fuel. The first probe which used the Lagrangian points and the halo orbits, ISEE–3, was launched in 1978 to study the Earth's magnetic field and the solar wind. Later, many other missions profited of the peculiar dynamical geography around the Lagrangian points, like Hiten (1990), SOHO (1995), ACE (1997), MAP (2001), Genesis (2001), Herschel–Planck (2009). Many other missions are also planned in the future (e.g., JWST, Gaia, Kuafu, etc.).

Motivated by the success of these new ideas in Space Manifold Dynamics as started by C. Conley, we proceed to investigate the stability problem (see Section 4)

within the following frameworks, having relevance in Astrodynamics:

- i) The analysis of the stability of the triangular Lagrangian points, which can be performed through Nekhoroshev's theory (see Section 5).
- ii) The construction of the invariant tori through a suitable parametric representation as performed in KAM theory (see Section 6.1). This technique can be extended also to construct the stable and unstable manifolds around the collinear points.
- iii) The extension of the stability analysis to a particular model of rotational dynamics, including the effect of dissipative contributions (see Section 6.2).

4 The stability problem

Many celestial models can be seen as perturbations of integrable dynamical systems, like in the case of the restricted 3-body problem. A nearly-integrable system is described by a Hamiltonian of the form

$$H(J, \phi) = h_0(J) + \varepsilon h_1(J, \phi), \quad (3)$$

where $J = (J_1, \dots, J_d) \in \mathbb{R}^d$ are the actions, $\phi = (\phi_1, \dots, \phi_d) \in \mathbb{T}^d$ are the angle variables and ε is a small positive real parameter. The choice of action-angle variables comes from the fact that in the integrable approximation $\varepsilon = 0$ the associated canonical equations can be solved as follows:

$$\begin{aligned} \dot{J} &= -\frac{\partial h_0(J)}{\partial \phi} = 0 \\ \Rightarrow J(t) &= J(0) = \text{const.} \\ \dot{\phi} &= \frac{\partial h_0(J)}{\partial J} \equiv \omega(J) \\ \Rightarrow \phi(t) &= \omega(J(0))t + \phi(0), \end{aligned} \quad (4)$$

where $(J(0), \phi(0))$ denote the initial conditions.

From a mathematical point of view, the solution takes place on a torus with given frequency $\omega = \omega(J(0))$. However, for $\varepsilon \neq 0$ the equations of motion in terms of action-angle variables are of the form:

$$\begin{aligned} \dot{J} &= -\varepsilon \frac{\partial h_1(J, \phi)}{\partial \phi}, \\ \dot{\phi} &= \omega(J) + \varepsilon \frac{\partial h_1(J, \phi)}{\partial J}. \end{aligned}$$

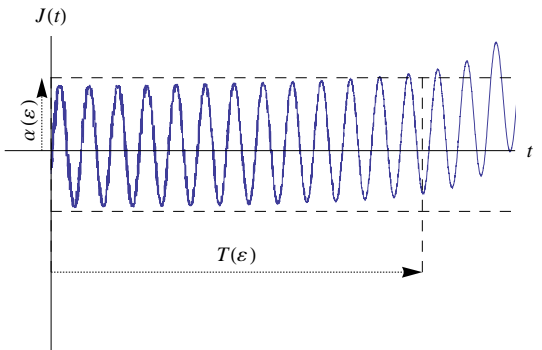


FIGURE 5. The stability problem (5).

One could argue that the motion is still on average ε -close to the integrable approximation or, in other words, that the effect of the perturbation becomes important only after a time $T \propto \varepsilon^{-1}$. We will see in the ongoing discussion that this is not always the case. To be more formal, let us investigate a stability problem such that the actions remain bounded over a given interval of time, namely there exists $\varepsilon_0 > 0$ such that for $\varepsilon \leq \varepsilon_0$:

$$|J(t) - J(0)| \leq \alpha(\varepsilon) \text{ for } t \leq T(\varepsilon), \quad (5)$$

where $T = T(\varepsilon)$ is the stability time and $\alpha = \alpha(\varepsilon)$ is some bounded function of ε (compare with Figure 5). As a first result, we can already state that for $\varepsilon = 0$ we have $T = \infty$ and $\alpha = 0$. It is interesting to investigate the parameter ranges, say $0 \leq \varepsilon \leq \varepsilon_0$ for some $\varepsilon_0 > 0$, which lead to one of the following conclusions for the solution associated to a Hamiltonian system of the form (3):

- i) There exist a perpetual solution, such that $|J(t) - J(0)| < \alpha(\varepsilon)$ for all times.
- ii) For solutions which are not perpetually stable, there exists a stability time $T(\varepsilon)$ such that $|J(t) - J(0)|$ is bounded for any $t \leq T(\varepsilon)$.

The seminal results provided by KAM and Nekhoroshev theories are motivated by the previous discussion. The content of KAM theory ([34], [1], [45]) is the following. Let us consider a nearly-integrable system of the form (3), such that for $\varepsilon = 0$ it admits the unperturbed solution (4). The hypotheses for the applicability of KAM theorem are the following:

1. The unperturbed Hamiltonian h_0 is non-degenerate, i.e. $\partial^2 h_0 / \partial J^2 \neq 0$.

2. The frequency of motion $\omega = \omega(J(0))$ is diophantine, namely, it satisfies the non-resonance condition $|\omega \cdot k|^{-1} \leq C|k|^s$ for any $k \in \mathbb{Z}^d$ and for some positive constants C, s .

The first assumption is needed to guarantee that the frequency of motion varies with the action J , while the second assumption is needed to control the small divisor problem arising in perturbation theory ([8]). If the perturbing parameter satisfies a smallness condition, say $\varepsilon \leq \varepsilon_0$ for some positive ε_0 , then KAM theorem ensures the persistence of an invariant surface for the perturbed system with frequency equal to the unperturbed frequency ω . We remark that KAM theorem does not impose restrictions on the stability time and therefore the existence of the invariant surfaces is guaranteed for eternity. The proof of the theorem is constructive in the sense that it provides an explicit algorithm to build the invariant torus through a perturbative Newton's method. Moreover, as we will see in Section 6.1, for systems with low degrees of freedom KAM theorem provides a strong stability property in the sense of confinement of the dynamics in the phase space by establishing the existence of two trapping tori.

The result due to Nekhoroshev ([46], [47]) concerns a stability theorem of type (5) by providing a bound on the diffusion of the actions for exponential times. In particular, Nekhoroshev's theorem yields that the functions α, T are of the form

$$\alpha(\varepsilon) = \varepsilon_0 \rho_0^a, \quad T(\varepsilon) = t_0 e^{(\frac{\varepsilon_0}{\varepsilon})^b}, \quad (6)$$

for some positive constants $\varepsilon_0, \rho_0, t_0, a, b$. Equation (6) states that the action variables stay bounded for a stability time which is exponentially long in ε^{-1} . The theorem can be applied, provided the unperturbed Hamiltonian h_0 satisfies a suitable non-degeneracy condition (even weaker than that required in KAM theorem), which is called in the original paper the *steepness condition* ([46]). Since this condition requires a somehow complicated mathematical formulation, in most literature this assumption is replaced by the so-called *quasi-convexity* condition on h_0 (see, e.g., [25], [26]). More precisely, a Hamiltonian h_0 is said to be quasi-convex if at least one of the following inequalities holds true for any $v \in \mathbb{R}^d$ ($\|\cdot\|$ denotes the Euclidean norm):

$$\begin{aligned} |\omega(J) \cdot v| &> \ell \|v\|, \\ \frac{\partial^2 h_0(J)}{\partial J^2} v \cdot v &\geq m \|v\|^2 \end{aligned}$$

for some positive constants ℓ, m . We remark that the stability time depends only on the parameters t_0, ε_0, b , strongly connected to the geometry and dimensionality of the system. Although former studies ([39], [40], [43]) already indicated an exponential stability behavior of the solution of some dynamical systems, the proof followed 20 years later ([46]). In his famous work Nekhoroshev gave the detailed analysis of the action space based on the so-called *geography of the resonances*. With this result it was possible to prove a global stability theorem, valid in an open domain of the phase space.

5 Stability of the triangular points

In order to illustrate the powerful results which can be obtained through Nekhoroshev's theorem, we analyze the stability of the Earth–Moon triangular Lagrangian points within the framework of the planar, circular, restricted 3-body problem. The main technical tool for the analytical studies leading to stability theorems of the form (5) is the so-called *normal form*. In Hamiltonian systems normal forms are achieved by means of a change of coordinates, such that in the new set of variables the system (3) can be written in cartesian coordinates as

$$\begin{aligned} H^{(r)}(J^{(r)}, \phi^{(r)}) &= \\ h_0^{(r)}(J^{(r)}; \varepsilon) + \varepsilon^{r+1} h_{r+1}(J^{(r)}, \phi^{(r)}) \end{aligned}$$

where r is the order of normalization. We call $h_0^{(r)}$ the (integrable) normal form and $\varepsilon^{r+1} h_{r+1}(J^{(r)}, \phi^{(r)})$ the remainder at the r -th order of normalization. The equations of motion in normal form coordinates become

$$\begin{aligned} \frac{d\phi^{(r)}}{dt} &= \omega^{(r)}(J^{(r)}; \varepsilon) + \varepsilon^{r+1} \frac{\partial h_{r+1}}{\partial J^{(r)}}, \\ \frac{dJ^{(r)}}{dt} &= -\varepsilon^{r+1} \frac{\partial h_{r+1}}{\partial \phi^{(r)}}, \end{aligned}$$

being $\omega^{(r)}(J^{(r)}; \varepsilon) = \partial h_0^{(r)} / \partial J^{(r)}$. Therefore, under the assumption that the norm of $\varepsilon^{r+1} h_{r+1}(J^{(r)}, \phi^{(r)})$ is small, up to the order $O(\varepsilon^{r+1})$ the solution in normal form coordinates is given by

$$\begin{aligned} \phi^{(r)}(t) &= \omega^{(r)}(J^{(r)}(0)) t + \phi^{(r)}(0), \\ J^{(r)}(t) &= J^{(r)}(0) = \text{const.} \end{aligned} \quad (7)$$

The solution describes the motion on the torus with frequency equal to $\omega^{(r)}(J^{(r)}(0))$. Note that the solution

(7) is given in terms of the variables $(J^{(r)}, \varphi^{(r)})$, together with a normalized frequency $\omega^{(r)}$. Estimates of the form (5) rely on the evaluation of the norm of the remainder function and of the generating function, which defines the symplectic transformation S from original to normalized variables, say $S : (J, \varphi) \rightarrow (J^{(r)}, \varphi^{(r)})$. While the former will give upper bounds on the stability time, the latter can be used to give bounds on the deviation of the actions. In order to obtain stability estimates of the Lagrangian points of the Sun–Earth system, we consider a variant of Nekhoroshev’s theorem, the so-called isochronous version ([22], [29]), where the perturbing parameter ε is replaced by the distance, which is assumed to be small, from the elliptic equilibrium point:

$$\begin{aligned} |\rho(t) - \rho(0)| &\leq \rho(0)^a \text{ for any} \\ t &\leq T = t_0 e^{\left(\frac{\rho_*}{\rho}\right)^b} \end{aligned} \quad (8)$$

for some $t_0 > 0$ constant; here $\rho = \rho(t)$ is the distance from the equilibrium point at time t , ρ_* is the maximum distance up to which the “Nekhoroshev’s regime” applies and the exponents a, b are parameters depending on the number of degrees of freedom. The stability time is exponential in the inverse of the distance ρ , which is bounded by the quantity $\rho(0)^a$. This variant of Nekhoroshev’s theorem is useful close to elliptic equilibria ([10], [18], [38]) and it can be implemented also in the case of symplectic mappings ([3]). As in Section 2 we assume that the eccentricity of the Earth is zero, say $e' = 0$, and we derive a 2-dimensional symplectic mapping, which is suitable to describe the dynamics close to the Lagrangian point L_4 . This can be done by using the averaged disturbing function:

$$\bar{R} = \frac{1}{2\pi} \int_0^{2\pi} R(L, G, \tau, \omega, \lambda') d\lambda',$$

and by deriving the mapping equations via a generating function (see [30]) of the form:

$$\begin{aligned} W &= \tau_n L_{n+1} + \omega_n G_{n+1} \\ &- 2\pi \left(\frac{1}{2(1+L_{n+1})^2} + (1+L_{n+1}) + \mu_1 \bar{R} \right). \end{aligned}$$

In the circular averaged case G is a constant of motion and the relevant dynamics reduce to a 2-dimensional surface of section, which is defined by the symplectic

transformation in phase space:

$$\begin{aligned} \tau_{n+1} &= \frac{\partial W}{\partial L_{n+1}} \\ &= \tau_n - 2\pi \left(1 - \frac{1}{(1+L_{n+1})^3} + \right. \\ &\quad \left. \mu_1 \frac{\partial \bar{R}}{\partial L_{n+1}} (\tau_n, L_{n+1}) \right), \\ L_n &= \frac{\partial W}{\partial \tau_n} \\ &= L_{n+1} - 2\pi \mu_1 \frac{\partial \bar{R}}{\partial \tau_n} (\tau_n, L_{n+1}). \end{aligned}$$

The mapping in the present form can be used as an implicit symplectic integrator of the averaged system to obtain the solution vector for initial conditions $(L(0), \tau(0))$ at discrete times $t = 2\pi n$. A typical phase portrait obtained from the averaged Hamiltonian equations for the Sun–Earth ratio is given in Figure 6. The fixed points located at $M - M' = 60^\circ$ and 300° correspond to L_4 and L_5 ; they are of elliptic type and they are surrounded by librational invariant curves. The fixed point located at $M - M' = 180^\circ$ is a saddle (corresponding to L_3); the separatrix going through L_3 separates the rotational and librational regime of motion. The phase portrait was obtained for the Sun–Earth mass ratio for $e' = 0$ and $e = 0$ on a grid of initial conditions to cover the different regimes of motion. It is interesting to investigate the stability of the equilibrium points over long time scales. This can be performed through numerical studies (including also additional perturbative effects), like it was done e.g. in [17], or by means of pure analytical methods ([19], [21]) leading to Nekhoroshev type stability estimates. In its simplest application of the theorem one uses the Taylor series expansion of the generating function close to one of the elliptic equilibrium points. The resulting mapping is polynomial in the canonical variables and it can be rendered explicit using iterated series inversions. Moreover, it is convenient to diagonalize the linear form of the mapping and to write it in complex conjugated variables using a suitable coordinate transformation based on the eigensystem of the linearized mapping equation. In general, mappings of the present type can then be written in a very compact form as

$$z_{n+1} = \Omega_\omega z_n + \sum_{k \geq 2} F_k(z, \bar{z}), \quad (9)$$

where $z, \bar{z} \in \mathbb{C}^d$ ($d > 0$) and $\Omega_\omega = (e^{i\omega_1}, e^{i\omega_2}, \dots, e^{i\omega_d})$ is a d -dimensional vector of

complex numbers associated to the linear frequency vector $\omega \equiv (\omega_1, \dots, \omega_d)$ of the unperturbed twist mapping. The perturbation can be split as the sum of its contributions F_k , labeled by the polynomial order defined by $k = \sum_{l=1}^d (a_l + b_l)$ for monomials of the form $z_1^{a_1} \bar{z}_1^{b_1} \dots z_d^{a_d} \bar{z}_d^{b_d}$. To obtain estimates on the stability time we seek, like in the continuous case, for a change of coordinates $S : z \in \mathbb{C}^d \rightarrow \zeta \in \mathbb{C}^d$, such that in the new variables the mapping equations become

$$\zeta_{n+1} = \Omega_{(\omega+\omega')} \zeta_n + R^{(r+1)}(\zeta, \bar{\zeta}), \quad (10)$$

where $\zeta, \bar{\zeta} \in \mathbb{C}^d$ are the transformed variables, $\Omega_{(\omega+\omega')}$ is the shifted frequency vector of the normalized mapping and $R^{(r+1)}$ denotes higher order contributions. We call (10) the Birkhoff normal form of the mapping (9) and $R^{(r+1)}(\zeta, \bar{\zeta})$ the remainder at the normalization order r . If the latter can be neglected, the motion is confined to lie on invariant circles in each hyperplane and in the vicinity of the central equilibrium. However, in general the remainder will cause a drift of the radii, defined by $\rho = \zeta \bar{\zeta}$, on times approximately inverse to the size of the norm of $\|R^{(r+1)}\|$. It was shown in ([38]) that in the case of the Lagrangian configurations, close to the equilibrium point L_4 or L_5 , the distance from the equilibrium ρ and the stability time T are connected via the relation:

$$\rho = 2^{-\frac{1}{2-r}} \left((r-2) \left(\frac{r}{r-2} \right)^r \|R^{(r+1)}\| T \right)^{\frac{1}{2-r}},$$

where r is the order of normalization. The expression is related to (8) in case the norm of the remainder $\|R^{(r+1)}\|$ becomes exponentially small; in that case it was possible to prove the confinement of the initial conditions close to the triangular equilibria for exponentially long times ([38]).

6 Attitude dynamics and KAM theory

In order to describe the results which can be obtained by applying KAM theory, we consider the attitude dynamics of a spacecraft, more precisely, we introduce two different models in rotational dynamics. The spin-orbit problem and the pitch model. The former model is considered within a conservative setting; for any non-zero eccentricity of the satellite's orbit, the model is described by a 1-dimensional, time-dependent, second-order differential equation. KAM theory provides a tool to construct an explicit approximate solution and to provide

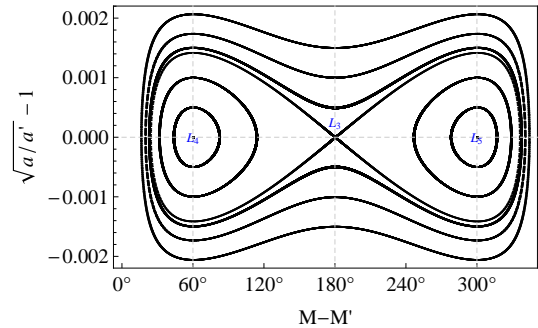


FIGURE 6. Phase portrait of the Lagrangian averaged problem for the Earth-Sun model. The elliptic fixed points situated at $M - M' = 60^\circ$ and 300° correspond to the triangular equilibrium points L_4 and L_5 . They are surrounded by invariant librational curves. The saddle at 180° corresponds to the unstable equilibrium point L_3 .

results about the stability of the satellite's motion. The pitch model concerns the motion of a non-rigid, asymmetric spacecraft on a circular orbit within a slightly resisting medium. Also this model is described by a 1-dimensional, time-dependent, second-order differential equation. The regular and chaotic character of the dynamics is analyzed through the implementation of the so-called Fast Lyapunov Indicators (see Section 6.3). Numerical tools, like Poincaré surfaces of section and the computation of the FLIs, are used in both models to investigate the dynamical stability.

6.1 The spin-orbit model

A simple model describing the rotational dynamics of a spacecraft S is obtained as follows. We assume that the satellite has a triaxial shape with principal moments of inertia $A > B > C$; we also assume that the barycenter of the spacecraft moves around the primary P on a Keplerian orbit. Concerning the rotation of the spacecraft we assume that the spin-axis coincides with the shortest physical axis and that it is perpendicular to the orbit plane (more interesting models would release the latter assumption by allowing the spacecraft to have an obliquity). After normalizing the units of measure so that the mean motion is unity (i.e. the period of revolution is 2π), this model is described by the second-order differential equation (see [8])

$$\ddot{x} + \varepsilon \left(\frac{a}{r} \right)^3 \sin(2x - 2f) = 0, \quad (11)$$

where $\varepsilon \equiv 3/2(B - C)/A$, a is the semimajor axis, r is the orbital radius and f is the true anomaly, while x is the angle formed by the longest physical axis (belonging, by assumption, to the orbital plane) and the periapsis line (see Figure 7). A *spin-orbit resonance* occurs whenever the period of revolution is proportional through a rational number to the period of rotation. A *synchronous resonance* occurs whenever the two periods are equal as in the case of a geosynchronous satellite always pointing the same spot on the Earth. Since, by assumption, the

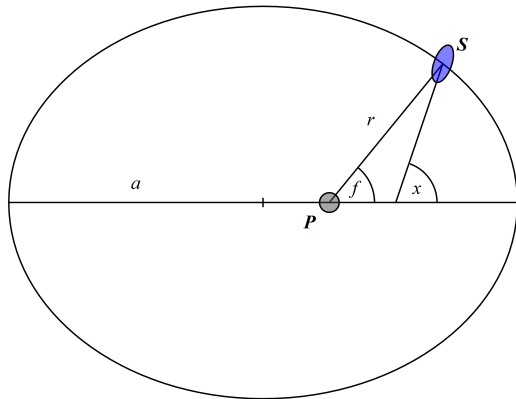


FIGURE 7. The geometry of the spin-orbit model (see the text).

orbit is a Keplerian ellipse, both r and f are known functions of the time and they depend parametrically on the orbital eccentricity e . This implies that the phase-space of the spin-orbit model is 3-dimensional; henceforth the 2-dimensional invariant KAM surfaces provide an important stability property in the sense of confinement in a given region of the phase space. Figure 8 provides some Poincaré maps (at times multiple of 2π) for different values of the parameters. We first analyze a sample which could refer to some geosynchronous satellites, namely with an almost circular orbit $e = 10^{-3}$ and a relatively large oblateness, i.e. a measure of the ratio of the moments of inertia ($\varepsilon = 0.1, 0.4, 0.8$), motivated by the fact that vehicles can be long and thin with antennas always pointing the same spot on the Earth. Comparing these cases we see that the librational region around the synchronous resonance (approximately located at $y = 1$, being $y \equiv \dot{x}$) increases as ε grows. Outside the librational region we find the *rotational invariant tori*, which run the whole interval $[0, 2\pi]$. A reduction of the synchronous libration and a simultaneous increase of the chaotic regions is obtained by taking larger values of the eccentricity like in Figure 8d). The

stability of the librational motion can be shown through the implementation of KAM theory. In fact, being the phase space associated to (11) 3-dimensional, the 2-dimensional invariant rotational tori separate the phase space into invariant regions. In particular, the existence of two rotational surfaces bounding the librational curve from below and above provide the stability of the motion in the phase space region enclosed by these curves. This idea has been implemented in the cases of the restricted 3-body problem and the spin-orbit model ([8]), obtaining stability results for parameter values consistent with the astronomical data. These results are obtained through the application of a (computer-assisted) KAM theorem, which provides also a constructive algorithm to determine the invariant tori. In fact, a rotational KAM surface with frequency ω for (11) is defined as an invariant 2-dimensional torus which is described by the parametric equation

$$x = \theta + u(\theta, t), \quad (12)$$

where θ is a parametric coordinate running in the interval $[0, 2\pi]$, such that $\dot{\theta} = \omega$. The unknown function u must be determined so that (12) is a solution of (11); in particular, if we define the operator D such that $Du = \omega \frac{\partial u}{\partial \theta} + \frac{\partial u}{\partial t}$, then u must satisfy the equation

$$D^2 u(\theta, t) + \varepsilon \left(\frac{a}{r} \right)^3 \sin(2\theta + 2u(\theta, t) - 2f) = 0. \quad (13)$$

KAM theory provides us a tool to solve equation (13) by means of a Newton's method, using the following algorithm:

1. expand the function u in Taylor-Fourier series and define the truncation to a suitable order N , say $u_N(\theta, t)$, as initial approximation:

$$u_N(\theta, t) = \sum_{j=1}^N \varepsilon^j \sum_{m,n \in \mathbb{Z}} \hat{u}_{m,n}^{(j)} e^{i(m\theta+nt)}, \quad (14)$$

for real coefficients $\hat{u}_{m,n}^{(j)}$;

2. insert (14) in (13) and compute recursively the coefficients $\hat{u}_{m,n}^{(j)}$ (notice that the second term in (13) depends on the coefficients of u at the orders 1, ..., $N-1$, so that the equation provides a recursive relation to define u_N);
3. use a Newton's method (as developed in KAM theory, see e.g. [8], [41]) to get a better approximate solution within the limiting precision.

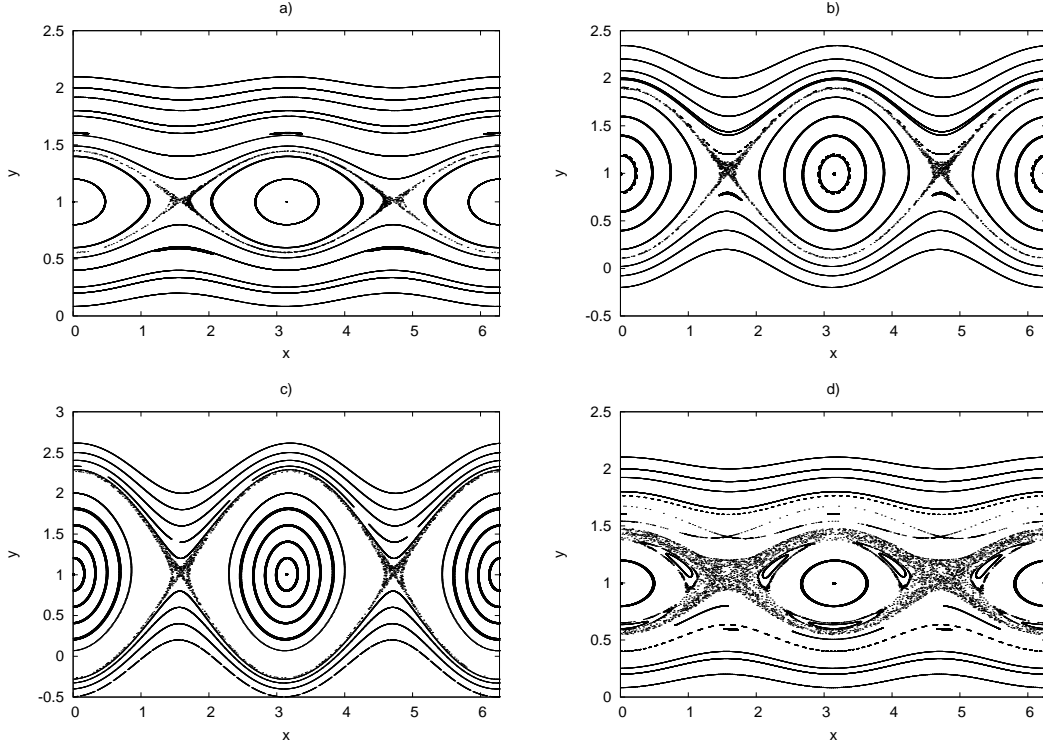


FIGURE 8. Poincaré maps of the spin–orbit model for a) $e = 0.001, \varepsilon = 0.1$, b) $e = 0.001, \varepsilon = 0.4$, c) $0.001, \varepsilon = 0.8$, d) $e = 0.01, \varepsilon = 0.1$.

We remark that such an algorithm can be conveniently implemented on a computer to find the Taylor–Fourier coefficients of the parameterizing function u and that it can be extended to encompass also the construction of stable and unstable manifolds around unstable equilibria ([41], [32]).

6.2 Pitch motion of a non-rigid spacecraft with viscous drag

Spacecraft dynamics is in general affected by external torques which may provoke energy dissipation (compare with [13], [31]). Examples are the Solar radiation pressure, the gravity gradient torque, the effect of an atmosphere, the magnetic torque induced by the planetary’s magnetic field or the torque provoked by a non-rigid structure whenever elastic and/or deformable elements are included in the spacecraft. Following [33] we consider the motion of an asymmetric spacecraft, assuming that the non-rigidity is modeled by a periodic variation of one of the moments of inertia, say $A(t) = A_0 + A_1 \cos \nu t$, where A_0, A_1 are constants

with $A_1 \ll A_0$ and ν is the frequency of variation. In this model we assume that the moments of inertia, say $A > B > C$, define a body frame (O, x, y, z) with O coinciding with the barycenter of the spacecraft (which we assume to keep unaltered by the non-rigid structure). Let us denote by (O, X, Y, Z) the orbital frame with the Z -axis pointing to the planet, the X axis along the direction of the velocity vector and the Y axis perpendicular to the orbit plane; as a first approximation, we assume that the orbit is circular. The Euler angles $(\psi, \vartheta, \varphi)$ between the orbital and body frames are called *yaw*, *pitch*, *roll* angles, respectively ([31]). According to [33] we assume that the yaw and roll motions are initially at rest, say $\psi(0) = \vartheta(0) = 0$ and $\varphi(0) = \dot{\varphi}(0) = 0$, and that the spacecraft orbits in a slightly resisting medium. If the units of measure are chosen so that the orbital frequency of the spacecraft is unity, the equation of motion becomes ([33])

$$\ddot{\vartheta} = -K \sin \vartheta \cos \vartheta - \varepsilon \sin \vartheta \cos \vartheta \cos(\nu t) - \delta \dot{\vartheta}, \quad (15)$$

where $K \equiv 3(A_0 - C)/B$, $\varepsilon \equiv 3A_1/B$ and δ is the viscous constant.

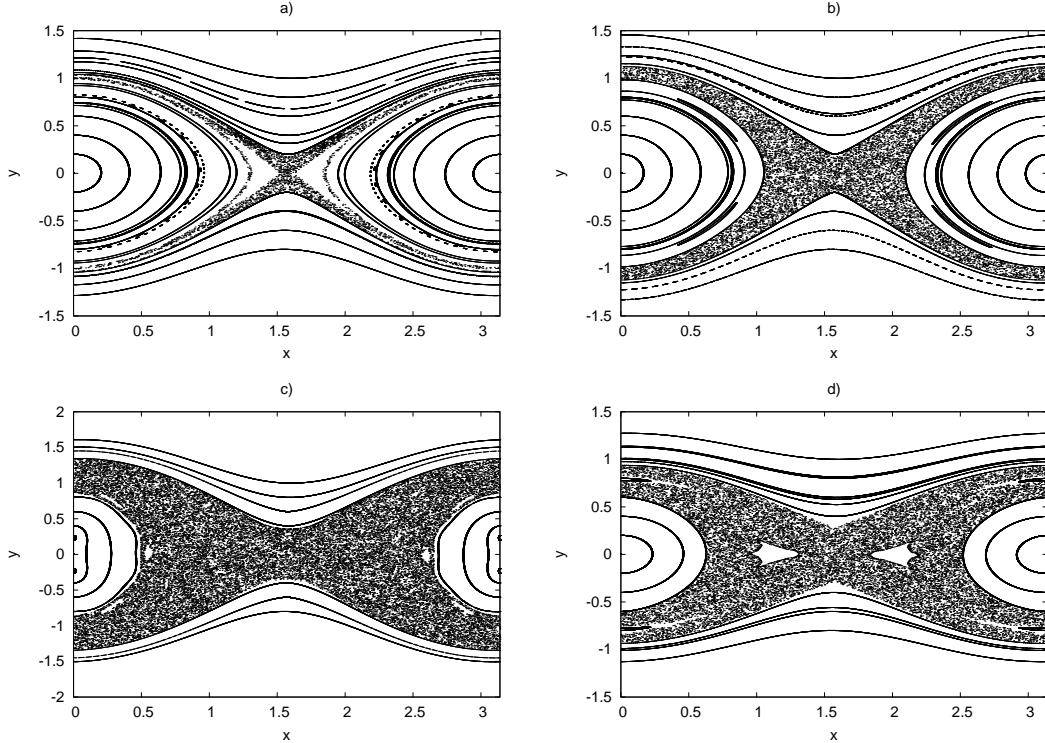


FIGURE 9. Poincaré maps of the pitch model for $\delta = 0$ and a) $K = 1, \eta = 1, \varepsilon = 0.01$, b) $K = 1, \eta = 1, \varepsilon = 0.1$, c) $K = 1, \eta = 1, \varepsilon = 0.5$, d) $K = 0.5, \eta = 1, \varepsilon = 0.1$.

Figure 9 shows some Poincaré maps (at times multiple of 2π) for different values of the parameters; the first three plots fix the values of $K = 1, \eta = 1$, while ε varies, showing an increasing amplitude of the chaotic region as ε gets larger; Figure 9d shows an example where the parameter K has been decreased to $K = 0.5$.

6.3 Stability regions

The Poincaré maps of Sections 6.1 and 6.2 provide a picture of the dynamics for specific values of the parameters. In order to have a global view of the dynamics, one can make use of classical chaos indicators, like the Lyapunov exponents ([6]), which reveal the regular or chaotic character of the dynamics. Strictly related to Lyapunov exponents, an effective indicator of chaos, already used in several contexts of Astrodynamics, is the *Fast Lyapunov Indicator*, hereafter FLI ([24]), which is obtained as the value of the largest Lyapunov exponent at a fixed time. More precisely, let us write the spin-orbit equation (11) or the pitch equation (15) as a first-order differential system of the form $\dot{z} = f(z)$,

where $z \equiv (x, y) \in \mathbb{R}^2$ and f is a 2-dimensional vector function; let the variational equations be written as

$$\dot{v} = \left(\frac{\partial f(z)}{\partial z} \right) v,$$

where v is a 2-dimensional vector. The FLI can be computed as follows: given the initial conditions $z(0) \in \mathbb{R}^2$, $v(0) \in \mathbb{R}^2$, the FLI at time $T \geq 0$ is provided by the expression ([24])

$$\text{FLI}(z(0), v(0), T) \equiv \sup_{0 < t \leq T} \log \|v(t)\|.$$

Figure 10 provides the FLI-maps associated to (11) in the plane ε versus y for $e = 10^{-3}$, $e = 10^{-2}$, $e = 10^{-1}$, respectively; the main features of the dynamics can be captured at a glance, provided we associate to each color a specific behavior: black to purple correspond to periodic orbits and associated librational regions; orange denotes rotational invariant surfaces; yellow corresponds to chaotic dynamics. The results show that for small values of the eccentricity, say $e = 10^{-3}$,

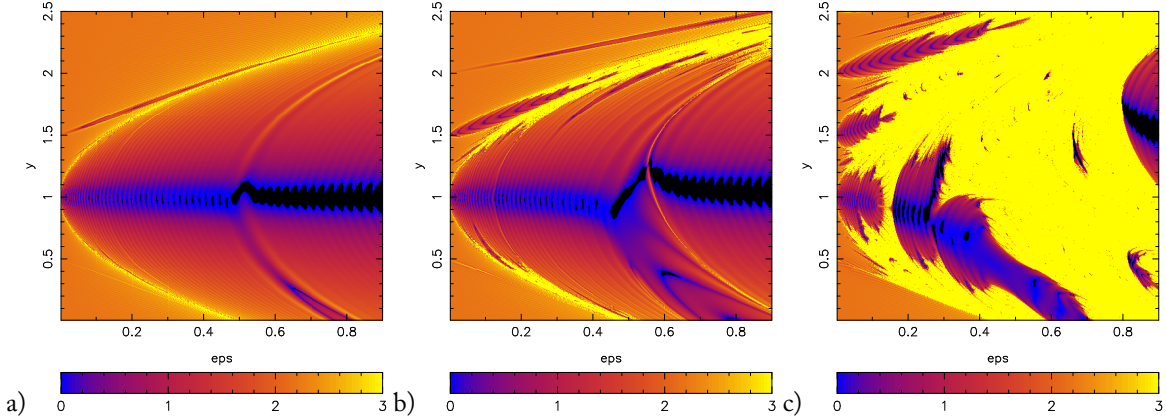


FIGURE 10. Values of the FLI (color scale) of the spin–orbit model showing ϵ versus y for a) $e = 10^{-3}$, b) $e = 10^{-2}$, c) $e = 10^{-1}$.

most of the phase space is filled by KAM tori or by the librational regime around the synchronous resonance (i.e. around $y = 1$); a tiny chaotic zone (the yellow region) surrounds the synchronous resonance, whose librational amplitude gets bigger as the oblateness ϵ increases. As the eccentricity grows, say $e = 10^{-2}$, a region of non-synchronous resonance with frequency equal to $3/2$ (i.e. starting from $y = 1.5$) appears as well as with frequency equal to $2/1$ (i.e. around $y = 2$). For larger eccentricities, say $e = 10^{-1}$, most of the phase space is dominated by chaotic motions.

A similar computation has been performed for the pitch model as in Figure 11; the first two panels refer to the conservative case, while in the last panels a small dissipation ($\delta = 0.001$) has been considered. A comparison between Figure 11a and b shows that the amplitude of the librational region increases with K , while a comparison between Figure 11b and c shows the effect of the dissipation on a time scale up to 150 time units. The system being dissipative, the latter picture is simply a transient dynamic. Indeed, Figure 11d shows the evolution on a time scale three times bigger than that of panel c. Due to the fact that the dissipation is small, one can observe only tiny variations of the dynamical behavior of the solution.

7 Conclusions

The fruitful combination of the concepts of manifolds, chaos and Lagrangian points led to the pioneer work by C. Conley about new routes for mission design. The interaction between Dynamical Systems, Celestial Mechanics and Astrodynamics has revealed many unex-

pected ways to plan space missions and it has opened new perspectives. In fact, the space between the Earth and the Moon as well as that between planets is not dynamically empty, but on the contrary it is definitely crowded by regular stable orbits, unstable manifolds, weakly and strongly chaotic trajectories and escaping orbits. The geography of the phase space has been deeply investigated by using Nekhoroshev's theorem, whose proof contains the interplay between resonant and non-resonant motions. The dynamics on specific invariant manifolds have been established by the celebrated KAM theory, which provides an explicit constructive algorithm to compute the invariant tori as well as the stable and unstable manifolds. The basic ingredient of KAM and Nekhoroshev's theorems is the development of perturbation theories for nearly-integrable systems, which allow to reduce the size of the perturbation to higher orders in the perturbing parameter. The associated normal forms can be computed by means of an adapted manipulator for perturbative series expansions and the results can be used to compute the dynamics of spacecraft within the accuracy of the normal form. These ideas have found a ground-test in many applications concerning the dynamics of natural and artificial celestial bodies, for example, new routes to Moon and planets have been constructed through Space Manifold Dynamics ([27]), the stability of the rotation of dumbbell and tether satellite models have been explored through normal forms ([12], [49]) and the Lagrangian equilibrium points have been used in several spacecraft missions.

Although the theoretical framework is well understood through the consolidated KAM and Nekhoroshev's the-

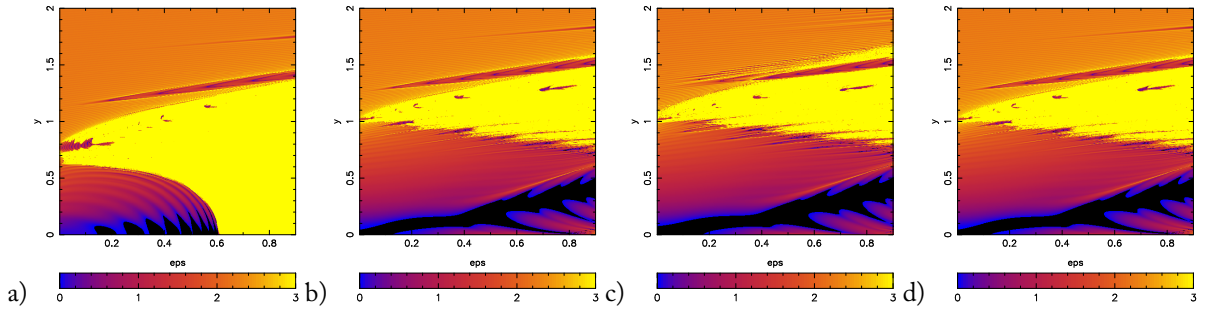


FIGURE 11. Values of the FLI (color scale) of the pitch model showing ε versus y for a) $K = 0.5$, $\eta = 1$, $\delta = 0$, b) $K = 1$, $\eta = 1$, $\delta = 0$, c) $K = 1$, $\eta = 1$, $\delta = 0.001$, $t = 150$, d) $K = 1$, $\eta = 1$, $\delta = 0.001$, $t = 450$.

ories, concrete applications to Astrodynamics still need to be fully exploited. In particular, we point out that the dynamics of spacecraft (as well as that of natural bodies) is affected by dissipative forces (e.g. Yarkowski effect, non-rigidity, gravity gradient torque, etc.). If the strength of the dissipation is small, the dynamics are closely related to that of the conservative model, but on the long run the dissipative effects alter the orbits and affect the dynamics in the sense that the motion is driven toward some attractors (indeed, the dissipation can be conveniently used to modify the spacecraft motion). In this scenario, the dynamics can be studied on different time scales according to mission requirements such as the conservative dynamics, the adiabatic regime and the dissipative setting. These studies can be performed both for orbital and rotational motions, as well as for analyzing the interplay between the two dynamical characters. It is worth mentioning that suitable normal forms can be developed to encompass the dissipative case ([11]). The dissipative normal forms seem very promising to investigate the effect of dissipation and to evaluate the dynamics of the spacecraft with greater accuracy. In conclusion, we believe that the mathematical tools available at present can be conveniently used to investigate and develop new methods in mission design and analysis.

Acknowledgements. We are indebted with Bruce Conway and Leonardo Mazzini for very useful suggestions and remarks. We acknowledge the grants ASI “Studi di Esplorazione del Sistema Solare” and PRIN 2007B3RBEY “Dynamical Systems and Applications” of MIUR.

References

- [1] V. Arnold. Proof of the theorem of A.N. Kolmogorov of the invariance of quasi-periodic motions under small perturbations of the Hamiltonian. *Russ. Math. Surv.*, 18:13–40, 1963.
- [2] R. Bate, D. Mueller, and J. White. *Fundamentals of Astrodynamics*. Dover Publications Inc., 1971.
- [3] A. Bazzani, S. Marmi, and G. Turchetti. Nekhoroshev estimates for isochronous non resonant symplectic maps. *Cel. Mech. Dyn. Astr.*, 47:333–359, 1990.
- [4] E. Belbruno. *Capture dynamics and chaotic motions in Celestial Mechanics*. Princeton University Press, 2004.
- [5] M. Belló, G. Gomez, and J. Masdemont. *Invariant Manifolds, Lagrangian Trajectories and Space Mission Design*. Space Manifold Dynamics, E. Perozzi, S. Ferraz-Mello eds., Springer, 2010.
- [6] G. Benettin, L. Galgani, A. Giorgilli, and J. Strelcyn. Lyapunov characteristic exponents for smooth dynamical systems and for Hamiltonian systems; a method for computing all of them. *Mecanica*, 15:9–20, 1980.
- [7] E. Brown and C. Shook. *Planetary theory*. Cambridge University Press, 1933.
- [8] A. Celletti. *Stability and Chaos in Celestial Mechanics*. Springer-Praxis, XVI, 264 pp., Hardcover ISBN: 978-3-540-85145-5, 2010.
- [9] A. Celletti and L. Chierchia. Quasi-periodic attractors in Celestial Mechanics. *Arch. Rat. Mech. Anal.*, 191:311–345, 2009.

- [10] A. Celletti and A. Giorgilli. On the stability of the Lagrangian points in the spatial restricted problem of three bodies. *Cel. Mech. Dyn. Astr.*, 50:31–58, 1991.
- [11] A. Celletti and C. Lhotka. Stability for exponential times in nearly-Hamiltonian systems: the non-resonant case. *Preprint*, 2011.
- [12] A. Celletti and V. Sidorenko. Some properties of the dumbbell satellite attitude dynamics. *Cel. Mech. Dyn. Astr.*, 101:105–126, 2008.
- [13] A. Celletti, L. Stefanelli, E. Lega, and C. Froeschlé. Global dynamics of the regularized restricted three-body problem with dissipation. *Cel. Mech. Dyn. Astr.*, 109:265–284, 2011.
- [14] C. Conley. Low Energy Transit Orbits in the Restricted Three-Body Problem. *SIAM J. Appl. Math.*, 16:732–746, 1968.
- [15] C. Conley. On the ultimate behavior of orbits with respect to an unstable critical point. I. Oscillating, asymptotic, and capture orbits. *J. Diff. Eq.*, 5:136–158, 1969.
- [16] A. Deprit. Canonical transformations depending on a small parameter. *Cel. Mech. Dyn. Astr.*, 1:12–30, 1969.
- [17] R. Dvorak and R. Schwarz. On the Stability Regions of the Trojan Asteroids. *Cel. Mech. Dyn. Astr.*, 92:19–28, 2005.
- [18] C. Efthymiopoulos, A. Giorgilli, and G. Contopoulos. Nonconvergence of formal integrals: II. Improved estimates for the optimal order of truncation. *J. Phys. A: Math. Gen.*, 37:10831–10858, 2004.
- [19] C. Efthymiopoulos and Z. Sándor. Optimized Nekhoroshev stability estimates for the Trojan asteroids with a symplectic mapping model of co-orbital motion. *MNRAS*, 3646:253–271, 2005.
- [20] S. Eggli. Refinement of Near Earth Asteroids' orbital elements via simultaneous measurements by two observers. *Cel. Mech. Dyn. Astr.*, 109:211–228, 2010.
- [21] B. Érdi. The Trojan problem. *Cel. Mech. Dyn. Astr.*, 65:149–164, 1996.
- [22] F. Fassò, M. Guzzo, and G. Benettin. Nekhoroshev-Stability of Elliptic Equilibria of Hamiltonian Systems. *Comm. Math. Phys.*, 197:347–360, 1998.
- [23] S. Ferraz-Mello. *Canonical Perturbation Theories*. Springer-Verlag, 2007.
- [24] C. Froeschlé, E. Lega, and R. Gonczi. Fast Lyapunov indicators. Application to asteroidal motion. *Cel. Mech. Dyn. Astr.*, 67:41–62, 1997.
- [25] A. Giorgilli. Rigorous results on the power expansions for the integrals of a Hamiltonian system near an elliptic equilibrium point. *Ann. Inst. H. Poincaré*, 48:423–439, 1988.
- [26] A. Giorgilli. Effective stability in Hamiltonian systems in the light of Nekhoroshev's theorem. *Integrable Systems and Applications*, Springer-Verlag, Berlin, New York:142–153, 1989.
- [27] G. Gomez and E. Barrabés. *Space Manifold Dynamics*. Available at http://www.scholarpedia.org/article/Space_Manifold_dynamics, 2010.
- [28] G. Gomez, J. Masdemont, and C. Simó. Study of the transfer from the Earth to a Halo Orbit around the equilibrium point L1. *Cel. Mech. Dyn. Astr.*, 56:541–562, 1997.
- [29] M. Guzzo, F. Fassò, and G. Benettin. On the stability of Elliptic Equilibria. *Math. Phys. Electron. J.*, 4:16 pp., 1998.
- [30] J. Hadjidemetriou. Mapping models for Hamiltonian systems with application to resonant asteroid motion. In “Predictability, Stability and Chaos in N-Body Dynamical Systems”, A.E. Roy ed., *NATO ASI Ser. B, Phys.*, 272:157–175, 1991.
- [31] P. Hughes. *Spacecraft Attitude Dynamics*. Wiley, New York, 1998.
- [32] G. Huguet, R. de la Llave, and Y. Sire. Fast numerical algorithms for the computation of invariant tori in Hamiltonian systems. *Preprint, to appear in DCDS-A*, 2011.
- [33] M. Inarrea and V. Lanchares. Chaotic pitch motion of an asymmetric non-rigid spacecraft with viscous drag in circular orbit. *Int. J. Nonlin. Mech.*, 41:86–100, 2006.

- [34] A. Kolmogorov. On the conservation of conditionally periodic motions under small perturbation of the Hamiltonian. *Dokl. Akad. Nauk. SSR*, 98:527–530, 1954.
- [35] W. Koon, M. Lo, J. Marsden, and S. Ross. Low energy transfer to the Moon. *Cel. Mech. Dyn. Astr.*, 81:63–73, 2001.
- [36] W. Koon, M. Lo, J. Marsden, and S. Ross. *Dynamical Systems, the Three-Body Problem and Space Mission Design*. Marsden Books., available at <http://www.esm.vt.edu/~sdross/books/>, 2008.
- [37] J. Lagrange. *Mécanique Analytique (1787)*. Œuvres de Lagrange, Joseph-Alfred Serret, Paris, vol. 11–12 (first published in 1787), 1867.
- [38] C. Lhotka, C. Efthymiopoulos, and R. Dvorak. Nekhoroshev stability at L4 or L5 in the elliptic-restricted three-body problem - application to Trojan asteroids. *Mont. Not. Roy. Astr. Soc.*, 3843:1165–1177, 2008.
- [39] J. Littlewood. On the equilateral configuration in the restricted problem of three bodies. *Proc. London. Math. Soc.*, 9:343–372, 1959.
- [40] J. Littlewood. The Lagrange configuration in celestial mechanics. *Proc. London. Math. Soc.*, 9:525–543, 1959.
- [41] R. d. l. Llave, A. Gonzalez, A. Jorba, and J. Villanueva. KAM theory without action-angle variables. *Nonlinearity*, 18:855–895, 2005.
- [42] J. K. Miller and E. A. Belbruno. A Method for the Construction of a Lunar Transfer Trajectory Using Ballistic Capture. *Proceedings of the 1st AAS/AIAA Spaceflight Mechanics Meeting*, Paper No. A93-17901 05-13:97–109, 1991.
- [43] J. Moser. Stabilitätsverhalten kanonischer Differentialgleichungssysteme. *Nachr. Akad. Wiss. Goett. Math. Phys. Kl. IIa*, 6:87–120, 1955.
- [44] J. Moser. On the generalization of a theorem of A. Liapounoff. *Comm. Pure Appl. Math.*, 11:257–271, 1958.
- [45] J. Moser. On invariant curves of area-preserving mappings of an annulus. *Nach. Akad. Wiss. Göttingen, Math. Phys. Kl. II*, 1:1–20, 1962.
- [46] N. Nekhoroshev. Exponential estimates of the stability time of near-integrable Hamiltonian systems. *Russ. Math. Surv.*, 32:1–65, 1977.
- [47] N. Nekhoroshev. Exponential estimates of the stability time of near-integrable Hamiltonian systems 2. *Trudy Sem. Petrov.*, 5:5–50, 1979.
- [48] H. Poincaré. *Les Méthodes Nouvelles de la Méchanique Céleste*. Gauthier Villars, Paris, 1892.
- [49] V. Sidorenko and A. Celletti. A "spring-mass" model of tethered satellite systems: properties of planar periodic motions. *Cel. Mech. Dyn. Astr.*, 107:209–231, 2010.
- [50] V. Szebehely. *Theory of Orbits, The Restricted Three Body Problem*. Academic Press, 1967.



Epitaxial quantum dots for sunlight harvesting

D. ALONSO-ÁLVAREZ*, B. ALÉN AND J. M. RIPALDA

IMM-Instituto de Microelectrónica de Madrid (CNM-CSIC), Isaac Newton 8, 28760 Tres Cantos, Spain

Abstract. As the photovoltaic market grows, there is an increasing necessity for improving solar cell technologies beyond their current limitations. One of the suggested ways to achieve that improvement is through the use of epitaxial quantum dots and the intermediate band solar cell concept. In this work, we present an overview of this technology, from the fundamentals of the concept to its practical implementation with quantum dots (QD) including its current status of development.

1 Introduction

1.1 Photovoltaics: from satellites to the rooftops

From the beginning of the space exploration with the Vanguard I and its 9% efficient Si solar cells in 1958 to the state of the art 32% efficient triple junction (3J) solar cells, space industry has always utilized the solar energy harvesting to power spaceships and satellites. In 1998, the Deep Space 1 spacecraft relied completely on its solar array to power the experimental ion engine and test many other advanced technologies. The International Space Station, currently orbiting the Earth with six people aboard, gets all of its energy from eight solar arrays of 420 m² each. And even the most challenging plans for building bases on the surface of the Moon and Mars take the solar energy as the fundamental building block of their installations.

From space, sunlight harvesting came down to Earth and it has become a competitive alternative in the last years as a non polluting, endless source of energy. Not surprisingly, the market of solar photovoltaic systems for terrestrial applications has grown at an annual average rate of 60% from 2004 to 2009 [32].

The increasing relevance of solar photovoltaic energy highlights the importance of searching for new ways of further improving the efficiencies and performance of current technologies. At the moment, the most advanced solar cells are triple junction devices made of III-V semiconductor compounds grown on Ge substrates, with a maximum efficiency of 32% and achieving a peak efficiency of 41.6% when using concentrated light [11]. These highly efficient solar cells are, in general, not cost effective unless used under concentrated light or used in space applications. As a consequence of this, the market for terrestrial systems is still dominated by Si solar arrays with efficiencies of around 20%. [11]

1.2 The intermediate band solar cell

The intermediate band solar cell (IBSC) concept was originally introduced by Wolf in the early 60's. However, it gained its current importance only after the work of Luque and Martí in 1997 that updated the concept in terms of detailed balance calculations. [37, 18]

The IBSC is based on the existence of a band partly filled with electrons inside the bandgap of a host material which can absorb low energy photons that otherwise

*E-mail address: diego.alonso@imm.cnm.csic.es

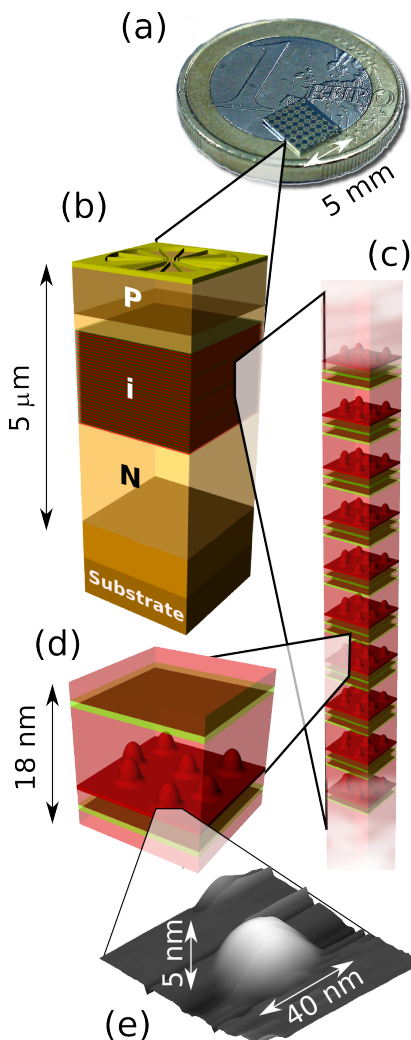


FIGURE 1. Illustration of the scale relationship in new concept solar cells: (a) a normal size QD solar cell, (b) the layer structure of the device, (c) the QDs stack, (d) the basic building block of QDs + spacer and (e) a single QD.

would be lost. Figure 2 summarizes the process. The absorption of photons with energies above the bandgap of the host material is mostly due to the interband transitions (A), from the valence band to the conduction band ($\text{VB} \rightarrow \text{CB}$). Transition B takes place between the valence band and empty states in the intermediate band ($\text{VB} \rightarrow \text{IB}$). Finally, transition C promotes an electron in the intermediate band to the conduction band ($\text{IB} \rightarrow \text{CB}$).

According to the calculations, an IBSC optimally designed can achieve conversion efficiencies that exceed

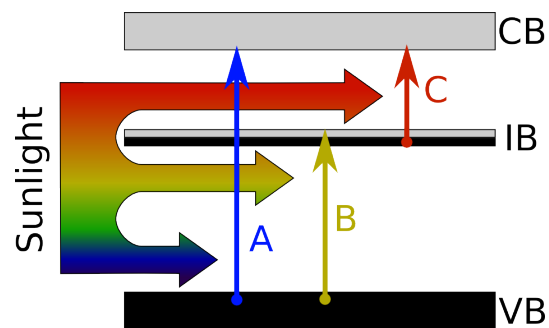


FIGURE 2. Intermediate band material and the electronic transitions involved in the generation of two electron-hole pairs.

the Shockley-Queisser limit for an ideal single gap solar cell and is near to the efficiency of an ideal series connected 3J cell under full concentration [22]. The advantage of this technology is that it can be used as a supplement in a multijunction device, giving an overall efficiency larger than that of a 3J or an IBSC separately. There are several material systems that can, in principle, form the intermediate band in a semiconductor. For example, there are studies that predict the formation of this band in a Si crystal highly doped with Ti [9]. Chalcopyrite compounds and thiospinels partially substituted with transition metals can also lead to the same kind of intermediate band [28, 29]. But probably the approach that has received more attention is using nanotechnology to create the intermediate band. This is where quantum dots come into play.

1.3 Quantum dots

When the size of a semiconductor is reduced in one or more dimensions to only a few tens of nanometres, the characteristics of the material change and quantum confinement effects begin to rule its electronic and optical properties. Among many other extraordinary consequences, its density of states (which sets the available energies that electrons and holes can have inside the semiconductor nanostructure) becomes stepped in 2D nanostructures, spiky in 1D and finally it is completely reduced to few discrete energy levels once the confinement is in the three dimensions (0D nanostructure). In the latter situation we talk about quantum dots (figure 3). It is worth emphasising that the density of states presented are somewhat idealised. Typical size distributions in QDs rarely result in atomic like transitions as shown.

Due to their discrete energy levels, QDs are sometimes called artificial atoms and, opposite to real atoms, their energy levels can be tuned to a particular value simply by changing their size, shape, composition or the surrounding host material.

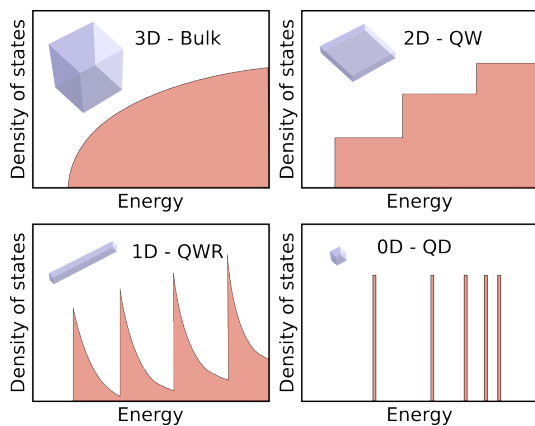


FIGURE 3. Density of states for a bulk semiconductor and nanostructures with confinement in one, two and three dimensions (quantum well -QW-, wire -QWR- and dot -QD-.)

QDs have a wide range of applications. Ultra low threshold current lasers have been fabricated at the telecommunication wavelengths that make use of the ground state emission of QDs [24]. They have already shown very promising characteristics as mid and far infrared photodetectors [17]. They are also the best candidates to fabricate single photon sources and quantum gates for semiconductor based quantum optical information technologies [23, 16]. Finally, in the last few years, they have attracted much attention in the photovoltaic field as the active material in new concept solar cells.

At this point it is important to distinguish between two kind of QDs that lead to different realizations of new generation solar cells. On one hand, there are epitaxial quantum dots which are those used in lasers and quantum information, typically made of InAs, GaAs or InSb embedded in a higher bandgap material (GaAs, AlGaAs, InP...). These QDs have been suggested as the active material for the fabrication of intermediate band solar cells (IBSC) [21].

On the other hand, colloidal QDs made of lead selenide (PbSe) or cadmium telluride (CdTe) for example, have proven very effective in exploiting the multiple exciton generation (MEG) process. In MEG solar cells, high energy photons produce several electron-hole pairs in-

stead of only one, thus avoiding losing the energy in excess in the form of heat.[14]

Both concepts can achieve comparable conversion efficiencies from a theoretical point of view, however, the former can be more easily integrated in current III-V solar cells technology since the materials and the production process are, essentially, the same.

2 The quantum dot solar cell

In this section we introduce fundamental concepts related to the design of a QD-IBSC from a theoretical point of view, the characteristics of the intermediate band material and the assumptions made for it to work.

2.1 Fundamentals of the intermediate band

In the original work by Luque and Martí they established several conditions that the intermediate band solar cell must fulfil, which can be summarized in the following [18, 38]:

1. Only optical transitions are permitted between the three bands depicted in figure 2; non-radiative processes must be avoided (thermal or tunnel escape, phonon emission and absorption, Auger processes...).
2. The optical transitions must be allowed and be efficient.
3. There should be no overlap between the absorption coefficients, which means that if a photon can produce the transition A or B, it will not be efficient in producing the transition B or C, respectively.
4. The position of the IB inside the bandgap, and the bandgap itself, should be such that the energies of transitions A (E_A), B (E_B) and C (E_C) approach the optimum calculated values for the ideal case: $E_A \sim 2.1$ eV, $E_B \sim 1.2$ eV and $E_C \sim 0.7$ eV. This configuration gives the highest efficiency.

The first condition avoids the drop in the open circuit voltage (voltage preservation principle) and implies the existence of three independent quasi-Fermi levels. The other three conditions maximize the photocurrent produced by the solar cell.

Under the previous assumptions, the conversion efficiency limit of an IBSC simulating the Sun as a black body at 6000 K and full concentration ($\times 46050$) is

63.2%. As a comparison, the efficiency limit in the same conditions of a single, double and a triple junction solar cells are 40.8%, 55.7% and 63.8% respectively.[22]

2.2 How QDs create the IB

In its simplest form, a QD-IBSC is a P-i-N diode with several layers of QDs placed in the intrinsic region (i), as it can be seen in figures 1b and 4 [21]. The IB material is limited to only one region, electrically isolated from the N and P contacts.

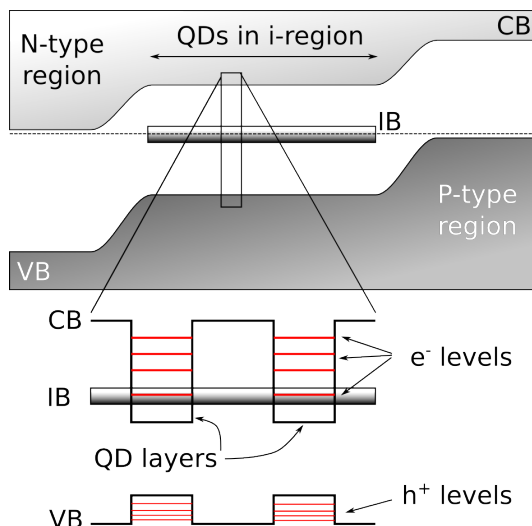


FIGURE 4. Band diagram of a simple IBSC. The IB is formed from the electron ground states of the stacked QD layers.

In this configuration, the IB arises from the confined electron energy levels in the QDs which, due to the 3D confinement, are isolated between them and with the conduction band (figure 4). This is one of the reasons that makes QDs preferable to QWs and QWRs: in these nanostructures there is no isolation between the confined levels and the conduction band, but a continuum of states, as it can be seen in figure 3. In this situation, a fast thermal relaxation and excitation between the CB and the confined levels would take place, violating the condition 1 set in the previous section.

In order to work as an IB and to have strong transitions B and C, the ground level have to be half filled with electrons so, in general, the intrinsic region is lightly doped to reach the required carrier concentration. This is a second reason why QWs are not good candidates to form the intermediate band: transition C is forbidden for incident light perpendicular to the QW plane, regardless

of the doping level, so condition 2 would never be fulfilled [33].

In general condition 3 is always satisfied since the transition probability depends on the density of states and the wavefunction overlap of the initial and final states, which have the appropriate dependency on photon energy.

Finally, the degree of fulfilment of condition 4 is limited by the range of materials available and the possibility of making QDs with them. There are several works that predict the optimum materials to achieve this goal, but, as a matter of fact, most groups work with the system InAs/GaAs: there is a long tradition of growing InAs QDs on GaAs substrates and there are many experimental and theoretical studies about its properties [6]. If achieved, the ideal InAs/GaAs IBSC could substitute the middle cell in a 3J device, increasing its limiting efficiency, although as a stand alone device this system is not optimum, as it will be shown below.

3 The QD stack

A complete working solar cell is far more complicated than the simple P-i-N junction depicted in figures 1 and 4. However, in a QD solar cell it is the active material, the QDs, which deserves most of the attention. Although in the last few years the advances in this field have been very noticeable, there are still some issues that prevent this new concept to surpass the efficiency of a conventional solar cell [5, 30, 3]. In this section, we describe the process of fabricating a stack of InAs QDs for photovoltaic applications, the problems that may appear, and the techniques and modifications to the original design used to mitigate those problems.

3.1 A single QD layer

To fabricate our samples we use solid source molecular beam epitaxy (MBE) which allows a very precise control of the growth conditions (substrate temperature, gas pressures, growth rates...) in addition to several *in situ* characterization methods. With this technique, it is possible to control the composition of the samples to the limit of a fraction of an atomic monolayer (ML). Epitaxial self assembled QDs appear when a semiconductor material grows on top of a substrate with a smaller lattice parameter. This is a very unstable situation and, due to the accumulation of elastic energy, after a critical thickness the growth front tends to relax and ripple (figure 5). Those ripples are the quan-

tum nanostructures. Depending on their shape they are called quantum wires (if they form long strips along a preferential direction), quantum dots (if they are dome-like structures) or even more exotic shapes (quantum rings, quantum dashes...) [1, 10]. Each of them possesses its own particular optical and electrical properties, as stated above, making them suitable for one or other application.

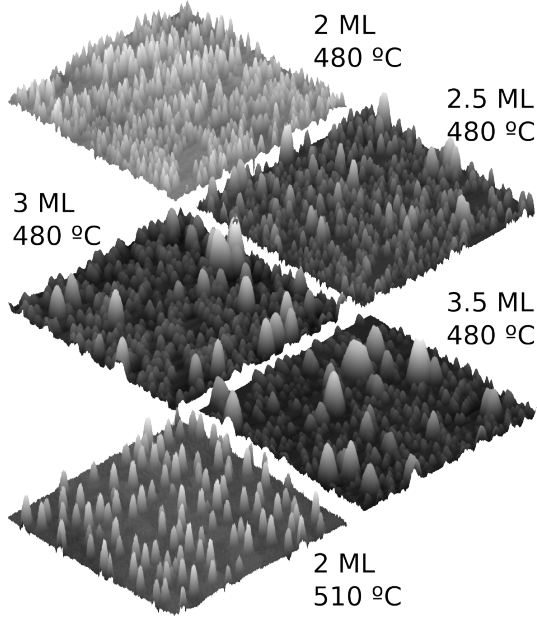


FIGURE 5. Atomic force microscopy images of QDs growth under different conditions. Each image is $1 \times 1 \mu\text{m}$ and the color scale goes from 0 nm (black) to 4, 19, 22, 29 and 10 nm (white) respectively from top to bottom.

Our best QDs form after the growth of 2 ML of InAs on a GaAs (001) substrate. Under the conditions used, the resulting nanostructures are lens-shaped QDs around 5 nm height and 40 nm in diameter (figure 5, bottom image, figure 1e). Different growth conditions lead to different density, homogeneity and size of the QDs which, in turn, affect the position of the energy levels.

In figure 6, it can be seen the qualitative evolution of the position of the energy levels within the bandgap of the host material as a function of the QDs size (normally their height, which is the smallest dimension). As the size of the QDs is increased, more energy levels are available and they get closer to each other and to the QDs band edge. As it will be seen below, the desirable situation would be (d) in figure 6, only one electron level with the first excited state close to the conduction band,

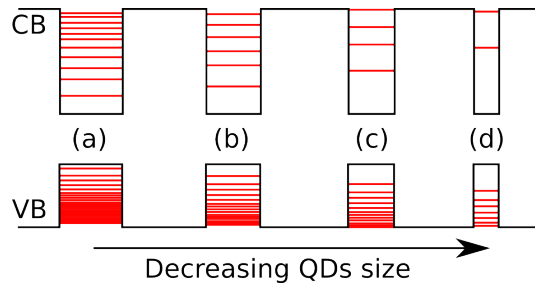


FIGURE 6. Schematic representation of the energy levels in a QD of different sizes.

although most QDs exhibit a level diagram closer to (c) or even (b).

Although it is not a requirement of the IBSC, in general it is desirable to have a good size homogeneity and to avoid large QDs since they tend to produce dislocations and bad quality materials. They are also more difficult to reproduce which is a necessity in a technology that aims to be implemented in industry. Referring to figure 5, QDs of images top and bottom would be acceptable to produce a device, but not the other three.

3.2 Many QDs layers: strain balanced stacks

Once the properties of a single QDs layer are established, it is time to stack them in a structure of several layers. The reason for this is the small active volume they represent and, hence, their small absorption cross section.

In solar cells (or infrared photodetectors) we find a serious dilemma; if we need to stack many layers of QDs, the strain and the elastic energy accumulates from layer to layer and the quality of the material degrades rapidly. We can separate the QDs layers and leave the extra energy dilute in the spacer between them, but in this case, the large total thickness of the device might make the extraction of carriers inefficient, in addition to problems related to the longer growth times of the samples. For this reason, in applications where a large number of QDs layers are needed, the general tendency is to keep the spacers within relatively small values (10-20 nm) and to use the strain balanced technique to dispose of the strain.

Strain balanced (or strain symmetrization, as it is also known) was introduced by Ekins-Daukes *et al.* in 1999 as a way to increase the number and quality of InGaAs QWs in a solar cell [8]. The technique worked fairly well and an InGaAs/GaAsP multiple quantum

well solar cell delivered by QuantaSol has reached an efficiency close to the world record for a single junction device (28.3% compared to 28.8%) at larger concentration [11, 31]. The technique was immediately exported to other nanostructures, in particular, to QDs, and efforts along these lines have been very intense in the last years.

The strain balanced (SB) technique consists of compensating the compressive stress introduced by the QDs by a tensile stress in the spacer between layers. In this way, by alternating tensile-compressive regions, the strain in the material does not accumulate and the formation of dislocations and other defects is suppressed.

Several groups have implemented their own combinations of materials in an attempt to stack many layers of QDs. Nuntawong *et al.* demonstrated improved optical quality in a stack of InAs QDs on GaAs using Ga(In)P as a compensating layer for laser applications [25]. Bailey *et al.* used pure GaP as a compensating layer in a 10-folded stack of InAs QDs, however, Popescu *et al.* preferred GaAsP, stacking up to 50 InGaAs QDs layers on a GaAs (113) substrate [5, 30]. Finally, Oshima *et al.* used Ga(N)As very successfully as a compensating layer, in spite of the problem of reducing the bandgap of the host material [27]. In all cases, they found improved crystal quality and optical properties although the overall performance of the devices as solar cells were not as good as a reference solar cell without QDs.

Our group has used two different approaches to achieve the strain symmetrization. First we used a digital strain compensation of InAs QDs with two separated GaP monolayers using a total spacer of 18 nm [3]. We manage to grow 50 QDs layers with good quality from a structural and optical point of view. However, the response of the solar cell in the high energy region was very bad, which we attributed to a severe degradation of the emitter of the device (P-region). X-ray diffraction measurements threw a degree of compensation of only 40%, which might be responsible of the poor results in the efficiency measurements.

Second, in order to achieve a perfect strain compensation we characterized the growth of the samples by *in situ* controlling the total accumulated stress [2]. This powerful technique allows to monitor the accumulated compressive stress introduced by a QD layer and the tensile stress due to the growth of the compensating layer (GaAsP of different compositions, in our case). The parameters of the latter (thickness, composition...) can then be chosen so the total accumulated stress per building block (QDs + spacer + compensating layer) ap-

proaches zero (figure 7).

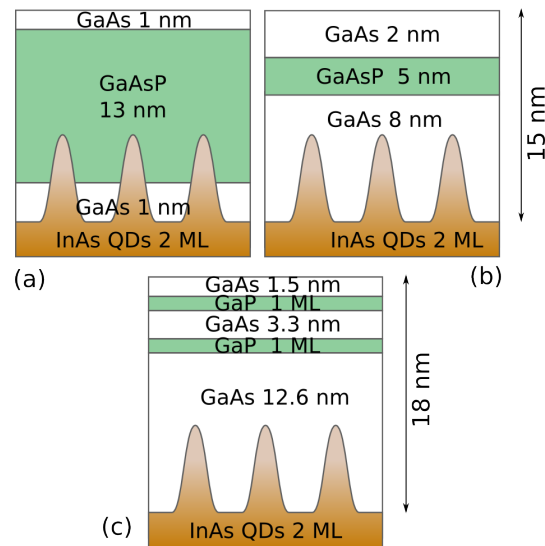


FIGURE 7. Strain balanced building blocks used in the devices of references [2] (a and b) and [3] (c).

We observed that after the growth of several strain balanced QDs layers, the stack degraded even under a zero stress condition. The reason for this degradation might be related with the QDs 3D shape that generates an inhomogeneous strain field around them. This strain field, responsible for the vertical alignment commonly observed in QDs stacks, can affect the formation of the strain balanced layer on a local scale, enhancing composition modulation processes, and thus preventing, or making worse, the correct strain symmetrization of the QDs layers.

Tatebayashi *et al.* have addressed this problem of inhomogeneous strain fields in stacks of strain balanced quantum dots studying the reduction in the degree of correlation between the QDs layers when they are correctly compensated for [35]. Bailey *et al.* also included the QDs shape in the problem, using an effective thickness of InAs to calculate the optimum compensating layer thickness [5]. In both cases, a perfect compensation was achieved on average using GaP, accepting that there would be regions over and undercompensated. No effect of the strain fields in the compensating layer was included into their studies or observed experimentally. Taking all this information into account, it seems that the most favorable situation is, precisely, to use pure GaP layers as the compensating material [35, 5, 3]. Being a binary alloy, it cannot suffer from composition

modulation, a general problem of ternary or quaternary compounds that is enhanced by the presence of the inhomogeneous strain field. Additionally, the thickness of the compensating layer can be kept thin enough (2 - 5 ML) so no transport detriment is expected. The use of other materials is also possible, as it has been reported, however, off-cut or high index substrates, very small QDs or larger spacers seems to be needed [30, 27]. In general these studies indicate that, on the contrary to strain balanced QWs, in QDs it is not enough to achieve a zero stress condition *on average*. Other factors, such as the compensating layer composition (binary or ternary alloy) and its position inside the spacer, gain importance, which had previously been disregarded until now.

3.3 The carrier extraction problem

Another point to be considered in the design of a stack of QDs for the implementation of the IBSC is the problem of non-radiative extraction of carriers from the intermediate band.

In general, it is taken as a positive sign in QDs solar cells to have strong photocurrent (PC) below the bandgap of the host material (GaAs in most cases) [30, 3, 27]. This means that the absorption of photons by the QDs and the extraction of carriers are very efficient. However, as pointed out by Antolín *et al.*, this might be a mistake in the case of an IBSC [4]. In particular, if this PC has its origin in thermal or tunnel escape of carriers from the QDs, the voltage preservation principle stated in section 2.1 is not fulfilled and the solar cells do not show the expected superior performance.

Antolín describes two mechanisms as responsible for voltage drop in QD solar cells. On one hand, there is thermally activated escape of electrons from the QDs, directly or assisted by the excited states (figure 8 (i) and (ii), respectively). On the other, electrons might tunnel to excited states of QDs placed in adjacent layers (figure 8 (iii)). They show that the former can be partly avoided by increasing the energy of confinement of electrons (termed E_C previously). They suggest to use strain relieving layers of higher bandgap materials around the QDs, such as InAlGaAs, to increase the depth of the ground electron level at the same time that an effective reduction of the bandgap of the host material is avoided. Tunneling may be also prevented, increasing E_C and separating the QDs layers, making the transition to an adjacent sheet inefficient. A possible drawback of this approach is that it might lead to the problems stated in the previous section when using large spacers between

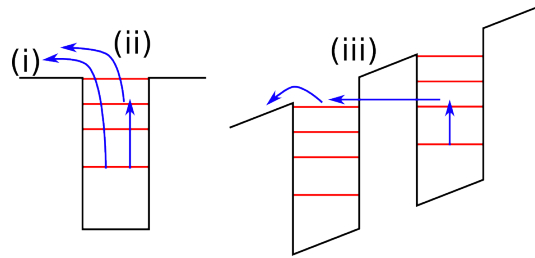


FIGURE 8. Escape processes that reduce the open circuit voltage. Thermal escape (i) direct and (ii) assisted by excited states. (iii) Thermal assisted tunnel.

QDs layers, so a trade-off between both effects should be consider to get an optimum design.

Closely related to the non-radiative escape from the QDs is the non-radiative capture of carriers from the CB to the IB. It has been shown that the capture of electrons by a QD is dominated by fast emission of phonons or by an Auger process, not by the emission of a photon [26]. Again, these mechanisms are a source of losses that, currently, are not clear how to avoid.

In spite of the problems described in the previous paragraphs, generation of PC due to the absorption of mid and far infrared photons from the IB to the CB have already been observed in an IBSC [20]. This contribution was around three orders of magnitude weaker than other effects, but it served to illustrate the working principles of the device. There are already some works that study how to improve the strength of this transition [19].

3.4 Spectral matching

Finally, the last consideration is related with the absorption spectrum of the QDs solar cell and the emission spectrum of the Sun. Figure 9a shows the spectral energy density of the Sun simulated as a black body at 6000 K and the ideal absorption coefficients according to the IBSC theory. Figure 9b, on the other hand, shows more realistic absorption coefficients as approximately deduced from the literature of InAs QDs solar cells and InAs quantum dot infrared photodetectors (QDIP) [3, 17]. In both cases the absorption coefficients are normalized to unity.

As it can be seen, although the high energy transitions might be acceptable for an IBSC, there is a critical difference in the lowest energy transition. In the InAs/GaAs QDs system this absorption is located in a region where the spectral energy density of the Sun is extremely low (three orders of magnitude smaller than

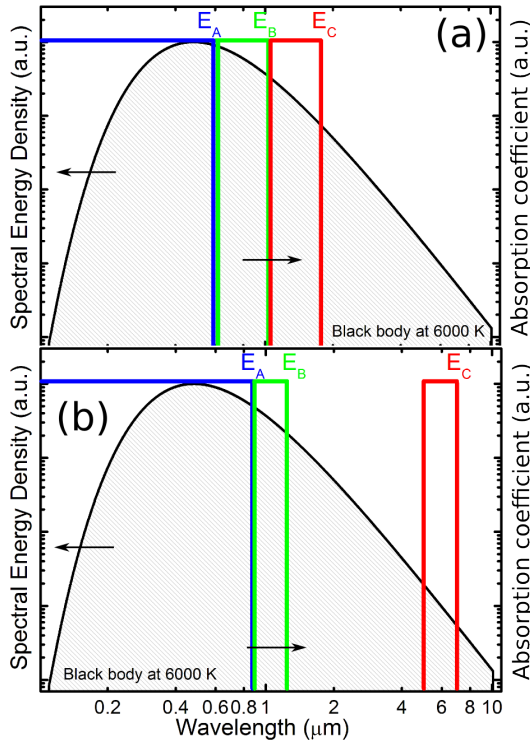


FIGURE 9. Spectral energy density of the Sun and the (a) ideal and (b) realistic normalized absorption coefficients.

the maximum), with no continuity between this absorption range and the other two. As a consequence photons with intermediate energies would be lost and the QD-IBSC will not show any improvement compared to a normal device. Moreover, combining this effect with the other two problems explained in the previous section, the InAs/GaAs IBSC will probably not outperform a reference GaAs device.

The origin of this effect is two folded. On one hand, the theoretical work of Luque has shown that only transitions between confined states with adjacent quantum numbers are strong [19]. This means that photons with energies larger than the energy difference between those levels will not produce a transition between the IB and the CB. On the other hand, the energy gaps and the conduction band offset in the InAs/GaAs system are not optimum and do not allow a better tuning of the transition energies if the previous selection rule is to be fulfilled.

The only solution to solve this mismatch between the absorption spectrum and the spectral energy density of the Sun seems to be to change the material sys-

tem to another one with more appropriate band offsets [30]. Some of the suggestions are InPSb/GaAsSb or InAsP/AlInAs [15]. Although there are some theoretical works addressing this problem, the experimental results with alternatives to the InAs/GaAs QDs are very limited and do not completely fulfil the required design constraints [36]. In this aspect a major experimental work is needed to test the feasibility of the theoretical predictions for materials systems that can lead to the IBSC.

4 Current status of the concept

QD solar cells have been grown by several research groups over the last couple of years. The reduction in the open circuit voltage is reasonably small and there is an appreciable increase in the short circuit current. However, the best results currently use a tailoring of the absorption edge of the host material rather than the IBSC concept and the fabrication of fully working devices is still in a very early stage of development. Typical current voltage curves and external quantum efficiency measurements of QDs solar cell can be found in the references of Table 1, where there is a comparison of some of the last results in this field. The table includes a summary of the materials used, the number of QDs layers (n), if they use strain balancing (SB), the short circuit current (I_{SC}), the open circuit voltage (V_{OC}), the fill factor (FF) and the efficiency (η).

As it can be seen, the general trends are to use a reduced number of QDs layers and to disregard the use of strain balance. Although QDs solar cells with more layers have been fabricated, it is found that the increase in the short circuit current does not compensate for the reduction in the open circuit voltage, leading to an overall efficiency smaller than solar cells with only few QD layers [34]. Non-radiative capture and emission of carriers by the QDs and the lack of spectral matching are the most important sources of losses in all these cells and, currently, they represent the main bottleneck in the development of QD-IBSC.

Considerable efforts are being devoted to overcome these limitations and fulfil the roadmap for QD-IBSC. Compared to the data available only one decade ago, now more QDs can be stacked with improved material quality, the key working principles have been illustrated and the fundamental processes governing the dynamics of solar cells with quantum nanostructures are better

[Ref]	Year	QD/Barrier	n	SB	I_{SC} (mA cm $^{-2}$)	V_{OC} (V)	FF (%)	η (%)
[7]	2009	InGaAs/GaAs	10	No	27.7 (27.4)	0.84 (1.04)	79.2 (83.4)	18.3 (23.8)
[12]	2010	InAs/GaAs	5	No	18.5 (18.4)	0.87 (0.91)	81.4 (81.3)	13.1 (13.0)
[13]	2009	InAs/GaAs	10	Yes	17.8 (16.5)	0.91 (1.00)	81 (81)	13.1 (13.4)

TABLE I. Comparison of the current best results of QDs solar cells. Values in brackets correspond to reference devices without QDs.

understood. In the years to come, the intense research in this field should reveal the real potential of epitaxial QDs in photovoltaics.

References

- [1] B. Alén, J. Martínez-Pastor, L. González, J. García, S. Molina, A. Ponce, and R. García. Size-filtering effects by stacking InAs/InP (001) self-assembled quantum wires into multilayers. *Physical Review B*, 65(24):1–4, 2002.
- [2] D. Alonso-Álvarez, J. M. Ripalda, B. Alén, A. Rivera, A. G. Taboada, J. M. Llorens, Y. González, L. González, and F. Briones. Strain issues in stress compensated QDs for intermediate band solar cells. In *Proceedings 25th European Photovoltaic Solar Energy Conference and Exhibition*, 2010.
- [3] D. Alonso-Álvarez, A. G. Taboada, J. M. Ripalda, B. Alén, Y. González, L. González, J. M. García, F. Briones, A. Martí, A. Luque, A. M. Sánchez, and S. I. Molina. Carrier recombination effects in strain compensated quantum dot stacks embedded in solar cells. *Applied Physics Letters*, 93(12):123114, 2008.
- [4] E. Antolín, A. Martí, C. D. Farmer, P. G. Linares, E. Hernández, A. M. Sánchez, T. Ben, S. I. Molina, C. R. Stanley, and A. Luque. Reducing carrier escape in the InAs/GaAs quantum dot intermediate band solar cell. *Journal of Applied Physics*, 108(6):064513, 2010.
- [5] C. G. Bailey, S. M. Hubbard, D. V. Forbes, and R. P. Raffaelle. Evaluation of strain balancing layer thickness for InAs/GaAs quantum dot arrays using high resolution x-ray diffraction and photoluminescence. *Applied Physics Letters*, 95(20):203110, 2009.
- [6] D. Bimberg, M. Grundmann, and N. N. Ledentsov. *Quantum dot heterostructures*. Wiley, 1998.
- [7] S. A. Blokhin, A. V. Sakharov, A. M. Nadtochy, A. S. Pauysov, M. V. Maximov, N. N. Ledentsov, A. R. Kovsh, S. S. Mikhrin, V. M. Lantratov, and S. A. Mintairov. AlGaAs/GaAs photovoltaic cells with an array of InGaAs QDs. *Semiconductors*, 43(4):514–518, 2009.
- [8] N. J. Ekins-Daukes, K. W. J. Barnham, J. P. Connolly, J. S. Roberts, J. C. Clark, G. Hill, and M. Mazzer. Strain-balanced GaAsP/InGaAs quantum well solar cells. *Applied Physics Letters*, 75(26):4195, 1999.
- [9] G. González-Díaz, J. Olea, I. Mártí, D. Pastor, A. Martí, E. Antolín, and A. Luque. Intermediate band mobility in heavily titanium-doped silicon layers. *Solar Energy Materials and Solar Cells*, 93(9):1668–1673, 2009.
- [10] D. Granados and J. M. García. Customized nanostructures MBE growth: from quantum dots to quantum rings. *Journal of Crystal Growth*, 251(1-4):213–217, 2003.
- [11] M. A. Green, K. Emery, Y. Hishikawa, and W. Warta. Solar cell efficiency tables (version 37). *Progress in Photovoltaics: Research and Applications*, 19(1):84–92, 2011.
- [12] D. Guimard, R. Morihara, D. Bordel, K. Tanabe, Y. Wakayama, M. Nishioka, and Y. Arakawa. Fabrication of InAs/GaAs quantum dot solar cells with enhanced photocurrent and without degradation of open circuit voltage. *Applied Physics Letters*, 96(20):203507, 2010.
- [13] S. M. Hubbard, C. G. Bailey, R. Aguinaldo, S. Polly, D. V. Forbes, and R. P. Raffaelle. Characterization of quantum dot enhanced solar cells for concentrator PV. In *Proceedings 34th IEEE Photovoltaic Specialists Conference*, volume 1, pages 1–6, 2009.
- [14] M. Ji, S. Park, S. T. Connor, T. Mokari, Y. Cui, and K. J. Gaffney. Efficient multiple exciton generation observed in colloidal PbSe quantum dots

- with temporally and spectrally resolved intraband excitation. *Nano letters*, 9(3):1217–22, 2009.
- [15] M. Y. Levy, C. Honsberg, A. Martí, and A. Luque. Quantum dot intermediate band solar cell material systems with negligible valence band offsets. In *Proceedings 31st IEEE Photovoltaic Specialists Conference*, volume 31, page 90, 2005.
- [16] X. Li, Y. Wu, D. Steel, D. Gammon, T. H. Stievater, D. S. Katzer, D. Park, C. Piermarocchi, and L. J. Sham. An all-optical quantum gate in a semiconductor quantum dot. *Science*, 301(5634):809–811, 2003.
- [17] W.-H. Lin, C.-C. Tseng, K.-P. Chao, S.-Y. Kung, S.-Y. Lin, and M.-C. Wu. Broadband quantum-dot infrared photodetector. *IEEE Photonics Technology Letters*, 22(13):963–965, 2010.
- [18] A. Luque and A. Martí. Increasing the efficiency of ideal solar cells by photon induced transitions at intermediate levels. *Physical Review Letters*, 78(26):5014–5017, 1997.
- [19] A. Luque, A. Martí, E. Antolín, and P. García-Linares. Intraband absorption for normal illumination in quantum dot intermediate band solar cells. *Solar Energy Materials and Solar Cells*, 94(12):2032–2035, 2010.
- [20] A. Martí, E. Antolín, C. Stanley, C. Farmer, N. López, P. Díaz, E. Cánovas, P. Linares, and A. Luque. Production of photocurrent due to intermediate-to-conduction-band transitions: a demonstration of a key operating principle of the intermediate-band solar cell. *Physical Review Letters*, 97(24):1–4, 2006.
- [21] A. Martí, N. López, E. Antolín, E. Canovas, C. Stanley, C. Farmer, L. Cuadra, and A. Luque. Novel semiconductor solar cell structures: The quantum dot intermediate band solar cell. *Thin Solid Films*, 511-512:638–644, 2006.
- [22] A. Martí and A. Luque. *Next generation photovoltaics: high efficiency through full spectrum utilization*. Number 1. Taylor & Francis, 2004.
- [23] J. Martín-Sánchez, G. Muñoz Matutano, J. Herranz, J. Canet-Ferrer, B. Alén, Y. González, P. Alonso-González, D. Fuster, L. González, J. Martínez-Pastor, and F. Briones. Single photon emission from site-controlled InAs quantum dots grown on GaAs (001) patterned substrates. *ACS nano*, 3(6):1513–7, 2009.
- [24] K. Mukai, Y. Nakata, K. Otsubo, M. Sugawara, N. Yokoyama, and H. Ishikawa. 1.3- μ m CW lasing of InGaAs-GaAs quantum dots at room temperature with a threshold current of 8 mA. *IEEE Photonics Technology Letters*, 11(10):1205–1207, 1999.
- [25] N. Nuntawong, S. Birudavolu, C. P. Hains, S. Huang, H. Xu, and D. L. Huffaker. Effect of strain-compensation in stacked 1.3 μ m InAsGaAs quantum dot active regions grown by metalorganic chemical vapor deposition. *Applied Physics Letters*, 85(15):3050, 2004.
- [26] B. Ohnesorge, M. Albrecht, J. Oshinowo, A. Forchel, and Y. Arakawa. Rapid carrier relaxation in self-assembled In_xGa_{1-x}As/GaAs quantum dots. *Physical Review B*, 54(16):11532–11538, 1996.
- [27] R. Oshima, A. Takata, and Y. Okada. Strain-compensated InAs/GaNAs quantum dots for use in high-efficiency solar cells. *Applied Physics Letters*, 93(8):083111, 2008.
- [28] P. Palacios, I. Aguilera, K. Sánchez, J. Conesa, and P. Wahnón. Transition-Metal-Substituted Indium Thiospinels as Novel Intermediate-Band Materials: Prediction and Understanding of Their Electronic Properties. *Physical Review Letters*, 101(4):2–5, 2008.
- [29] P. Palacios, K. Sánchez, J. Conesa, J. Fernández, and P. Wahnón. Theoretical modelling of intermediate band solar cell materials based on metal-doped chalcopyrite compounds. *Thin Solid Films*, 515(15):6280–6284, 2007.
- [30] V. Popescu, G. Bester, M. Hanna, A. Norman, and A. Zunger. Theoretical and experimental examination of the intermediate-band concept for strain-balanced (In,Ga)As/Ga(As,P) quantum dot solar cells. *Physical Review B*, 78(20):1–17, 2008.
- [31] Q. P. Releases. http://www.quantasol.com/news/item/quantasol_unveils_28.

- 3_efficient_single-junction_solar_cell_world_reco/, 2009.
- [32] R. . G. S. Report. <http://www.ren21.net/>, 2010.
 - [33] J. Singh. *Electronic and optoelectronic properties of semiconductor structures*. Cambridge University Press, 2003.
 - [34] T. Sugaya, S. Furue, H. Komaki, T. Amano, M. Mori, K. Komori, S. Niki, O. Numakami, and Y. Okano. Highly stacked and well-aligned $\text{In}_{0.4}\text{Ga}_{0.6}\text{As}$ quantum dot solar cells with $\text{In}_{0.2}\text{Ga}_{0.8}\text{As}$ cap layer. *Applied Physics Letters*, 97(18):183104, 2010.
 - [35] J. Tatebayashi, N. Nuntawong, P. S. Wong, Y.-C. Xin, L. F. Lester, and D. L. Huffaker. Strain compensation technique in self-assembled InAs/GaAs quantum dots for applications to photonic devices. *Journal of Physics D: Applied Physics*, 42(7):073002, 2009.
 - [36] G. Wei and S. R. Forrest. Intermediate-band solar cells employing quantum dots embedded in an energy fence barrier. *Nano letters*, 7(1):218–22, 2007.
 - [37] M. Wolf. Limitations and possibilities for improvement of photovoltaic solar energy converters: Part I: Considerations for earth's surface operation. *Proceedings of the IRE*, 48(7):1246 –1263, 1960.
 - [38] A. Zunger, A. Franceschetti, J.-W. Luo, and V. Popescu. Understanding the physics of carrier-multiplication and intermediate-band solar cells based on nanostructures - What is going on? *Proceedings 34th IEEE Photovoltaic Specialists Conference*, 2009.



Acta Futura 4 (2011) 81-97

DOI: 10.2420/AF04.2011.81

**Acta
Futura**

Micro-to-Macro: Astrodynamics at Extremes of Length-scale

COLIN R. MCINNES*, MATTEO CERIOTTI, CAMILLA COLOMBO, JOAN-PAU SANCHEZ
RUSSELL BEWICK, JEANNETTE HEILIGERS AND CHARLOTTE LÜCKING

Advanced Space Concepts Laboratory, University of Strathclyde, Glasgow G1 1XJ, United Kingdom

Abstract. This paper investigates astrodynamics at extremes of length-scale, ranging from swarms of future ‘smart dust’ devices to the capture and utilisation of small near Earth asteroids. At the smallest length-scales, families of orbits are found which balance the energy gain from solar radiation pressure with energy dissipation due to air drag. This results in long orbit lifetimes for high area-to-mass ratio ‘smart dust’ devices. High area-to-mass hybrid spacecraft, using both solar sail and electric propulsion, are then considered to enable ‘pole-sitter’ orbits providing a polar-stationary vantage point for Earth observation. These spacecraft are also considered to enable displaced geostationary orbits. Finally, the potential material resource available from captured near Earth asteroids is considered which can underpin future large-scale space engineering ventures. The use of such material for geo-engineering is investigated using a cloud of unprocessed dust in the vicinity of the Earth-Sun L_1 point to fractionally reduce solar insolation.

1 Introduction

The growing utilisation of space as a platform for science, telecommunications, Earth observation and navigation is a direct result of the application of the tools of classical orbital dynamics. Many decades of ap-

plied research have translated key ideas from dynamical astronomy to spacecraft astrodynamics to generate families of orbits which now deliver essential scientific and commercial products such as high bandwidth data-links, high resolution multi-spectral imagery and precise global positioning. While such exciting space applications have transformed a range of both commercial and public services, the continued exploitation of space will require new innovations both in spacecraft technologies and in fundamental astrodynamics.

This paper provides an overview of an on-going programme of work which aims to deliver radically new approaches to astrodynamics at extremes of length-scale to underpin new space-derived products and services for space science, telecommunications and Earth observation. These include vast swarms of interacting MEMS-scale ‘smart dust’ devices for new science applications [9, 23], displaced polar and geostationary orbits for Earth observation and communications [6, 15] and new concepts for the capture and exploitation of small near Earth asteroids [33, 3], as illustrated schematically in Fig. 1.

Traditionally, astrodynamics has centred on the classical gravitational two-body problem, with additional forces treated as small perturbations. This approach allows the conic section solutions to the unperturbed gravitational two-body problem to form the basis of an understanding of the weakly perturbed problem (for example [18, 31]).

*E-mail address: colin.mcinnes@strath.ac.uk

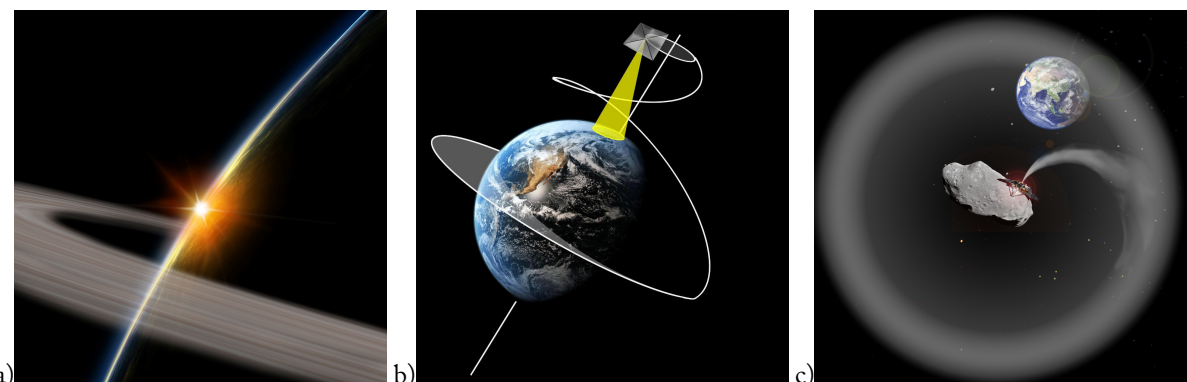


FIGURE 1. *Micro-to-macro: future space systems at extremes of length-scale (a) MICRO: swarms of 'smart dust' sensor nodes (b) MESO: pole-sitter orbits for gossamer spacecraft (c) MACRO: geo-engineering with captured near Earth asteroid material.*

Such an approach has provided the mathematical tools to enable, for example, orbit control of geostationary telecommunication satellites, the definition of mapping orbits for Earth observation satellites and coverage patterns for satellite navigation constellations.

More recently, the use of modern dynamical systems theory has led to exciting new developments in the gravitational three-body problem (for example [19, 13]). Work has explored the use of new families of trajectories connecting periodic orbits about the collinear libration points as the basis for highly efficient orbit transfer in the Earth-Moon and Earth-Sun systems. These more recent developments are a strong indication that there is much work still to be done in modern astrodynamics, and that many new families of useful orbits await discovery.

Future space systems will require a new approach to orbital dynamics from micro- to macroscopic length-scales L . This new understanding will be required to underpin the exploitation of future space systems from swarms of interacting MEMS-scale 'smart dust' devices ($L \sim 10^{-3}$ m) to extremely large gossamer spacecraft ($L \sim 10^3$ m). At these extremes of spacecraft length-scale, perturbations such as atmospheric drag, solar radiation pressure and electrodynamic forces can be of the same order of magnitude as the central two-body or three-body gravitational forces. The strongly perturbed nature of the dynamics of such spacecraft gives rise to rich new families of orbits which can be exploited to deliver new space products and services.

Gossamer spacecraft are characterised by a large deployable surface area, but a relatively modest mass, yield-

ing extremely low areal densities. These spacecraft are strongly perturbed by atmospheric drag and solar radiation pressure, and in the case of solar sails, utilise solar radiation pressure directly for propulsion. Similarly, micro-spacecraft are rapidly shrinking in mass and volume, driven by advances in integrated micro-electronics. Since spacecraft mass scales as L^3 , while surface area scales as L^2 , effective areal density scales as L^{-1} with diminishing spacecraft size. This again leads to strong atmospheric drag and solar radiation pressure perturbations and the possibility of electrodynamic effects due to natural or artificial surface charging. Therefore both classes of spacecraft, while at opposing ends of the length-scale spectrum, will require the integrated development of new methods in astrodynamics to explore such strongly perturbed orbits. At even larger length-scales, new insights into the three-body problem can enable the capture of small near Earth asteroids by greatly leveraging the effect of intervention by impulse or continuous thrust. The ability to efficiently capture such material could have a long-term impact on the feasibility and cost of future space systems at the largest length-scales such as space solar power and space-based geo-engineering.

Key questions to be addressed in each of the following three sections include:

- **MICRO:** How does the orbital dynamics of micro-spacecraft scale with rapidly diminishing spacecraft size and how can the orbits of swarms of such devices be controlled?
- **MESO:** Can different natural perturbations and low thrust propulsion technologies be combined to

enable new families of exploitable orbits for large gossamer spacecraft?

- MACRO: Can new insights from orbital dynamics bring forward the development of visionary, large-scale space engineering ventures by efficiently capturing near Earth asteroid resources?

2 MICRO: Astrodynamics for *smart dust* swarms

2.1 Long-lived orbits for smart dust devices

Recent innovations in spacecraft design have exploited advances in miniaturisation to fabricate small satellites with dimensions of a single micro-chip. Low-cost manufacturing of vast numbers of micro-spacecraft can lead to their use in swarm applications, and their small dimensions facilitate access-to-space through deployment in orbit as piggy-back on a conventional spacecraft. The deployment of vast numbers of '*SpaceChips*' will enable future missions, such as global sensor networks for Earth observation and communication, distributed space missions for multi-point, real-time sensing for space science, interplanetary exploration in support of traditional spacecraft, deployment in the vicinity of a spacecraft for environmental and damage detection, or possibly future space-based geo-engineering applications. Even if limited, micro-spacecraft are also capable of long-term orbit control through the exploitation of perturbations such as Lorentz force, solar radiation pressure or atmospheric drag and vicinity control by means of spacecraft-to-spacecraft interaction through the Coulomb force.

Moreover, the exploitation of orbital dynamics at extremely small length-scales can enable novel families of exploitable non-Keplerian orbits. Due to the extremely high area-to-mass ratio (A/m) of future SpaceChips, or smaller '*smart dust*' devices, with respect to conventional spacecraft, perturbations such as solar radiation pressure (SRP) and aerodynamic drag, which goes as A/m , become dominant with respect to the Earth's gravity. The study of the long-term effect on the satellite's orbit caused by those perturbations generates equilibrium orbits where the total variation of semi-major axis and eccentricity due to SPR and drag is zero, and the effect of SRP is exploited to obtain Sun-synchronous precession of the apse-line passively, without the use of active control. In those regions of the orbital element phase space where solar radiation pressure and atmospheric

drag both have a non-negligible effect on the spacecraft orbit, complete equilibrium is not possible. However, the long-term orbit evolution still presents some intriguing behaviour; if the initial conditions are in a certain region around the equilibrium solution set, the long-term evolution is characterised by librational motion, progressively decaying due to the non-conservative effect of atmospheric drag [11, 10] (see Fig. 2). It is possible to define different arcs of the orbit evolution where the trajectory is dominated either by drag or by solar radiation pressure.

The natural effects of solar radiation pressure and atmospheric drag perturbations can be exploited to design swarm missions, for example, for the mapping and study of the upper regions of the Earth's atmosphere [9]. A swarm of SpaceChips is deployed on the ecliptic plane from a single spacecraft, as distributed nodes of a network to obtain a spatial and temporal map of the ionosphere and exosphere. By selecting the release conditions in terms of angular displacement ϕ between the orbit pericentre and the direction of the Sun-Earth line, the effect of SRP is exploited to scatter the devices into a set of different orbits which cover an extended, but bounded, region of the atmosphere, collecting distributed measurements.

Figure 2 shows the long-term evolution of the SpaceChip swarm after release from a conventional spacecraft. For the first part of the orbit evolution for $\phi < \pi$ the secular rate of change of the eccentricity is negative; as a consequence the orbit perigee rises reaching its maximum at $\phi = \pi$. Afterwards, when $\phi > \pi$, the secular variation of eccentricity is negative, hence the perigee height decreases.

Importantly, the short lifetime of high area-to-mass spacecraft can be greatly extended (and indeed selected) through the interaction of energy gain from asymmetric solar radiation pressure and energy dissipation due to drag (see blue line in Fig. 6). Due to the large area-to-mass ratio of these devices orbit lifetime due to air drag alone is extremely short (see green lines in Fig. 2 and Fig. 6). In addition, the effect of atmospheric drag can be exploited to obtain a fast decay of the swarm of devices in the terminal phase of the mission, ensuring their end-of-life disposal and avoiding the creation of long-lived space debris from the swarm.

More intriguing new behaviours are found when planet's oblateness is considered in the governing equations and the motion is not bounded to the ecliptic plane.

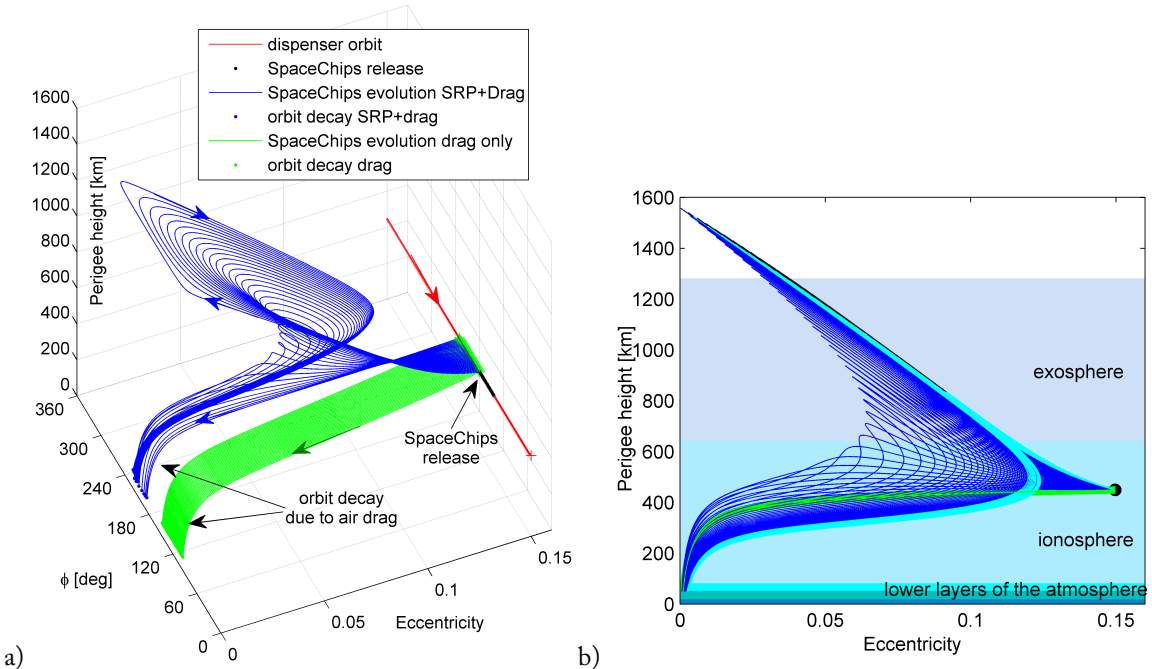


FIGURE 2. SpaceChip swarm mission. As a conventional dispenser spacecraft moves on its orbit (red), it releases a number of SpaceChips, whose long-term evolution under the effect of SRP and drag is represented by the blue line. The long-term evolution under drag only is represented with the green line. (a) Orbit evolution in the phase space. (b) Atmosphere coverage in the eccentricity-perigee height plane. The exploitation of SRP allows coverage of a more extended region of the atmosphere from the device release (black point) until the final decay (when the perigee height decreases below 50 km).

2.2 Electrochromic orbit control of high area-to-mass ratio spacecraft

Possible mission concepts for swarms of ‘smart dust’ devices can be extended by including active orbit control over the long-term evolution of the swarm. An electrochromic coating of the SpaceChip device can be employed to alter the reflectivity coefficient of the spacecraft. This control method is intended primarily for micro-scale satellites-on-a-chip that do not possess the physical size for conventional orbit control actuators such as thrusters and have a naturally high area-to-mass-ratio. However, larger satellites could also exploit these findings by employing a large lightweight inflatable balloon with an electrochromic coating. Electrochromic materials are already widely used in terrestrial applications such as intelligent sunshades, tinting windows and flexible thin film displays and have been used in space applications, albeit not for orbit control. The recently launched IKAROS solar sailing demonstrator uses electrochromic surfaces on the sail to ad-

just its attitude and electrochromic radiators have been developed for thermal control. Electrochromic materials (EM) change their optical properties when a voltage is applied, thus modulating the fraction of light which is transmitted, absorbed and reflected, therefore effectively changing the reflectivity coefficient c_R of the spacecraft between two set values ($c_{R\min} = 1$ and $c_{R\max} = 2$). The acceleration any object receives from the solar radiation pressure is given by:

$$\mathbf{a}_{SRP} = c_R \frac{p_{SR} A_\odot}{c m} \quad (1)$$

where c_R is the coefficient of reflectivity, p_{SR} the solar flux, c the speed of light, A_\odot the effective surface area receiving solar radiation and m is the mass of the object. It can be seen that the value of a_{SRP} in Eq. (1) depends on the area-to-mass ratio of the object. Conventional spacecraft experience SRP only as a perturbing force whereas the effect on micro-scale satellites becomes dominant. Because of the discrete nature of the reflectivity change, the orbit control has the characteris-

tics of a on-off controller with the lower reflectivity state ($c_{R \min}$) of the EM thin-film defined as the off-state and the higher reflectivity state ($c_{R \max}$) as the on-state. It is assumed that during each orbit the reflectivity can be switched twice. The true anomalies at which these changes take place are used as control parameters.

Through this control method the effect of SRP can be modulated to stabilise the spacecraft in certain sun-synchronous, elliptical orbits and orbital manoeuvres can be performed [23]. For stabilisation, an artificial potential field controller has been implemented using a quadratic potential in the orbital element phase space around the desired stabilisation point. A region in the eccentricity- ϕ -phase-plane has been identified where spacecraft could be stabilised indefinitely. For orbital manoeuvres, instead, the electrochromic control method is used to balance the effect of eclipses to keep a constant semi-major axis. There are two possible solutions achieving this, by maintaining the reflectivity mainly low or mainly high along each single orbit revolution. This choice will determine the set of flow lines the spacecraft will follow in the phase space. Each member of the swarm can be thus navigated, depending on its current position in the phase space with respect to the targeted final position.

The results of a case study are shown in Fig. 3; eight SpaceChips starting from different initial orbits are collected into the same final orbit within one year using electrochromic orbit control. On the left the initial and final orbits are displayed. The right figure shows the evolution of the eccentricity, ϕ , over time, while the semi-major axis remains constant, and the centre figure shows the evolution of the orbits in the phase plane. The spacecraft start on the orbits marked by the coloured circles and then progress following the flow lines towards the goal orbit marked with a black circle. The dashed flow lines correspond to the higher reflectivity control option, the dotted lines to the lower reflectivity control option.

2.3 Extension of the mission design through active control of the swarm

The mission concepts presented in Section 2.1 can be extended by including active orbit control over the long-term evolution of the SpaceChip swarm [8]. The control relies on a basic bang-bang control algorithm based on a simplified version of the electrochromic orbit control introduced in Section 2.2. The spacecrafts follow the natural flow lines in the orbital element phase space for

the major part of their evolution accepting a change in semi-major axis due to eclipses. The change of reflectivity coefficient takes place every time the angle between the orbit pericentre and the direction of the Sun-Earth line ϕ goes through π (see Fig. 4)

$$c_R = \begin{cases} c_{R \max}, & \text{if } \phi < \pi \text{ and } t \leq T_{\text{mission max}} \\ c_{R \min}, & \text{if } \phi \geq \pi \text{ and } t \leq T_{\text{mission max}} \\ c_{R \max}, & \text{if } t > T_{\text{mission max}} \end{cases} \quad (2)$$

In this way the long-term control of the orbit can be achieved and a swarm of SpaceChips moving along different librational loops can be stabilised in the phase space at $\phi = \pi$, with an eccentricity within a certain range. Once the stabilisation region is reached, the spacecraft will change its reflectivity value, once per orbit, thus keeping its orbital elements fixed in a position of the phase space which, otherwise, will not be in equilibrium. To avoid the debris hazard of the swarm existing for an indefinite time, the duration of the mission is limited to a maximum value $T_{\text{mission max}}$, after which the control algorithm is turned off and the swarm naturally evolves towards a fast decay, due to the effect of atmospheric drag.

Figure 5 shows the evolution of the perigee heights with time. The passive exploitation of SRP (blue lines) allows an increase of the perigee height and an extension of the lifetime with respect to the drag-only scenario (green lines). The control strategy (red lines) for the reflectivity coefficient allows stabilising the members of the swarm at a constant perigee for a long duration. Importantly, the effect of SRP causes a significant increase in the orbit lifetime with respect to the drag-only case, as shown in Fig. 6, as a function of the angular displacement at release. The green line represents the orbit lifetime of the swarm in the case SRP is not considered, and the blue line corresponds to the passive evolution under drag and SRP with a constant value or reflectivity $c_R = c_{R \max}$. If the control strategy in Eq. 2 is implemented, the swarm lifetime is shown with the red line.

3 MESO: Astrodynamics for gossamer spacecraft

The orbital dynamics of a large, high-area-to-mass ratio spacecraft is greatly influenced by natural perturbations, generating new kinds of exploitable orbits. For example, non-Keplerian orbits (NKO) are those in which a small, but continuous acceleration is used to generate

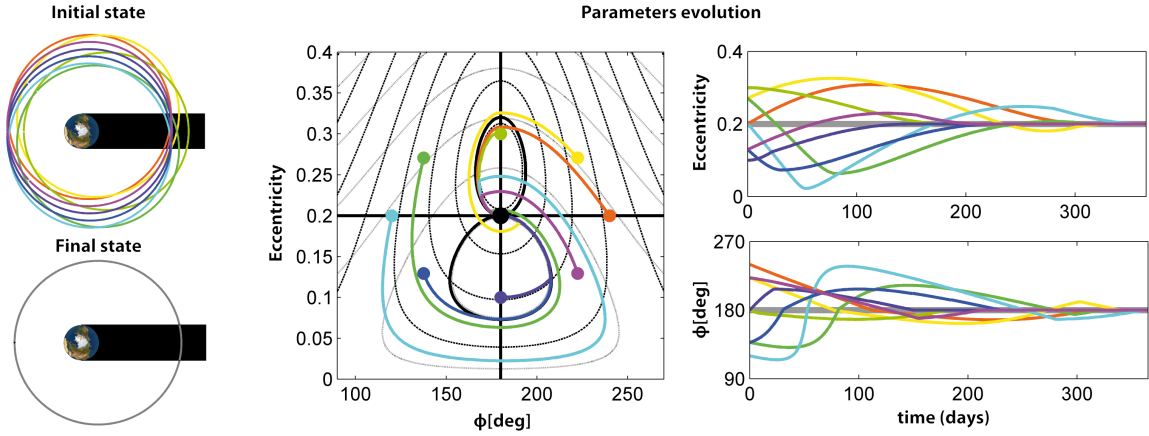


FIGURE 3. Results of a case study simulation for the electrochromic orbit control. Initial and final orbital state of eight spacecraft and evolution of their orbital parameters in the e - ϕ -phase space and over the time of the simulation (1 year).

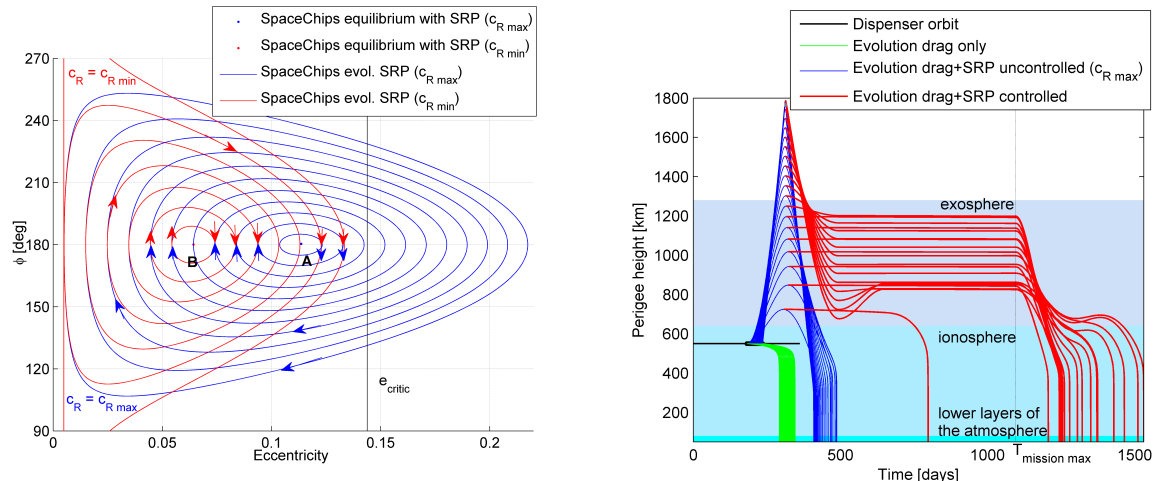


FIGURE 4. Schematic of the control algorithm based on the reflectivity coefficient change.

periodic orbits that do not follow the natural dynamics of the system [26]. Both solar sailing [2] and solar electric propulsion (SEP) [25] have been proposed as technologies to enable these kind of missions. However, we propose to hybridise the two technologies on a gossamer spacecraft [21], and investigate the advantages.

In the hybrid spacecraft, the sail is fixed on the spacecraft bus and its thrust is controlled by changing the sail attitude. Solar arrays or thin film solar cells (TFSC) partially covering the sail surface are used to power the SEP thruster. This is assumed to be mounted on a gimbal,

FIGURE 5. Evolution of the swarm under the effect of drag-only (green lines), drag and SRP uncontrolled (blue lines), drag and SRP controlled (red lines).

such that the direction of its thrust can be controlled. At the cost of increased spacecraft complexity, the two separate propulsion systems complement each other, cancelling their reciprocal disadvantages and limitations. In principle, a steerable SEP thruster can provide the missing acceleration component (towards the Sun) that the sail cannot generate. Similarly, the hybrid spacecraft can be seen as an SEP spacecraft, in which an auxiliary solar sail provides part of the acceleration, en-

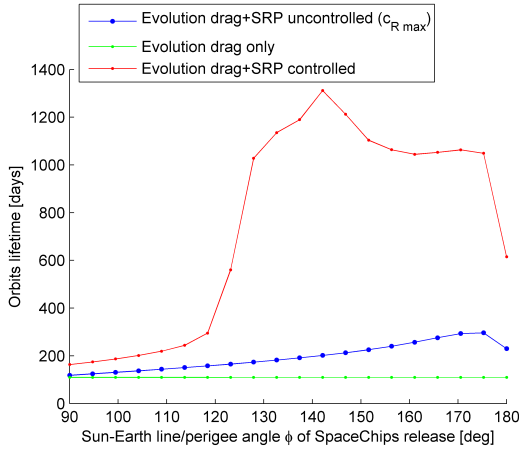


FIGURE 6. Orbit lifetime as function of the angular position of SpaceChips release.

abling saving of propellant and a lower demand on the electric thruster, possibly with some intervals in which it could be turned off. In this sense, the hybrid spacecraft can be seen as a way to gradually introduce solar sails for space applications [29], and hence to reduce the advancement degree of difficulty (AD2) [24] in the technology readiness level scale.

To maximise the performance of the hybrid spacecraft, the objective is to minimise the SEP propellant consumption. When the position, velocity and mass of the spacecraft are known at a particular instant of time, the acceleration due to gravitational forces (that need to be counterbalanced by the hybrid propulsion) can be computed, and thus the problem is to find the optimal solar sail cone and clock angles α, δ such that the SEP acceleration a_T is minimised [5]:

$$(\alpha^*, \delta^*) = \arg \min (a_T (\alpha, \delta)) \quad (3)$$

By exploiting this method, this section investigates the application and advantages of hybrid propulsion for two types of NKO: optimal Earth pole-sitter orbits and displaced geostationary orbits.

3.1 Optimal Earth pole-sitter orbits

A pole-sitter is a spacecraft that is constantly above one of the Earth's poles, i.e. lying on the Earth's polar axis [12]. This type of mission could provide a continuous, hemispherical, real-time view of the poles, and will enable a wide range of new applications in climate science and telecommunications [20].

We consider the Sun-Earth circular restricted three-body problem (CR3BP). Since the polar axis of the Earth is almost fixed while the Earth rotates around the Sun, in the synodic reference frame, it appears to span a full conical surface of half angle 23.5 deg every year. The spacecraft has to follow the same motion during its mission, and this can therefore be translated into constraints on the position as a function of time (see Fig. 7).

We seek optimal periodic pole-sitter orbits that exploit the solar sail to minimise the SEP propellant consumption over a fixed period (one year), while maintaining the pole-sitter condition at each instant during the mission. Optimal orbits are defined in terms of evolution of the states (position, velocity, mass), and controls (sail cone and clock angles, SEP thrust direction and magnitude) over one year. The optimal orbit design is performed in two steps. In the first step, after assigning a trajectory that satisfies the pole-sitter constraints, a locally-optimal control history is found, through a semi-analytical procedure, solving the problem in Eq. 3. This solution is then used for initialising the second step, which optimises the first guess through a pseudospectral transcription of the optimal control problem. Details of the design and optimisation process are covered in [5]. The analysis is done for both the pure SEP spacecraft, and the hybrid spacecraft in a range of system lightness numbers β_0 , which is proportional to the area-to-mass ratio of the hybrid sailcraft, and hence a measure of the sail size for a given initial mass.

First, it is found that a consistent gain in propellant mass fraction is obtained by adding a small sail to a pure SEP spacecraft. As the lightness number increases towards very high values, the gain in propellant mass for a given increase of β_0 becomes less. However, this fact justifies the investigation of the hybrid spacecraft, seen as a pure SEP system with a small-lightness-number auxiliary sail.

If the distance of the spacecraft from the Earth is kept constant (an example of such an orbit is in Fig. 8), it is found that an optimal distance exists at which the propellant consumption is minimised. This distance is approximately 0.018 AU (or about 2.7 millions of km), depending on the lightness number, and is of the same order as that of the Lagrangian point L₁ of the Earth-Sun system (1.5 million km from the Earth).

Note that the distance from the Earth can be varied: this degree of freedom can be used to find novel families of optimal orbits, leading to additional propellant mass saving. Different optimal orbits are found depending on

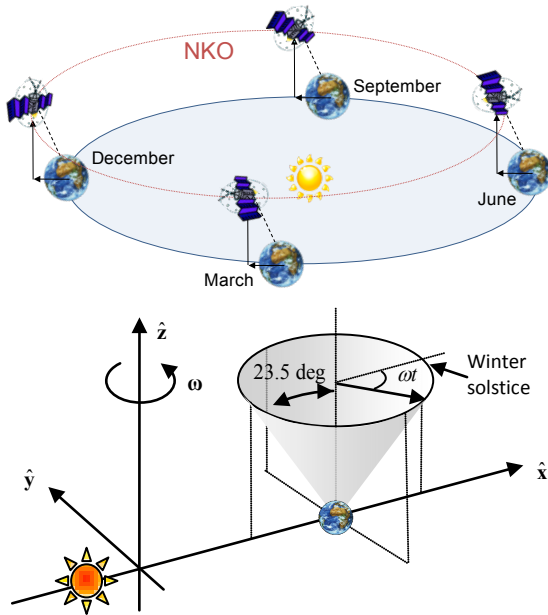


FIGURE 7. Apparent precession of the Earth's polar axis due to rotation of reference frame. (a) Inertial frame. (b) Synodic frame.

the value of β_0 . Optimal orbits get closer to the Earth in winter and farther in summer, as the lightness number of the solar sail increases. The distance can even double from winter (2 million km) to summer (4 million km) for a hybrid spacecraft with a lightness number of 0.1 (Fig. 9).

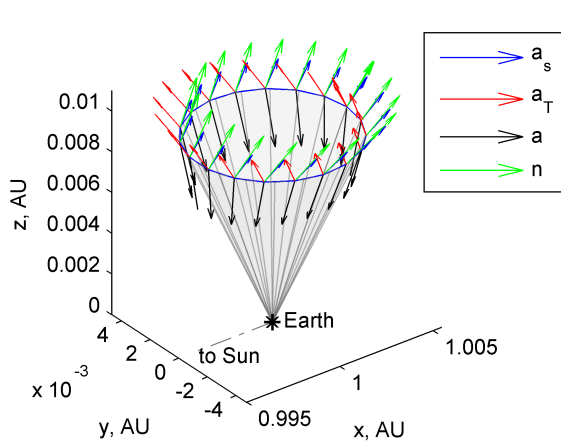


FIGURE 8. Sail acceleration (a_s), SEP acceleration (a_T), total gravitational acceleration (a) and sail normal (n) on a constant-distance orbit at 0.01 AU.

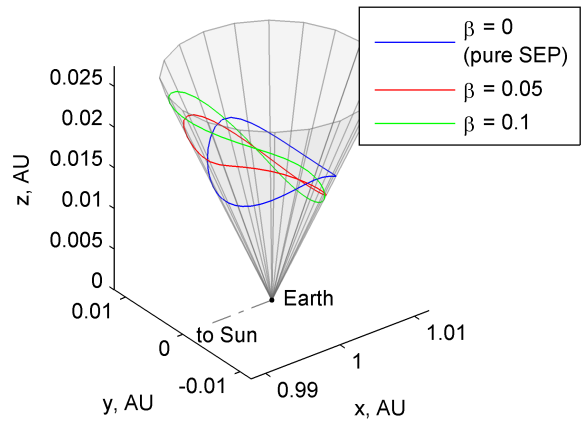


FIGURE 9. Minimum propellant mass hybrid pole-sitter orbits, for three different values of β_0 .

By comparing optimal solutions for pure SEP and hybrid spacecraft, it is found that the latter requires a lower propellant mass fraction. A substantial saving in propellant is obtained by adding a relatively small sail: considering an initial mass of 1000 kg, an SEP specific impulse of 3200 s and an optical sail model, for a 1-year orbit, the propellant mass decreases from 158 kg (for the pure SEP) to 97 kg ($\beta_0 = 0.05$).

However, the hybrid spacecraft is a more complex system, mainly due to the presence of the solar sail and the need for a gimballed thruster. Therefore, a preliminary systems design is performed, to assess the conditions at which the hybrid spacecraft is advantageous over the conventional SEP one, in terms of a lower initial mass for carrying the same payload mass.

It is found that, with near- to mid-term sail technology (sail loading of 7.5 g/m^2), the hybrid spacecraft has a lower initial mass than the SEP case if the mission duration is 7 years or more, with greater benefit for longer missions. Assuming far-term sail technology (5 g/m^2), then the hybrid spacecraft outperforms the pure SEP case even for short missions [7]. The comparison is performed varying the distance from the Earth optimally for each type of spacecraft.

Due to the instability of pole-sitter orbits, a feedback control is necessary to keep the spacecraft on track, counterbalancing errors and small perturbations that are not considered in the dynamics for the reference solution, as well as errors in the spacecraft model (e.g. unpredictable degradation of the sail). It was shown [6] that it is possible to keep the spacecraft on-track, and counterbalance injections errors, only by using the SEP thruster, while maintaining the sail at nominal attitude. Furthermore, it was shown that a relatively small variation of the reference thrust vector is sufficient to respond to large injection errors (order of 100,000 km), and to recover from relatively long SEP failures (up to 35 days).

3.2 Displaced geostationary orbits

With a period equal to the Earth's rotational period, spacecraft in geostationary orbit (GEO) are stationary with respect to their ground station, allowing for a continuous downlink to Earth. Vital telecommunication and Earth observation satellites are currently exploiting this unique property of the geostationary orbit. However, due to limits imposed by east-west spacing requirements, the GEO is starting to get congested at certain key longitude slots [17]. Therefore, in order to increase its capacity, we propose the use of displaced NKOs.

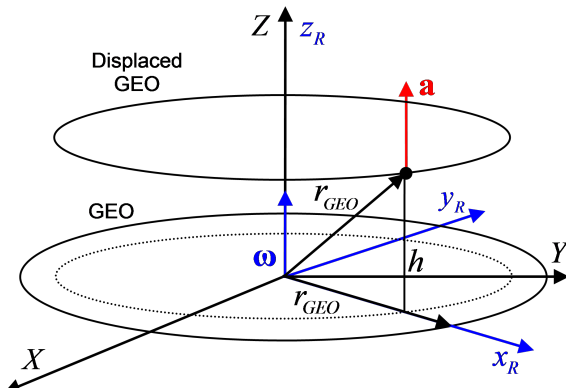


FIGURE 10. Definition of displaced geostationary orbit (GEO)

By applying a continuous acceleration to counterbalance the gravitational acceleration, the geostationary orbit can be levitated above or below the equatorial plane, thereby creating new geostationary slots. Pure solar sailing has already been considered to maintain such displaced geostationary orbits, but a residual force in the equatorial plane causes the spacecraft to move with respect to its ground station. Furthermore, only small displacements, still inside the geostationary station keep box, appeared to be feasible, causing collision risk to spacecraft in the geostationary orbit [2]. To overcome these problems, we propose to maintain the displaced GEO using hybrid propulsion.

We can find displaced geostationary orbits, or displaced NKOs in general, by seeking equilibrium solutions to the two- or three-body problem in a rotating frame of reference. A transformation to an inertial frame will subsequently show that the spacecraft executes a circular orbit displaced away from the centre of the central body [26].

The situation as it occurs in the displaced geostationary orbit is depicted in Figure 10: the geostationary orbit is levitated over a distance h while keeping both the orbital radius and the orbital angular velocity equal to the orbital radius and orbital angular velocity in the geostationary orbit, r_{GEO} and ω respectively. This case corresponds to a so-called 'Type I' NKO for which the required thrust induced acceleration is at its minimum [27]. The direction of the required acceleration is pure out-of-plane and, for the displaced GEO, the magnitude is solely a function of the displacement distance h . With the required acceleration known, the minimisation problem in Eq. 3 can be solved for a particular value

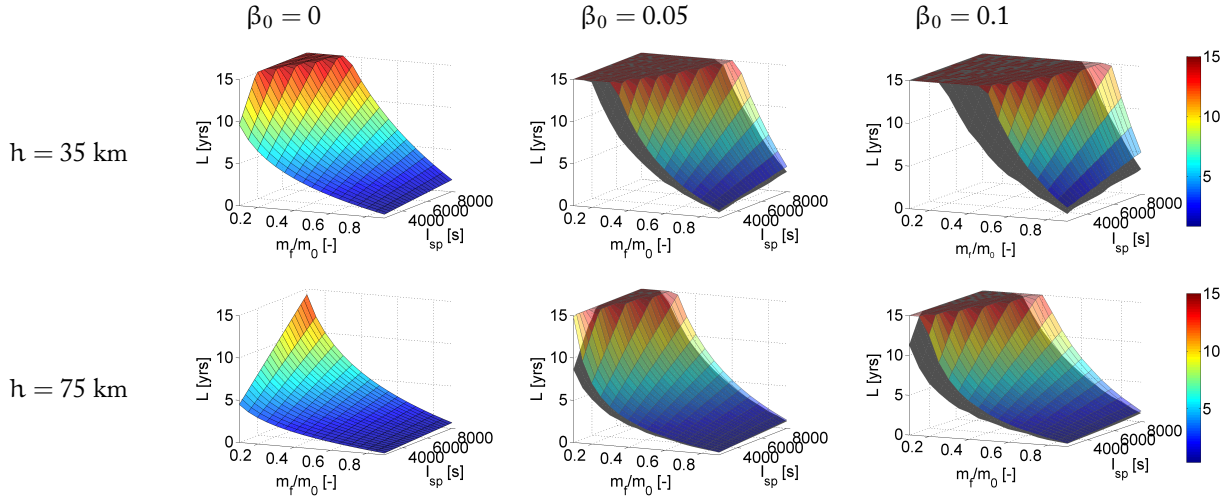


FIGURE 11. Mission lifetime L as a function of the specific impulse I_{sp} and the mass fraction m_f/m_0 , for different values of the system lightness number β_0 and the displacement distance h . The coloured surfaces include a seasonal transfer between a geostationary orbit displaced above and below the equatorial plane. The grey surfaces exclude this transfer.

for h . Analytical formulae for the optimal steering law are found by setting the partial derivative of the SEP acceleration with respect to the sail pitch and yaw angles equal to zero and requiring that the second derivative is positive. As mentioned, Eq. 3 can be solved at a particular instant in time, i.e. for a given value for the mass and given time during the year. The latter is related to the change in the direction of the Sun-sail line due to the tilt of the Earth's rotational axis with respect to the ecliptic plane. By using a discretisation of the orbit into equally distributed nodes, the analysis described can be extended to find the variation of the SEP and solar sail controls and accelerations, SEP thrust magnitude and spacecraft mass as a function of time over multiple orbital periods [15].

Performing this analysis provides the results as shown in Figure 11, where the performance of the hybrid spacecraft is expressed through the mission lifetime, L . This lifetime is dependent on the amount of propellant onboard the spacecraft, which is represented by the spacecraft dry mass fraction, m_f/m_0 , with m_0 the initial spacecraft mass and m_f the spacecraft mass after time L . The figure shows that a wide range of SEP specific impulses are considered. Furthermore, considering a standard geostationary station keeping box of 0.05° - 0.1° , equalling 36.8 - 73.6 km, two different displacement distances of 35 and 75 km are investigated. Finally, three different values for the system lightness number

are adopted, including the case where $\beta_0 = 0$, which represents the use of pure SEP propulsion and is used for comparison.

Figure 11 shows that, for example, for a 35 km displaced orbit, a currently feasible specific impulse of 3200 s and a mass fraction of 0.5 , a lifetime of 3.5 years can be achieved for the pure SEP case, which increases to 9.7 and 15 years for hybrid propulsion, depending on the value chosen for β_0 . A slight decrease in the performance can be observed for the higher displaced orbit as for similar values for the specific impulse and mass fraction, lifetimes of 2.9 and 4.3 years can be achieved. Note that these results assume an SEP transfer between a geostationary orbit displaced above the equatorial plane and an orbit displaced below the equatorial plane twice a year, in spring and in autumn, to make full use of the annual changing Sun-sail line direction. Solving the accompanying optimal control problem using a direct pseudo-spectral method shows that this transfer requires an almost negligible propellant budget. To show the influence of this transfer on the performance of hybrid propulsion, Figure 11 also includes the results when the hybrid spacecraft is maintained above the equatorial plane throughout the year. Then, a decrease in the lifetime of a few months up to a few years can be observed, but still exceeds the lifetimes of a pure SEP mission.

To investigate whether the mass fractions and specific impulses of Figure 11 allow for a payload to be carried

during the lifetimes shown in those figures, a preliminary spacecraft mass budget is considered to express the performance of the hybrid spacecraft in terms of payload mass capacity. For this, a maximum initial mass, such that the thrust magnitude does not exceed 0.2 N during the mission lifetime, is assumed. Further details on the mass breakdown and technological assumptions can be found in [15]. The results are shown in Figure 12. Considering a lifetime of 10–15 years for current geostationary spacecraft, Figure 12 shows that only hybrid propulsion enables such lifetimes while still allowing for useful payload masses of 255 to 489 kg to be carried on board in a 35 km displaced orbit, while reasonable lifetimes with somewhat smaller payloads can be obtained for the larger displacement of 75 km.

4 MACRO: Astrodynamics for visionary concepts

The final research theme aims to perform speculative research from a level-headed perspective in order to map out possible long-term futures for the utilisation of space by exploiting new insights into astrodynamics. Examples of this speculative research are space-based geo-engineering and asteroid capture and exploitation.

The current consensus within the scientific community is that global warming is currently happening due to the large quantities of greenhouse gases such as CO₂ and methane that are emitted into the atmosphere. It is clear from the slow movement of international agreements on emission restrictions that, should emission caps be put in place, they may be too late to prevent the Earth from warming above the 1.5 – 2.5 °C that many fear could cause irreversible effects [16]. Hence it is prudent to investigate possible methods to mitigate the effects of global warming by the deliberate manipulation of the Earth's climate. This field is generally referred to as geo-engineering or climate engineering.

Many proposals have been made for possible geo-engineering schemes and have been evaluated in a study by the Royal Society in 2009 [34] based on affordability, timeliness, safety and effectiveness. The report concludes that currently too little is known about the possible consequences of these methods to recommend a single system, but also that the best method of implementation is likely to be a mixture of different methods. Aspects of this research theme aims to improve the ability of one of these methods, space-based geo-engineering, to mitigate the worst effects of climate

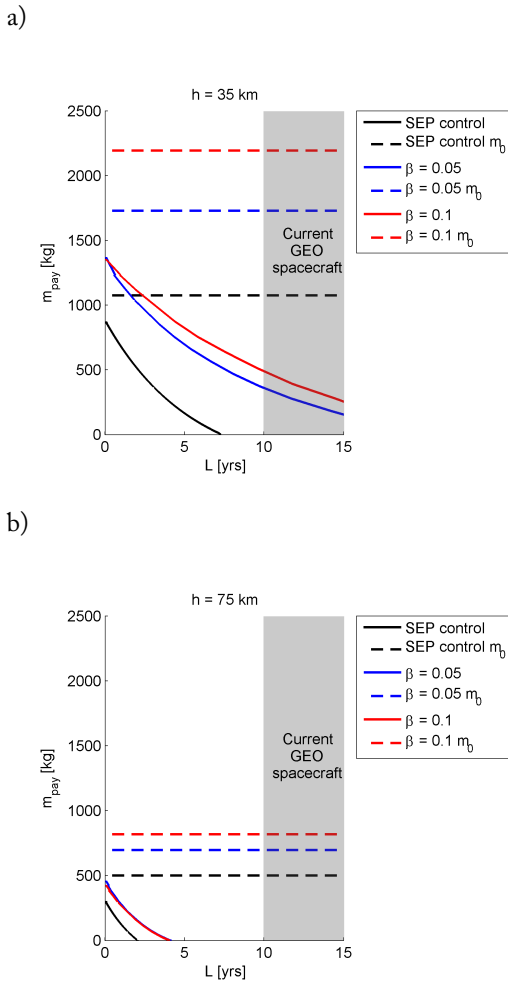


FIGURE 12. Payload mass m_{payload} as a function of the mission lifetime L for different values of the system lightness number β_0 and for $I_{\text{sp}} = 3200$ s. (a) 35 km displacement. (b) 75 km displacement.

change.

Several scenarios for space based geo-engineering platforms have already been identified [1, 28, 30, 35]. All of these possible solutions require an enormous engineering effort comparable only to the largest engineering ventures on Earth (e.g., Three Gorges dam or Panama Canal), but in a much more hostile environment. However, the level of the engineering undertaking necessary for space geo-engineering, as well as for other future space applications such as space solar power satellites and space tourism, may be relieved to some extent by utilising materials that are already available in space [33].

4.1 Capture of near Earth asteroid material

Small celestial objects, i.e., asteroids and comets, have long been identified as possible reservoirs of materials for utilisation in space. Some examples of this are volatiles for propellant, water for life support, metals for structures, semiconductors for solar cells or simply regolith for radiation shielding [22]. In particular, near Earth asteroids (NEA) have recently risen in prominence because of two important points: they are among the easiest celestial bodies to reach from the Earth and they may represent a long-term threat. A range of methods have also been identified as able to provide a change in the asteroid linear momentum, sufficient to deflect an asteroid on a collision trajectory with the Earth [32]. Using these methods, a resource-rich asteroid could in principle be manoeuvred and captured into a bound Earth orbit through judicious use of orbital dynamics. The capture and transport of the entire NEA into an Earth orbit, for posterior processing, would require more energy than the transport of processed material directly from the unperturbed asteroid orbit. However, the mining and processing of materials in-situ would entail very complex and long duration missions. Both of these scenarios, in-situ processing and transport or asteroid capture, imply different mission architectures and the optimality of one option with respect to the other may ultimately depend on the technology readiness of the different mission systems, as well as the orbit of each particular asteroid and resource to be exploited. Nevertheless, the required Δv , as a measure of specific energy, is a good figure of merit that provides a qualitative estimate of the required scale of engineering necessary for any of the two options. The question that arises then is how much near-Earth asteroid material is there which could be captured with a modest investment of energy. This latter question can be answered by comparing the accessible Keplerian orbital regions with a NEA model able to predict the statistical probability of the existence of an asteroid with a given set of orbital elements and diameters (see Fig. 13). The accessible Keplerian region can be delimited by defining a multi-impulsive Keplerian transfer parameterised by the transport cost parameter Δv . The simplest transfer can be modelled by two impulses: first, a change of plane in order to yield a coplanar encounter with Earth, which ensures that if the asteroid is an Earth-crossing object, this would actually cross the Earth's orbital path, and second, a final insertion burn that takes place at the periapsis passage of the Earth encounter. This transfer, as with a Hohmann

transfer analysis, provides a good conservative estimate of the exploitable asteroid material. A capture transfer that considers only one single impulse during the periapsis passage of the asteroid can also be modelled. For this second transfer, one needs to compute the subset of asteroids with a given semi-major axis, eccentricity and inclination set $\{a, e, i\}$ that have an orientation such that a serendipitous fly-by with the Earth is possible. Figure 13, for example, shows the accessible volume of the $\{a, e, i\}$ Keplerian subspace considering a one-impulse capture with a Δv threshold at 2.37 km/s, the value required to escape lunar gravity, used to provide a comparison of energy investment [33]. The NEA density distribution is computed by interpolating the theoretical distribution published by Bottke et al. [4] and can also be seen in Fig. 13.

One can then assess the availability of asteroid material on easily accessible orbits by computing the median diameter of the object that can be found within a given Δv limit. Figure 14 shows the median diameter of the first, tenth, hundredth and thousandth largest accessible asteroid in the near Earth space, together with the 90% confidence region for each one of these objects. While the median diameter indicates that there is 50% chance that the j^{th} -largest accessible asteroid could be larger or smaller than the median diameter, the confidence region provides a cumulative 90% chance to find an object size within the shaded area. Finally, the figure also shows the expected median diameter of the accessible objects when the maximum transfer time is set to 40 years. The information in the figure can be read as follows: let us, for example, set the Δv threshold at 100 m/s, the largest accessible object has a 50% probability to be equal to or larger than 24 meters diameter, while we can say with 90% confidence that its size should be between 72 meters and 12 meters. These results are computed assuming a phase free transfer, while if a random, but fixed initial phase is assumed, and 40 years of transfer time are allowed, then the result of the median diameter decreases to 23 meters. The following set of data in the decreasing ordinate axis is the group referring to the 10th largest object found within the region of feasible capture given by a Δv threshold of 100 m/s, whose median diameter is at 8 meters diameter. The 100th largest object is foreseen to have a diameter of 3 meters and 1000th largest of 1 meter.

The results shown in the latter figure highlight the feasibility of future asteroid resource utilisation. One can imagine advantageous scenarios for space utilisation from the results on the expected size of the accessible

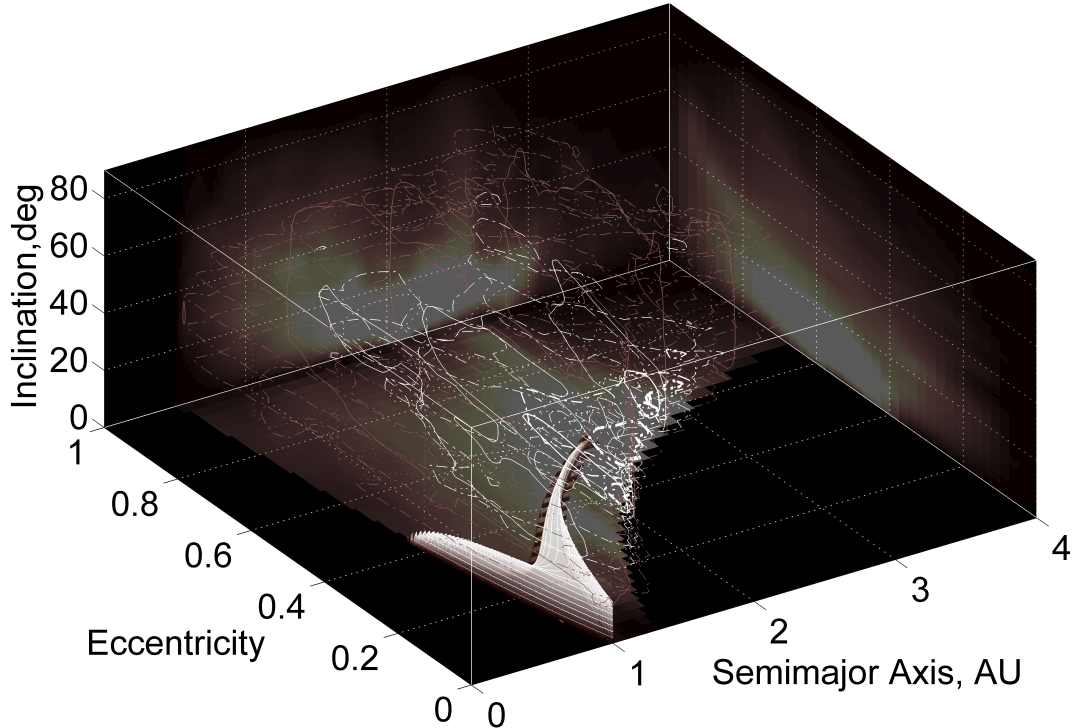


FIGURE 13. Accessible region for asteroid exploitation by means of a one-impulse manoeuvre with a $2.37 \text{ km/s } \Delta v$ (i.e., v -shaped volume) [33]. Also in the figure, Near-Earth asteroid density distribution represented by a set of isolines within the $\{a,e\}$ and $\{a,i\}$ planes and cumulative projection of the density at each side wall.

material. For example, the exploitation of the largest expected object found within a 100 m/s budget, a 24-m asteroid, could supply from 10^7 kg to $4 \times 10^7 \text{ kg}$ of asteroid material, depending on composition and density. If this object was a hydrated carbonaceous asteroid, a million litres of water could possibly be extracted. However, if this object was an M-class asteroid, of order thirty thousand tonnes of metal could potentially be extracted and even a tonne of Platinum Group Metals (PGM). The latter resource could easily reach a value of fifty million dollars in Earth's commodity markets. If the Δv budget is increased to 1 km/s, one 190-m diameter object should be accessible. This corresponds to more than 300 million litres of water or more than 10 million tons of metal and 600 tons of PGMs valued at 30 billion dollars.

4.2 Geo-engineering using captured near Earth asteroids

Another possible use of near Earth asteroids is to provide material for space-based geoengineering schemes. Space-based geoengineering focuses on solar radiation management, i.e., reducing the amount of sunlight reaching the Earth, to create a cooling effect. These methods have either proposed placing large clouds of dust around the Earth or at the $L_4 \backslash L_5$ points in the Earth-Moon system [35] or placing large solar reflectors\refractors at the L_1 point in the Sun-Earth system [1, 28] or also in Earth orbit [30]. In general, the dust cloud methods require much larger total masses due to the dispersed nature of the material, but also because the positions suggested so far mean that for much of the time dust will not be in a position to reflect solar

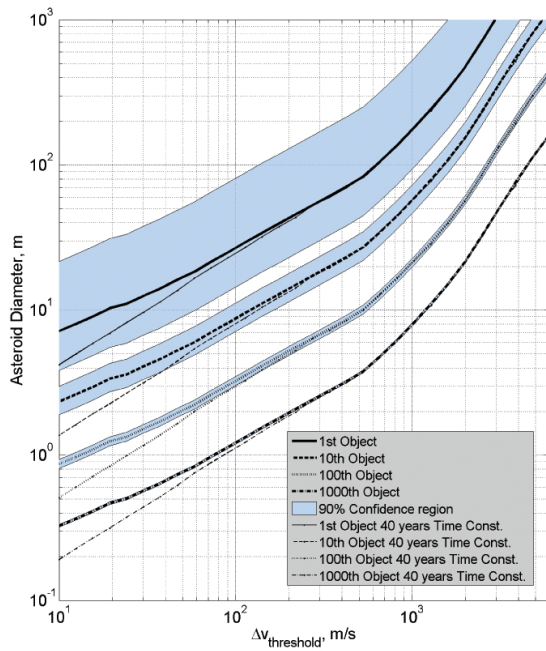


FIGURE 14. Expected size of the accessible asteroid.

photons along the Sun-Earth line.

In contrast, the reflector methods that place objects at the L₁ point are much more mass efficient as the reflectors will constantly be in a position to shade the Earth. However, the downside to this method is that the reflectors must be manufactured either terrestrially and launched into position or manufactured in-situ from captured NEA material. Both of these methods are currently unfeasible due to current launch and space manufacturing capabilities.

Therefore, there is a need to investigate a potentially more near-term method of space-based geoengineering. This is achieved by investigating the macro-scale concept of placing a large cloud of unprocessed asteroid dust at the L₁ point using the micro-scale astrodynamics associated with high area-to-mass ratio particles discussed earlier. It is envisaged that such a dust cloud can be created by either using a solar collector to sublimate material from the surface of a captured NEA, or by mass driver equipped landers on a NEA surface. The sublimation process can be used to both capture the NEA and bound its position in the vicinity of the L₁ point. In order to model the dynamics of such dust clouds, solar radiation pressure, parameterised by the dust grain ‘lightness factor’, β , must be included in the equations of motion of the circular restricted three-body problem

(CR3BP). The value of β can be determined by the ratio of the solar radiation pressure force to the solar gravitational force and is defined as:

$$\beta = \frac{|\mathbf{F}_{\text{rad}}|}{|\mathbf{F}_g|} = 570 \frac{Q}{\rho R} \quad (4)$$

where Q is the coefficient of reflectance, ρ is the grain density in kg m⁻³ and R is the grain radius in μm. The factor Q varies from a value of 0 for a completely transparent material to 1 for a completely absorbing material and 2 for a completely reflecting material. The inclusion of solar radiation pressure results in the effective mass of the Sun being reduced in the mass parameter, μ , as shown in equation (5), thus affecting the dynamics of the CR3BP.

$$\mu = \frac{M_E}{(1 - \beta)M_S + M_E} \quad (5)$$

where M_E is the mass of the Earth and M_S is the mass of the Sun. The motion of the particles in the CR3BP can now be modelled for a cloud of dust placed in the region of the interior Lagrange point along the Sun-Earth line, a full description of which can be found in [3]. Due to the instability of the L₁ point, a cloud placed in its vicinity will disperse over time. Using a model of the dynamics of the problem a steady state solution can be found such that the average density of the cloud in the phase space of the problem can be determined for the lifetime of the cloud. Using this understanding of the dust dynamics, along with a solar radiation model, also described in [3], the reduction in solar insolation experienced on the Earth’s surface can be determined. This process has been completed for several scenarios which incorporate a varying initial cloud position and size and dust grain size. The initial position varies between the classical L₁ position and the new equilibrium position found when the effect of solar radiation pressure is taken into account, whilst the initial dust cloud radius varies from 500 km to 12,000 km. Four initial grain sizes have also been used, these being 32 μm, 10 μm, 3.2 μm and 0.01 μm, which correspond to β values of 0.005, 0.018, 0.061 and 0.106 respectively [36].

It has been determined that a 1.7% solar insolation reduction will offset the effects of a temperature increase of 2°C [14], equivalent to a doubling of the atmospheric concentration of CO₂. The mass requirement of dust for the cloud being released at the classical L₁ position can be seen in Figure 15 whilst the results for the cloud being released from the new, displaced, equilibrium point

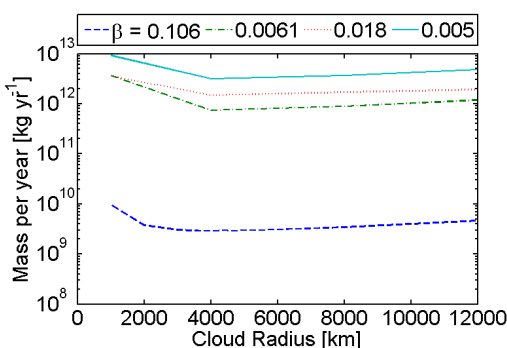


FIGURE 15. Mass requirement of dust for the steady state solution of clouds ejected at the L₁ point for varying initial cloud radii for the four grain sizes used.

can be seen in Figure 16. The minimum mass of dust injected into the cloud per year necessary to achieve the required insolation reduction is $8.87 \times 10^8 \text{ kg yr}^{-1}$, as can be seen in Figure 16. This result was achieved for a 3,000 km diameter cloud, released at the displaced equilibrium position for a grain size of 0.01 μm. This mass is considerably lower than previous dust based space-based geoengineering concepts and is also of the same order as the solid reflector methods, assuming a mission lifetime of 10 years, whilst reducing complexity considerably through the use of unprocessed dust rather than highly engineering reflectors or refractors. Further work is being carried out to determine the effect that the gravitational potential of the captured NEA has on the stability of the cloud created from the asteroid. The NEA can therefore help anchor the dust cloud.

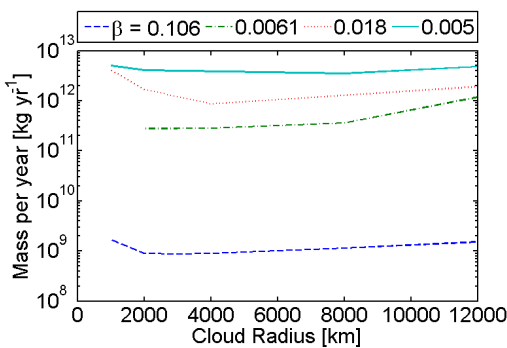


FIGURE 16. Mass requirement of dust for the steady state solution of clouds ejected at the new displaced equilibrium points of the four grain radii used for varying initial cloud sizes.

5 Conclusions

This paper has provided an overview of an on-going programme of work which aims to deliver radically new approaches to astrodynamics at extremes of length-scale to underpin new space-derived products and services. New developments in astrodynamics at three length-scales, micro, meso and macro, have been discussed with a range of applications for future space systems, from space science through to telecommunications and Earth observation, and longer-term concepts such as space-based geo-engineering. A unifying feature of this work is that astrodynamics at the smallest and largest of length-scales will lead to strongly perturbed orbits, for example with MEMS-scale ‘smart dust’ devices, or natural dust grains, and large gossamer spacecraft. At these extremes of length-scale, perturbations such as atmospheric drag, solar radiation pressure and electrodynamic forces can be of the same order of magnitude as the central two-body or three-body gravitational forces. The strongly perturbed nature of the dynamics of such systems gives rise to rich new families of orbits which can be exploited to deliver new space products and services. Finally, there are intriguing connections between the micro and macro length-scales through the exploitation of an understanding of dust dynamics for both swarms of ‘smart dust’ and large-scale space-based geo-engineering.

6 Acknowledgments

This work was supported by an Advanced Investigator Grant from the European Research Council through VISIONSPACE (ERC project 227571).

References

- [1] R. Angel. Feasibility of cooling the Earth with a cloud of small spacecraft near the inner lagrange point (L_1). *Proceedings of the National Academy of Sciences*, 103(46):17184–17189, 2006.
- [2] S. Baig and C. R. McInnes. Light-levitated geostationary cylindrical orbits are feasible. *Journal of Guidance, Control, and Dynamics*, 33(3):782–793, 2010.
- [3] R. Bewick, J. P. Sanchez, and C. R. McInnes. An L_1 positioned dust cloud as an effective method of space-based geo-engineering. In *61st International Astronautical Congress (IAC 2010)*, number IAC-10.D1.1.7, 27 September – 1 October 2010.
- [4] W. F. Bottke, A. Morbidelli, R. Jedicke, J. M. Petit, H. F. Levison, P. Michel, and T. S. Metcalfe. Debiased orbital and absolute magnitude distribution of the Near-Earth Objects. *Icarus*, 156(2):399–433, 2002.
- [5] M. Ceriotti and C. R. McInnes. An Earth pole-sitter using hybrid propulsion. In *AIAA/AAS Astrodynamics Specialist Conference*, number AIAA 2010-7830. AIAA, 2-5 August 2010.
- [6] M. Ceriotti and C. R. McInnes. Hybrid solar sail and SEP propulsion for novel Earth observation missions. In *61st International Astronautical Congress (IAC 2010)*, number IAC-10.C4.6.8, 27 September – 1 October 2010.
- [7] M. Ceriotti and C. R. McInnes. A near term pole-sitter using hybrid solar sail propulsion. In R. Kezerashvili, editor, *2nd International Symposium on Solar Sailing (ISSS 2010)*, pages 163–170. New York City College of Technology, 20-22 July 2010.
- [8] C. Colombo, C. M. Lücking, and C. R. McInnes. Orbit evolution, maintenance and disposal of SpaceChip swarms. In *6th International Workshop on Satellite Constellation and Formation Flying (IWSCFF 2010)*, number IWSCFF 2010 2-2, 1-3 November 2010.
- [9] C. Colombo and C. R. McInnes. Orbit design for future SpaceChip swarm missions. In *61st International Astronautical Congress (IAC 2010)*, number IAC-10.C1.8.2, 27 September – 1 October 2010.
- [10] C. Colombo and C. R. McInnes. Orbital dynamics of Earth-orbiting ‘smart dust’ spacecraft under the effects of solar radiation pressure and aerodynamic drag. In *AIAA/AAS Astrodynamics Specialist Conference*, number AIAA 2010-7656. AIAA, 2-5 August 2010.
- [11] C. Colombo and C. R. McInnes. Orbital dynamics of ‘smart dust’ devices with solar radiation pressure and drag. *Accepted for publication Journal of Guidance, Control, and Dynamics*, 2011.
- [12] J. M. Driver. Analysis of an arctic polesitter. *Journal of Spacecraft and Rockets*, 17(3):263–269, 1980.
- [13] G. Gómez, W. S. Koon, M. W. Lo, J. E. Marsden, J. Masdemont, and S. D. Ross. Connecting orbits and invariant manifolds in the spatial restricted three-body problem. *Nonlinearity*, 17(5):1571–1606, 2004.
- [14] B. Govindasamy, K. Caldeira, and P. B. Duffy. Geoengineering Earth’s radiation balance to mitigate climate change from a quadrupling of CO_2 . *Global and Planetary Change*, 37(1-2):157–168, 2003.
- [15] J. Heiligers. Displaced geostationary orbits using hybrid low-thrust propulsion. In *61st International Astronautical Congress (IAC 2010)*, number IAC-10-E2.1.2, 2010.
- [16] IPCC. Contribution of working groups i, ii and iii to the fourth assessment report of the intergovernmental panel on climate change. *Core Writing Team, Pachauri, R.K. and Reisinger, A. (Eds.), IPCC, Geneva, Switzerland. pp 104*, 2007.
- [17] R. Jahn, A. Rossi, T. Flohrer, and D. Navarro-Reyes. Reorbiting of satellites in high altitudes. In *5th European Conference on Space Debris*, 2009.
- [18] D. King-Hele. *Theory of satellite orbits in an atmosphere*. Butterworths, London, 1964.
- [19] W. S. Koon, M. W. Lo, J. E. Marsden, and S. D. Ross. Heteroclinic connections between periodic orbits and resonance transitions in celestial mechanics. *Chaos*, 10(2):427–469, 2000.
- [20] M. A. Lazzara. The polar meteorologist’s dream machine: artificial Lagrange orbit satellite applications via arctic and antarctic composite satellite

- imagery. In R. Kezerashvili, editor, *2nd International Symposium on Solar Sailing (ISSS 2010)*, pages 49–55. New York City College of Technology, 20–22 July 2010.
- [21] M. Leipold and M. Götz. Hybrid photonic/electric propulsion. Technical Report SOL4-TR-KTH-0001, ESA contract No. 15334/01/NL/PA, Kayser-Threde GmbH, Jan. 2002. ESA contract No. 15334/01/NL/PA.
- [22] J. Lewis. *Mining the sky: untold riches from asteroids, comets and planets*. Helix Books/Perseus Books Reading, 1996.
- [23] C. M. Lücking, C. Colombo, and C. R. McInnes. Orbit control of high area-to-mass ratio spacecraft using electrochromic coating. In *61st International Astronautical Congress (IAC 2010)*, number IAC-10.C1.2.7, 27 September – 1 October 2010.
- [24] M. Macdonald and C. R. McInnes. Solar sail mission applications and future advancement. In R. Kezerashvili, editor, *2nd International Symposium on Solar Sailing (ISSS 2010)*, 2010.
- [25] C. R. McInnes. The existence and stability of families of displaced two-body orbits. *Celestial Mechanics and Dynamical Astronomy*, 67(2):167–180, 1997.
- [26] C. R. McInnes. Dynamics, stability, and control of displaced non-Keplerian orbits. *Journal of Guidance, Control, and Dynamics*, 21(5):799–805, 1998.
- [27] C. R. McInnes. *Solar Sailing: Technology, Dynamics and Mission Applications*. Springer-Praxis Books in Astronautical Engineering, Springer-Verlag, 1999.
- [28] C. R. McInnes. Space-based geoengineering: challenges and requirements. *Proceedings of the Institution of Mechanical Engineers, Part C: Journal of Mechanical Engineering Science*, 224(3):571–580, 2010.
- [29] O. Mori, H. Sawada, R. Funase, T. Endo, M. Morimoto, T. Yamamoto, Y. Tsuda, Y. Kawakatsu, and J. Kawaguchi. Development of first solar power sail demonstrator - IKAROS. In *21st International Symposium on Space Flight Dynamics (ISSFD 2009)*. CNES, 2009.
- [30] J. Pearson, J. Oldson, and E. Levin. Earth rings for planetary environment control. *Acta Astronautica*, 58(1):44–57, 2006.
- [31] A. E. Roy. *Foundations of Astrodynamics*. Macmillan, London, 1965.
- [32] J. P. Sanchez, C. Colombo, M. Vasile, and G. Radice. Multi-criteria comparison among several mitigation strategies for dangerous Near Earth Objects. *Journal of Guidance, Control and Dynamics*, 32(1):121–142, 2009.
- [33] J. P. Sanchez and C. R. McInnes. Assessment on the Feasibility of Future Sheperding of Asteroid Resources. In *61st International Astronautical Congress (IAC 2010)*, number IAC-10.D3.2.7. International Astronautical Federation, 27 September – 1 October 2010.
- [34] J. Shepherd, K. Caldeira, P. Cox, and J. Haigh. Geoengineering the climate. *Report of Royal Society working group of geo-engineering*, 2009.
- [35] C. Struck. The feasibility of shading the greenhouse with dust clouds at the stable lunar Lagrange points. *Journal of the British Interplanetary Society*, 60(3):82–89, 2007.
- [36] M. Wilck and I. Mann. Radiation pressure forces on "typical" interplanetary dust grains. *Planetary and Space Science*, 44(5):493–499, 1996.

